

# NOTE TO USERS

This reproduction is the best copy available.

**UMI**<sup>®</sup>



**COSEISMIC DEFORMATION OF THE 2001 EL  
SALVADOR AND 2002 DENALI FAULT EARTHQUAKES  
FROM GPS GEODETIC MEASUREMENTS**

A  
THESIS

Presented to the Faculty  
of the University of Alaska Fairbanks  
in Partial Fulfillment of the Requirements  
for the Degree of

**DOCTOR OF PHILOSOPHY**

By

Sigrún Hreinsdóttir, B.S., M.S.

Fairbanks, Alaska

May 2005

UMI Number: 3167007

Copyright 2005 by  
Hreinsdottir, Sigrun

All rights reserved.

### INFORMATION TO USERS

The quality of this reproduction is dependent upon the quality of the copy submitted. Broken or indistinct print, colored or poor quality illustrations and photographs, print bleed-through, substandard margins, and improper alignment can adversely affect reproduction.

In the unlikely event that the author did not send a complete manuscript and there are missing pages, these will be noted. Also, if unauthorized copyright material had to be removed, a note will indicate the deletion.

**UMI**<sup>®</sup>

---

UMI Microform 3167007

Copyright 2005 by ProQuest Information and Learning Company.

All rights reserved. This microform edition is protected against unauthorized copying under Title 17, United States Code.

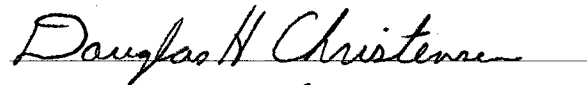
ProQuest Information and Learning Company  
300 North Zeeb Road  
P.O. Box 1346  
Ann Arbor, MI 48106-1346

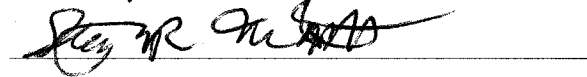
COSEISMIC DEFORMATION OF THE 2001 EL SALVADOR AND  
2002 DENALI FAULT EARTHQUAKES FROM GPS GEODETIC  
MEASUREMENTS

By

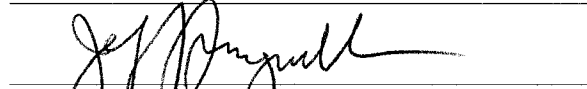
Sigrún Hreinsdóttir

RECOMMENDED:

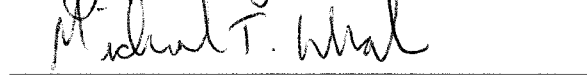






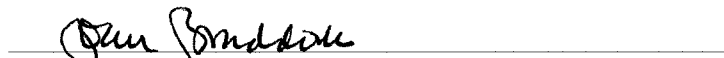


Advisory Committee Chair

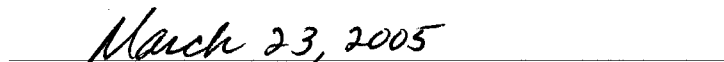


Chair, Department of Geology and Geophysics

APPROVED:

  
Dean, College of Natural Science and Mathematics

  
Dean of the Graduate School

  
Date

### Abstract

GPS geodetic measurements are used to study two major earthquakes, the 2001  $M_W$  7.7 El Salvador and 2002  $M_W$  7.9 Denali Fault earthquakes.

The 2001  $M_W$  7.7 earthquake was a normal fault event in the subducting Cocos plate offshore El Salvador. Coseismic displacements of up to 15 mm were measured at permanent GPS stations in Central America. The GPS data were used to constrain the location of and slip on the normal fault. One month later a  $M_W$  6.6 strike-slip earthquake occurred in the overriding Caribbean plate. Coulomb stress changes estimated from the  $M_W$  7.7 earthquake suggest that it triggered the  $M_W$  6.6 earthquake. Coseismic displacement from the  $M_W$  6.6 earthquake, about 40 mm at a GPS station in El Salvador, indicates that the earthquake triggered additional slip on a fault close to the GPS station. The  $M_W$  6.6 earthquake further changed the stress field in the overriding Caribbean plate, with triggered seismic activity occurring west and possibly also to the east of the rupture in the days to months following the earthquake.

The  $M_W$  7.9 Denali Fault earthquake ruptured three faults in the interior of Alaska. It initiated with a thrust motion on the Susitna Glacier fault but then ruptured the Denali and Totschunda faults with predominantly right-lateral strike-slip motion unilaterally from west to east. GPS data measured in the two weeks following the earthquake suggest a complex coseismic rupture along the faults with two main regions of moment release along the Denali fault. A large amount of additional data were collected in the year following the earthquake which greatly improved the resolution on the fault, revealing more details of the slip distribution. We estimate a total moment release of  $6.81 \times 10^{20}$  Nm in the earthquake with a  $M_W$  7.2 thrust subevent on Susitna Glacier fault. The slip on the Denali fault is highly variable, with 4 main pulses of moment release. The largest moment pulse corresponds to a  $M_W$  7.5 subevent, about 40 km west of the Denali-Totschunda fault junction. We estimate relatively low and shallow slip on the Totschunda fault.

## Table of Contents

Signature Page . . . . .	i
Title Page . . . . .	ii
Abstract . . . . .	iii
Table of Contents . . . . .	iv
List of Figures . . . . .	vi
List of Tables . . . . .	viii
List of Appendices . . . . .	ix
Acknowledgments . . . . .	x
<b>1 Introduction</b>	<b>1</b>
1.1 Tectonic Geodesy . . . . .	1
1.2 Overview of Thesis Contents . . . . .	2
<b>2 The 2001 January 13th <math>M_W</math> 7.7 and February 13th <math>M_W</math> 6.6 El Salvador Earthquakes: Deformation and Stress Triggering</b>	<b>4</b>
2.1 Abstract . . . . .	4
2.2 Introduction . . . . .	4
2.3 GPS Data and Analysis . . . . .	6
2.4 Deformation and Seismic Data . . . . .	10
2.4.1 January 13 2001, $M_W$ 7.7 Earthquake . . . . .	10
2.4.2 February 13 2001, $M_W$ 6.6 Earthquake . . . . .	14
2.5 Seismicity and Stress Changes Following the January 13 Earthquake . . . . .	18
2.6 Conclusions . . . . .	23
2.7 Acknowledgments . . . . .	25
<b>3 Coseismic Slip Distribution of the 2002 <math>M_W</math> 7.9 Denali Fault Earthquake, Alaska, Determined from GPS Measurements</b>	<b>28</b>
3.1 Abstract . . . . .	28
3.2 Introduction . . . . .	28
3.3 GPS Data and Analysis . . . . .	29
3.4 Inversion for Fault Slip Model . . . . .	31
3.5 Discussion and Conclusions . . . . .	35
3.6 Acknowledgments . . . . .	37

<b>4</b>	<b>Coseismic Deformation of the 2002 Denali Fault Earthquake: Insights from GPS Measurements</b>	<b>40</b>
4.1	Abstract . . . . .	40
4.2	Introduction . . . . .	40
4.3	GPS Data and Analysis . . . . .	44
4.3.1	Pre-Earthquake Survey Data . . . . .	46
4.3.2	Post Nenana Mt. Earthquake Data . . . . .	47
4.3.3	Post Denali Fault Earthquake Data . . . . .	48
4.3.4	GPS Data Analysis . . . . .	48
4.3.5	Black Rapids Glacier Geodetic Network . . . . .	49
4.3.6	Estimating Coseismic Displacements . . . . .	50
4.3.7	Nenana Mt. Earthquake . . . . .	53
4.4	Coseismic Displacements . . . . .	56
4.4.1	Denali Hwy Profile . . . . .	59
4.4.2	Black Rapids Glacier . . . . .	61
4.4.3	Richardson Hwy/Trans-Alaska Pipeline Profile . . . . .	63
4.5	Inversion on 3D Fault Model in Elastic Half Space . . . . .	67
4.5.1	Data . . . . .	67
4.5.2	Fault Model . . . . .	68
4.5.3	Inversion Method . . . . .	69
4.5.4	Coseismic Slip Distribution . . . . .	72
4.5.5	Resolution and Uncertainty . . . . .	79
4.6	Discussion . . . . .	81
4.7	Conclusions . . . . .	87
4.8	Acknowledgments . . . . .	88
<b>5</b>	<b>Conclusions</b>	<b>94</b>
5.1	General . . . . .	94
5.2	The 2001 El Salvador Earthquakes . . . . .	94
5.3	The 2002 Denali Fault Earthquake . . . . .	95
5.4	Future of Earthquake Research with GPS . . . . .	96



## List of Figures

2.1	Plate boundaries in Central America . . . . .	5
2.2	The $M_W$ 7.7 (01/13) earthquake's epicenter . . . . .	7
2.3	Earthquake activity in El Salvador from January 13 to May 15, 2001 . . . . .	8
2.4	GPS time series for the station SSIA in El Salvador relative to MANA in Nicaragua . . . . .	11
2.5	Coseismic displacements (black vectors) from the $M_W$ 7.7 January 13 El Salvador earthquake . . . . .	12
2.6	$\Delta\chi^2$ for estimated model parameters . . . . .	15
2.7	Coseismic displacement at the site SSIA in San Salvador from the $M_W$ 6.6 February 13 El Salvador earthquake . . . . .	16
2.8	Coulomb failure stress changes estimated from the $M_W$ 7.7 earthquake for right-lateral strike-slip faults at 10 km depth . . . . .	20
2.9	Coulomb failure stress changes estimated from the $M_W$ 7.7 earthquake for left-lateral strike-slip faults at 10 km depth . . . . .	21
2.10	Effects of the coefficient of friction . . . . .	22
2.11	Coulomb failure stress change estimated from the $M_W$ 6.6 earthquake for left-lateral strike-slip faults . . . . .	24
3.1	GPS sites used in this study . . . . .	29
3.2	Coseismic displacements (black) from the $M_W$ 7.9 earthquake . . . . .	30
3.3	Vertical coseismic displacements (blue) from the $M_W$ 7.9 earthquake . . . . .	32
3.4	Trade-off curve between roughness and misfit (circles and solid line) and the CVSS as function of smoothing factor (squares with dashed line) . . . . .	34
3.5	Coseismic slip distribution for the $M_W$ 7.9 Denali fault earthquake . . . . .	35
3.6	Estimated right lateral surface offset of the preferred model (line) compared to geological surface measurements . . . . .	36
4.1	Tectonic setting of the Denali Fault earthquake . . . . .	42
4.2	Horizontal coseismic displacements from the $M_W$ 7.9 Denali Fault earthquake . . . . .	45
4.3	The $M_W$ 6.7 Nenana Mt. earthquake . . . . .	55

4.4	Near-field coseismic displacements from the Denali Fault earthquake . . . .	57
4.5	Vertical coseismic displacements from the $M_W$ 7.9 Denali Fault earthquake	58
4.6	GPS data along Denali Hwy, south of and parallel to the Denali fault . . .	60
4.7	Black Rapids Glacier network . . . . .	61
4.8	Geological surface offset measurements and estimated average slip . . . . .	62
4.9	Coseismic displacements along Richardson Hwy profile . . . . .	65
4.10	Richardson Hwy profile (azimuth N120°E) . . . . .	66
4.11	Weighted residual sum of squares (solid line) and weighted cross-validation sum of squares (dashed line) . . . . .	71
4.12	Range of reasonable coseismic slip models from the roughest ( $\beta = 2.5 \text{ km}^2/\text{m}$ ) to the smoothest ( $\beta = 7 \text{ km}^2/\text{m}$ ) . . . . .	73
4.13	Coseismic slip model of the Denali Fault earthquake ( $\beta = 4 \text{ km}^2/\text{m}$ ) . . . .	74
4.14	Model residuals exceeding 95% confidence region of measured displacements	75
4.15	Weighted Residual Sum of Squares as a function of maximum depth of slip allowed in the model . . . . .	76
4.16	Comparison between modeled surface offset (lines) and geological surface offset data . . . . .	77
4.17	Weighted Residual Sum of Squares as a function of dip-slip bounds in the BVLS inversion . . . . .	78
4.18	Inversion result from a synthetic dataset calculated using a synthetic checker- board model of $12 \text{ km} \times 12 \text{ km}$ . . . . .	79
4.19	Inversion result from a synthetic dataset calculated using a simple synthetic model . . . . .	81
4.20	Estimated uncertainty of the coseismic slip distribution using a Monte Carlo simulation . . . . .	82
4.21	Moment release per 3 km section along the earthquake rupture . . . . .	83

### List of Tables

2.1 Coseismic displacements relative to MANA in Nicaragua . . . . .	10
2.2 Location and fault plane solutions for the $M_W$ 7.7 earthquake . . . . .	13
2.3 Location and fault plane solutions for the $M_W$ 6.6 earthquake. . . . .	13
A.1 Coseismic GPS data for the Denali Fault earthquake. . . . .	98
B.1 GPS stations and surveys . . . . .	101
B.2 Nenana Mt. earthquake displacements . . . . .	110
B.3 Corrections . . . . .	111
B.4 Denali Fault earthquake displacements . . . . .	117

**List of Appendices**

<b>A Table with Chapter 3</b>	<b>98</b>
<b>B Tables With Chapter 4</b>	<b>100</b>

## Acknowledgments

Many people have contributed to this thesis in one way or another. I would first of all like to thank my advisor, Jeffrey T. Freymueller, for all the support and guidance he has given me throughout this study. His office was always open and he made the time to discuss problems and solve them with me when I was stuck on a hurdle or two. He gave me a chance to work on some amazing projects and his expertise in the field has been invaluable. Many thanks! I would also like to thank my committee, both current committee members, Douglas Christensen, Steve McNutt and Natalia Ratchkovski, and previous committee members, Max Wyss and Evelyn Price. They have given me important guidance, in particular in the field of seismology. In addition I have benefited greatly from the guidance and help of Dr. Roland Bürgmann who generously offered his time and expertise during a crazy time period following the Denali Fault earthquake, at which time my thesis took a 90° turn.

I would like to thank the people that are partly responsible for which direction I have taken in life. My M.S. advisors Páll Einarsson and Freysteinn Sigmundsson introduced me to GPS geodesy and got me addicted to the field. They along with Thóra Árnadóttir have been very supportive through the years and had a big part in me making the decision to come to Alaska to pursue a Ph.D. degree.

I have done lots of fieldwork since I came to Alaska and have worked with some wonderful people. I'd like to thank every one of you for the help and company provided on various trips. I would also like to thank my advisor in addition to Roger Hansen and Max Wyss for support to go to conferences during my study. I also had the privilege to go on an amazingly cool field trip to Katmai with the Alaska Volcano Observatory, one I'll never forget.

I want to thank my wonderful and supportive family who were the only people from Iceland that didn't think I was crazy to go from Iceland to Alaska ("of all places") for more school. In Alaska I have got to know some wonderful people and if it weren't for my very best friends Chris and Sharon this degree would have been so much harder to work at. They and "the girls" have kept me sane during my stay here. In addition I'd like to thank the Eichelberger family who has on so many occasions opened their home to me.

Last but not least I'd like to thank students and staff at the Geophysical Institute. It has been like one big family these past few years. In particular I'd like to thank Chris Larsen and Hilary Fletcher who have been very supportive.

## Chapter 1

### Introduction

#### 1.1 Tectonic Geodesy

We live on a dynamic planet. The surface of the earth is divided into near rigid tectonic plates that move relative to each other at rates of up to a few tens of mm/yr. Along the boundaries of the plates active deformation takes place, marked by seismic activity. With GPS geodetic measurements we can estimate both the plates' velocities as well as active deformation in the plate boundary zones.

A few years before Alfred Wegener presented his theory of continental drift (1915), the groundwork for the development of modern plate tectonics, Henry Fielding Reid presented his theory of elastic rebound (1910), the loading cycle for earthquakes. Reid based his theory on geodetic observations from a triangulation network, measured in the 1860's, 1880's, and just after the 1906, San Francisco, California earthquake. He noticed that in the earthquake locations close to the fault moved relative to locations on the opposite side of the fault and that the displacements were largest at the fault and decreased with distance. Measurements from the 1860's and 1880's showed that a location off the coast of California had moved relative to locations inland prior to the earthquake, suggesting that the fault was being loaded by steady motion of distant points. He suggested that the combined deformation prior to and during the earthquake would result in one block moving past the other along the fault. This marked a milestone in the understanding of tectonic earthquakes. [Reid, 1910; Scholz, 2002]

In the years following Reid's theory new geodetic techniques have been developed to measure crustal motion and our understanding of earthquakes has improved. Geodetic measurements of interseismic, coseismic, and postseismic deformation around faults has revealed more complex behavior than can be explained with a simple elastic model. With the measurements from each new earthquake we learn new things and we still have a lot to learn. The hope of one day being able to forecast earthquakes pushes the science forward. In recent years space geodesy (e.g. Very Long Baseline Interferometry (VLBI), Satellite Laser Ranging (SLR), Lunar Laser Ranging (LLR), and Global Positioning System (GPS)) has allowed us to make high precision measurements between distant points, to constrain plates motions as well as deformation along plate boundaries. GPS measurements have the

advantage over other techniques of being able to detect and measure mm level deformation as well as several meters of deformation over small regions (m) and globally (several hundred km or more), relatively cheaply and easily at any given time.

In this thesis I utilize the capabilities of GPS geodesy to study two major earthquakes that occurred in 2001 and 2002. I will show that with only a handful of permanent GPS stations, important constraints can be provided for earthquake slip models, and how a large number of GPS sites can reveal the detailed slip distribution of earthquakes. These studies give us further insight into earthquake mechanisms, bringing us one little step forward in the understanding of earthquakes.

## 1.2 Overview of Thesis Contents

This thesis consists of three main chapters (2, 3 and 4), each has been prepared individually for publication in scientific journals. Chapter 3 was published in 2003 (Geophysical Research Letters) and Chapter 4 is currently under review (Journal of Geophysical Research, Solid Earth). Co-authors are listed at the beginning of each chapter.

Chapter 2 discusses GPS measurements of two large earthquakes ( $M_W$  7.7 and  $M_W$  6.6) in El Salvador, occurring one month apart in 2001. Small but significant displacements were observed at permanent GPS stations in Central America following the earthquakes. In the chapter I show that with only a handful of permanent GPS stations I can constrain important aspects of earthquakes, such as location and slip. A simple earthquake model is constructed for the  $M_W$  7.7 earthquake that fits the GPS data. I use the model to show how the  $M_W$  7.7 earthquake could have triggered the  $M_W$  6.6 earthquake. I show that neither a simple left-lateral nor a right-lateral strike-slip fault as indicated by the fault plane solution from Harvard CMT for the  $M_W$  6.6 earthquake can alone explaining observed coseismic offset at a GPS site in El Salvador. This could suggest a triggered slip on a fault near the GPS station. I suggest that the earthquake and activity following the  $M_W$  6.6 earthquake indicate bookshelf style deformation in the region.

Chapter 3 discusses GPS measurements following the Denali Fault earthquake, a major ( $M_W$  7.9) earthquake that occurred in the interior of Alaska in 2002. I use data from permanent GPS stations and campaign GPS data collected in the 10 days following the earthquake to estimate the slip distribution of the earthquake. The data reveal a complex

nature of the earthquake slip.

In Chapter 4 I have expanded the study of the 2002 Denali Fault earthquake. Many sites were inaccessible in the months following the earthquake due to winter conditions. They were measured in the spring of 2003. In addition I benefit from GPS data from large number of survey markers along the highways in Alaska, measured prior to the earthquake by surveyors. These survey markers were re-measured in the summer of 2003. This dataset greatly improves our ability to resolve and model slip along the fault rupture. The data are affected by postseismic deformation from the earthquake, interseismic deformation, as well as coseismic deformation from the  $M_W$  6.7 Nenana Mt. earthquake, occurring 10 days prior to the Denali Fault earthquake. I estimate and correct the data for these signals and construct a detailed slip model for the Denali Fault earthquake. Statistical tests were run to estimate the optimal slip-model, providing the optimal fit to data versus model roughness. I also tested the models resolution and estimated the uncertainty of the slip using synthetic data sets and Monte Carlo simulation. I compare the results to slip distribution estimated from other studies.

## References

- Reid, H.F. (1910), The Mechanics of the Earthquake, The California Earthquake of April 18, 1906, Report of the State Investigation Commission, 2, Carnegie Institution of Washington, Washington, D.C.
- Scholz, C. H. (2002), The Mechanics of Earthquakes and Faulting, 2nd edition, Cambridge University Press, United Kingdom, Cambridge.



## Chapter 2

### The 2001 January 13th $M_W$ 7.7 and February 13th $M_W$ 6.6 El Salvador

#### Earthquakes:

#### Deformation and Stress Triggering<sup>1</sup>

##### 2.1 Abstract

On January 13 2001, an  $M_W$  7.7 normal fault earthquake occurred offshore El Salvador. The earthquake occurred in the subducting Cocos plate and was followed by high seismic activity in the region with several earthquakes exceeding magnitude 5. On February 13, an  $M_W$  6.6 strike-slip earthquake occurred in the overriding Caribbean plate, about 75 km NNW from the epicenter of the large January earthquake. Deformation due to both earthquakes was observed at continuous GPS stations in Central America. In the  $M_W$  7.7 earthquake small but significant displacements (10-15 mm) were measured at three GPS stations up to 200 km from the earthquake's epicenter. In the  $M_W$  6.6 earthquake  $39 \pm 3$  mm of coseismic displacement was measured at a GPS station in San Salvador, El Salvador, 30 km west of the epicenter. A post earthquake signal is detectable at the GPS station which could be related to observed seismic activity at faults in the vicinity of the GPS station. Coulomb failure stress changes estimated from the 2001 January 13  $M_W$  7.7 earthquake indicate that the  $M_W$  6.6 strike-slip earthquake was triggered by the earthquake.

##### 2.2 Introduction

Central America is seismically very active, with the transcurrent plate boundary between the North American and Caribbean plate trending east-west through central Guatemala, and the Cocos plate subducting beneath the Caribbean plate along the Mid-America trench off the Pacific coast (Figure 2.1) [Dewey and Suárez, 1991; White, 1991]. Offshore El Salvador the Cocos and the Caribbean plates are converging at the rate of  $74 \pm 3$  mm/yr [DeMets *et al.*, 1994]. This rapid convergence results in frequent large earthquakes at the plate interface [Ambraseys and Adams, 2001]. Moderate size earthquakes also occur frequently in the overriding Caribbean plate along the volcanic front [Ambraseys and Adams, 2001; White, 1991; White and Harlow, 1993]. Most occur in a tectonic depression that lies parallel to and coincides with the active volcanic belt [Burkart and Self, 1985]. The earthquakes are

---

<sup>1</sup>Manuscript in preparation with authors S. Hreinsdóttir and J. T. Freymueller.

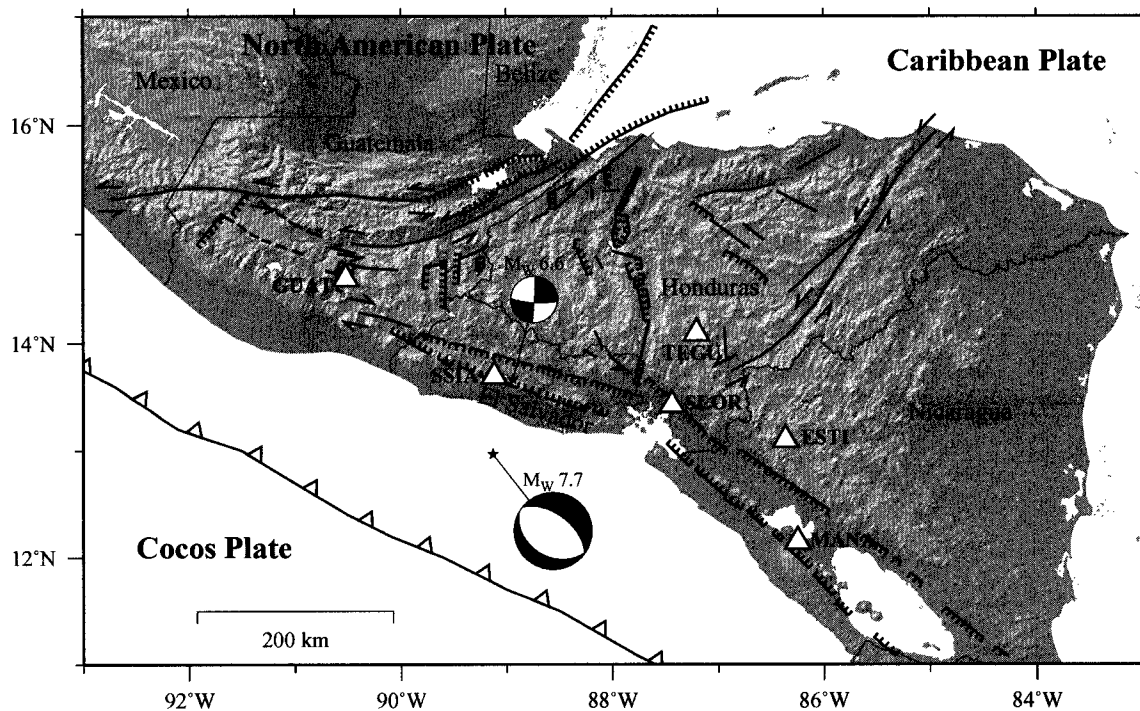


Figure 2.1. Plate boundaries in Central America and the location and focal mechanisms (Harvard-CMT) of the January 13 ( $M_W$  7.7) and February 13 ( $M_W$  6.6) El Salvador earthquakes. White triangles show location of the CORS GPS stations in Central America. Faults from *Burkart and Self* [1985].

in general of tectonic origin and are probably a result of the oblique component of the convergence between the Cocos and Caribbean plates [*White*, 1991]. North of El Salvador transcurrent displacement between the North American plate and the Caribbean plate, about 11 mm/yr, is taken up on several major strike-slip faults [*DeMets et al.*, 1994; *Burkart and Self*, 1985].

On the 13 of January 2001 an  $M_W$  7.7 earthquake occurred offshore El Salvador (Figures 2.1 and 2.2). It was a normal fault event occurring within the subducting Cocos plate [*Harvard CMT*, 2001; *NEIC*, 2001]. The earthquake caused major destruction and triggered large landslides across most of the southern half of El Salvador [*Bommer et al.*, 2002; *EERI*, 2001]. The earthquake was followed by high seismic activity over a broad area, with several aftershocks exceeding  $m_b$  4.5 (Figure 2.3a) [*ISC*, 2001]. A month later, on February 13, an  $M_W$  6.6 strike-slip earthquake occurred in the overriding Caribbean plate,  $\sim 30$  km east

of San Salvador (Figure 2.2). The earthquake was shallow, triggering large landslides and causing major destruction in its epicentral region. The earthquake was followed by a swarm of aftershocks in a  $10 \text{ km} \times 30 \text{ km}$  zone striking about  $\text{N}105^\circ \text{ E}$  (Figure 2.3d). On February 17 an  $M_L$  5.1 earthquake occurred in the western outskirts of San Salvador, west of the main aftershock region from the  $M_W$  6.6 strike-slip earthquake (Figure 2.3e) [EERI, 2001; Bommer *et al.*, 2002]. The aftershocks from the  $M_L$  5.1 earthquake indicate a SSW-NNE trending rupture plane. A few months later on May 8 2001, another  $M_L$  5.1 earthquake occurred in the region, this time located just east of the main aftershock region from the  $M_W$  6.6 strike-slip earthquake (Figure 2.3i). Aftershocks from this event cluster in a  $15 \text{ km} \times 20 \text{ km}$  region with several  $\geq M_L$  4 aftershocks indicating rupture on a SSW-NNE trending plane (Figure 2.3j).

Coseismic deformation due to the  $M_W$  6.6 and  $M_W$  7.7 earthquakes was observed at continuous GPS stations in Central America. The observed deformation of the January 13 earthquake in addition to seismic data allows us to model the earthquake source and calculate the Coulomb failure stress changes caused by the earthquake. Comparison of the areas of calculated increase in stress and observed seismic activity following the earthquakes show a correlation that indicates that the  $M_W$  7.7 earthquake triggered seismic activity in the overriding Caribbean plate.

### 2.3 GPS Data and Analysis

We use data from six continuous GPS stations located in Central America (Figure 2.1, Table 2.1). They are a part of the Continuously Operating Reference Stations project (CORS), coordinated by the National Geodetic Survey (NGS) [Spofford and Weston, 1998; Snay, 2000], and are operated by Central American Geodetic agencies in cooperation with the NGS.

The GPS data were analyzed using the GIPSY/OASIS II GOA4 software (release 1) developed at the Jet Propulsion Laboratory (JPL) using the JPL non-fiducial orbits. Data from each day were processed separately to obtain loosely constrained daily coordinate and covariance estimates for each station. Carrier phase ambiguity resolution was problematic on this data, therefore the solutions used in this paper do not include ambiguity resolution. Each GPS solution was then transformed into the International Terrestrial Reference

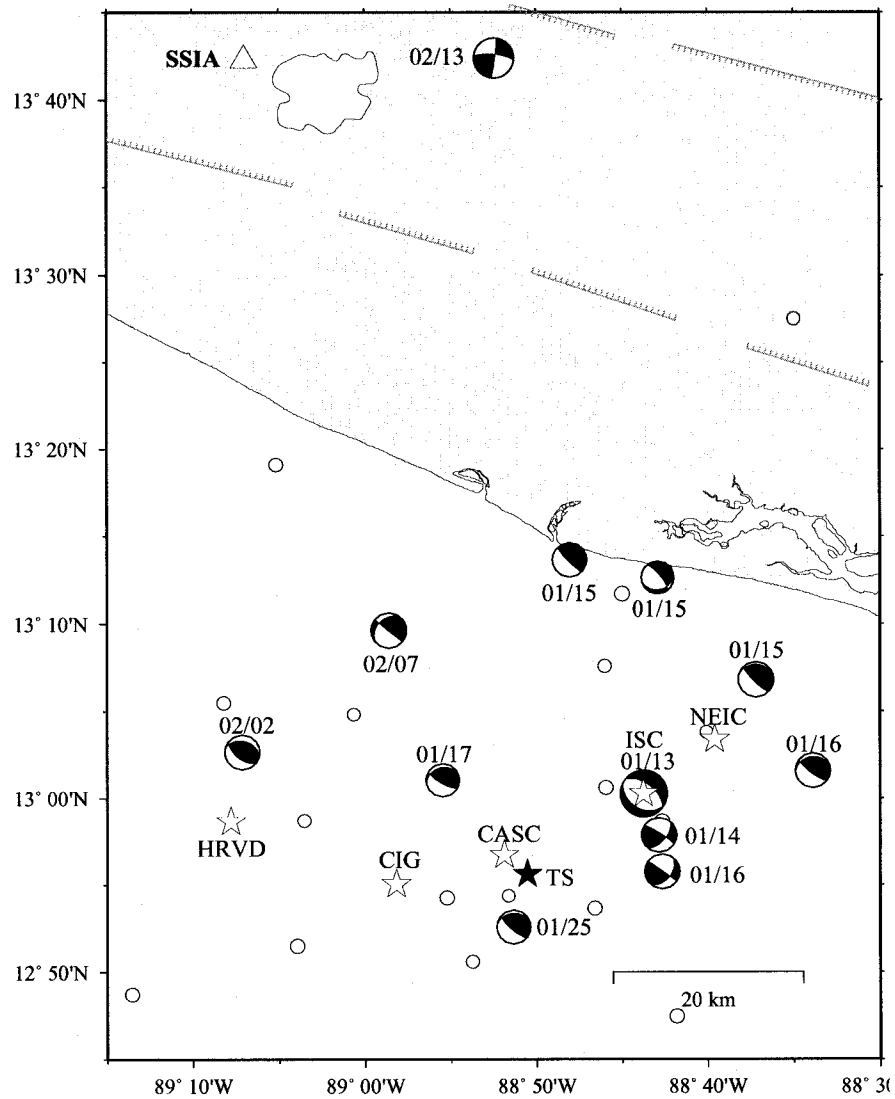


Figure 2.2. The  $M_W$  7.7 (01/13) earthquake's epicenter (from ISC) and focal mechanism (from Harvard CMT). The stars show the earthquake's locations estimated by Harvard CMT solution (HRVD), USGS Earthquake Information Center (NEIC), Centro de Investigaciones Geotécnicas (CIG), Central American Seismic Center (CASC), International Seismological Center (ISC), and this study (TS). In addition we show the epicenters (from ISC) for  $m_b \geq 4.5$  and focal mechanism (from Harvard CMT) for the largest earthquakes occurring in the region in the month following the  $M_W$  7.7 earthquake.

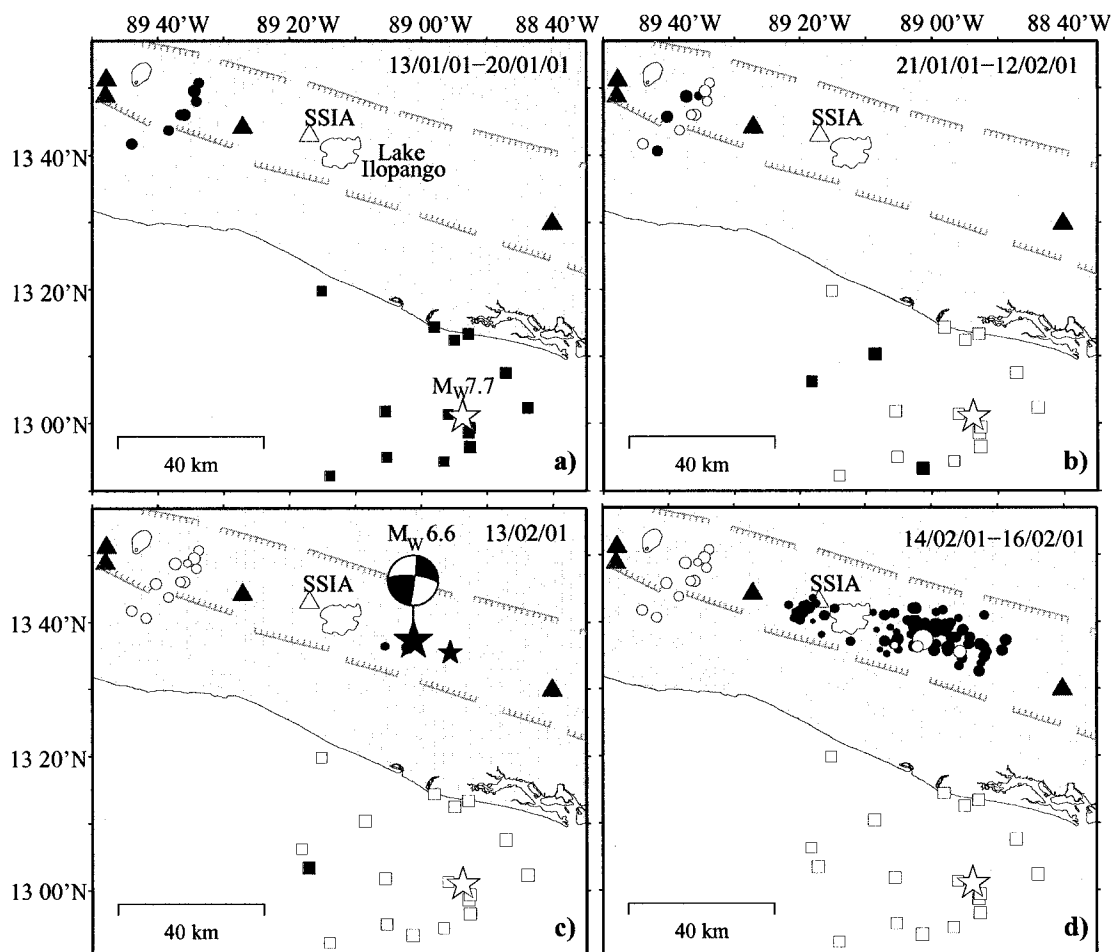


Figure 2.3. Earthquake activity in El Salvador from January 13 to May 15, 2001. The white star shows the epicenter of the  $M_W$  7.7 earthquake from the International Seismological Center (ISC). Squares show earthquakes of  $m_b \geq 4.5$  located offshore El Salvador (ISC). Circles and red stars show upper crustal earthquakes located by the Centro de Investigaciones Geotécnicas (CIG). Red stars ( $M_L \geq 4$ ) and blue events show earthquakes occurring within each time window. White events indicate earthquakes occurring in previous time windows. Black triangles show historically active volcanoes in the region. The CORS GPS station SSIA is shown with a yellow triangle. The focal mechanism for February 13  $M_W$  6.6 and May 8  $M_L$  5.1 from Harvard CMT are shown.

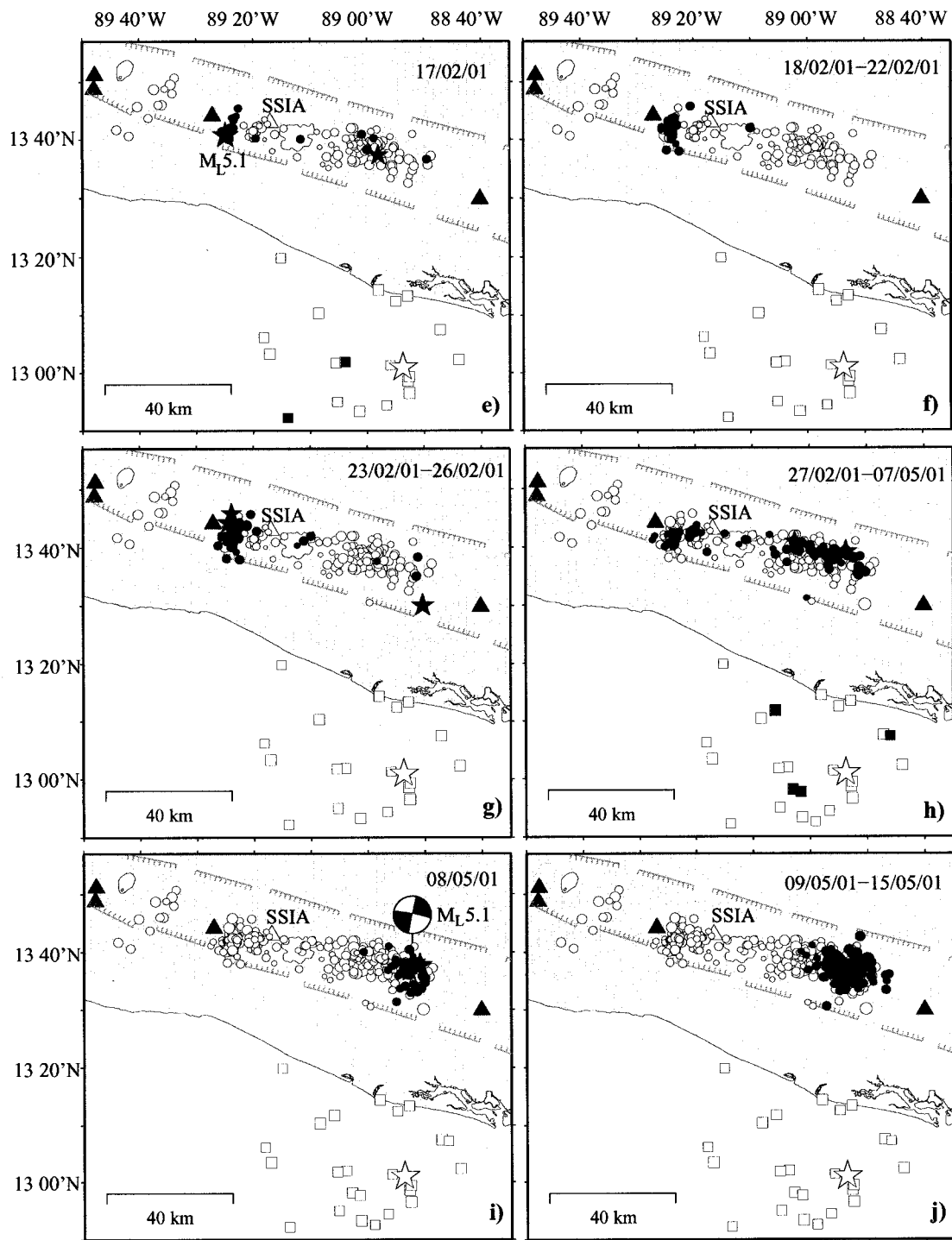


Figure 2.3. continued

Table 2.1. (12.1489°N, 86.2490°W). Uncertainties are  $1\sigma$ .

Station	Lat [°]	Lon [°]	$H$ [m]	$d_{\text{north}}$ [mm]	$d_{\text{east}}$ [mm]
January 13 $M_W$ 7.7					
GUAT	14.5904	-90.5198	1552.0	$0 \pm 2$	$-2 \pm 2$
SSIA	13.6971	-89.1166	626.6	$-11 \pm 2$	$10 \pm 2$
TEGU	14.0904	-87.2056	948.8	$8 \pm 2$	$7 \pm 2$
SLOR	13.4239	-87.4365	12.0	$6 \pm 2$	$10 \pm 2$
ESTI	13.0995	-86.3621	852.7	$3 \pm 2$	$1 \pm 2$
February 13 $M_W$ 6.6					
SSIA	13.6971	-89.1166	626.6	$-36 \pm 2$	$14 \pm 2$

Frame 2000 (ITRF00) [<http://lareg.ensg.igh.fr/ITRF/ITRF00>] using 20 to 22 reference sites surrounding Central America to define the 7 parameter Helmert transformation.

## 2.4 Deformation and Seismic Data

Following the January 13 2001  $M_W$  7.7 earthquake a significant offset of 10-15 mm was observed in time series data for the CORS GPS stations SSIA, TEGU, and SLOR in Central America, up to 200 km from the epicenter (Figure 2.4). The time series are rather noisy, in particular in the east component, so we estimate the site locations relative to the station MANA in Nicaragua that is furthest from the January and February activity. This minimizes common errors in the GPS solution, enhancing the small but detectable signal. On February 13 2001, an  $M_W$  6.6 earthquake occurred in the vicinity of the station SSIA resulting in a few cm coseismic offset at the site.

To estimated coseismic displacements at the GPS sites we merged together the last five pre-earthquake solutions and the first five post-earthquake solutions. We scaled the uncertainty by the scatter in the solutions and estimated displacements relative to MANA from the pre and post earthquake solutions.

### 2.4.1 January 13 2001, $M_W$ 7.7 Earthquake

We estimated coseismic displacements of the CORS GPS sites in Central America relative to MANA (Table 2.1, Figure 2.5). The closest site to the epicenter, SSIA, has a coseismic displacement towards the epicenter whereas sites east and north-east of the epicenter show displacements away from the epicenter.

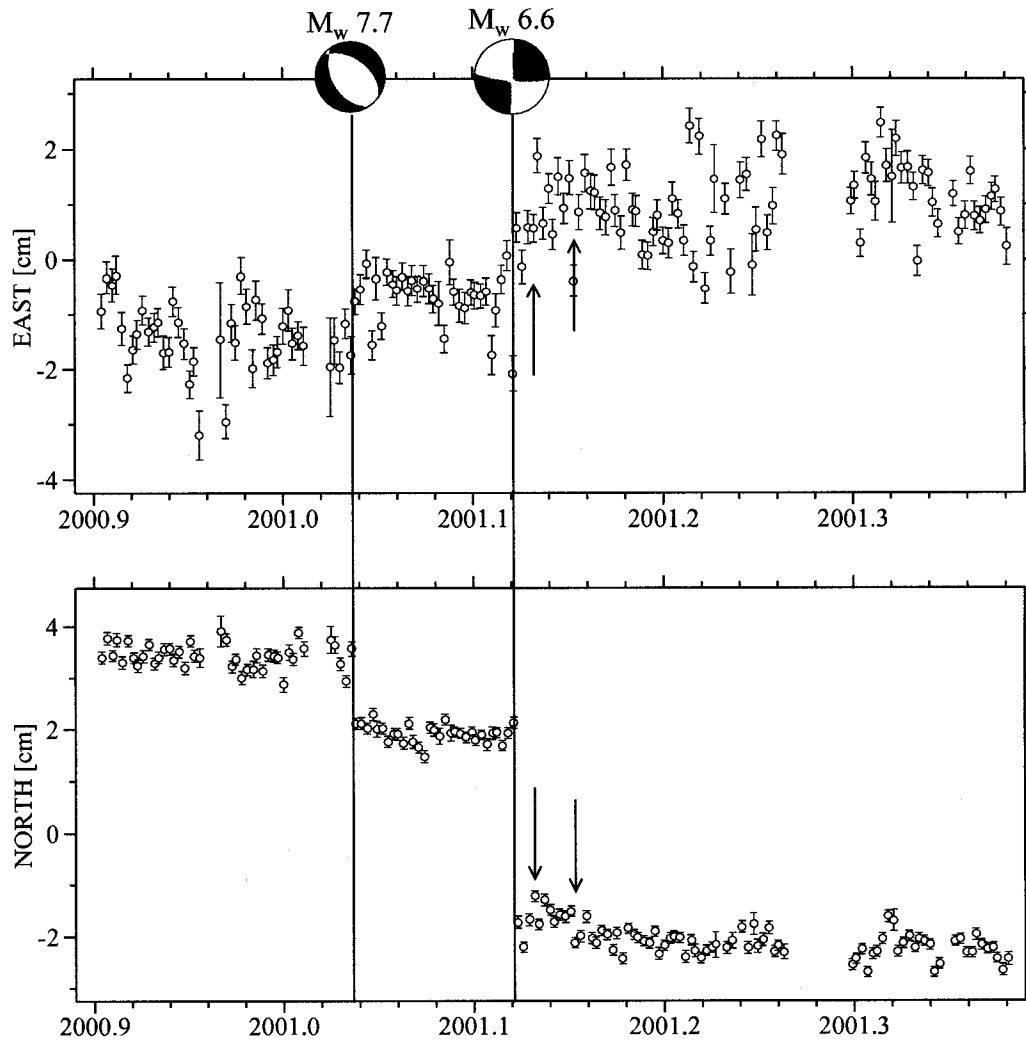


Figure 2.4. GPS time series for the station SSIA in El Salvador relative to MANA in Nicaragua (355.2 km distance). Two offsets are visible in the time series showing  $15 \pm 3$  mm displacement on January 13 at the time of the  $M_W$  7.7 earthquake and a larger offset,  $39 \pm 3$  mm, on February 13 at the time of the  $M_W$  6.6 earthquake. Following the February 13 earthquake we see a small post earthquake signal that could be related to local seismic activity on February 17 ( $M_L$  5.1) and February 25 ( $M_L$  4.6) (arrows).



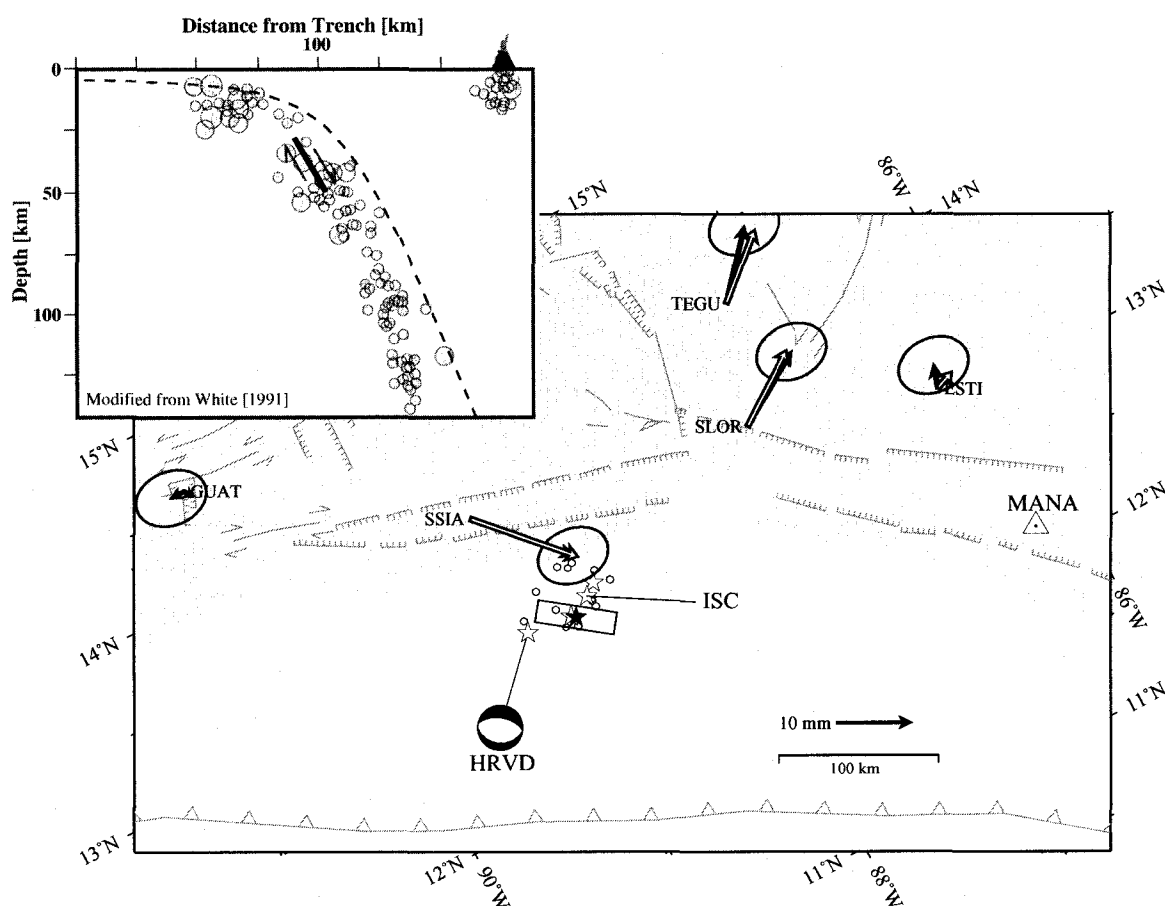


Figure 2.5. Coseismic displacements (black vectors) from the  $M_w$  7.7 January 13 El Salvador earthquake. The displacements are shown relative to the station MANA (with 95% confidence ellipses). White vectors show estimates from a best dislocation model relative to MANA, estimating slip and location of a fixed fault plane. The fault plane's dip and strike was fixed to the Harvard CMT solution's estimate (plane 2) but the dimensions of the fault plane were fixed to estimates from *Vallée et al.* [2003]. Aftershocks (circles) with  $m_b \geq 4.7$ , occurring in the month following the earthquake are shown for reference [ISC, 2001]. The inset shows the schematic settings of the earthquake rupture within the Cocos plate (modified from White [1991]).

Table 2.2. Location and fault plane solutions for the  $M_W$  7.7 earthquake

Source	Location			Plane 1			Plane 2*		
	Lat [°]	Lon [°]	D [km]	Strike	Dip	Rake	Strike	Dip	Rake
HRVD	2.9700	-89.1300	56.0	121°	35°	-95°	307°	56°	-86°
NEIC	13.0490	-88.6600	60.0f	121°	37°	-95°	307°	54°	-86°
Vallée et al.			48	119°	31°	-88°	297°	58°	-93°
CASC	12.9380	-88.8650	30.8						
ISC	12.9970	-88.7290	82.9						
GPS	12.920	-88.843	40						

\* Preferred value of *Vallée et al.* [2003]

Table 2.3. Location and fault plane solutions for the  $M_W$  6.6 earthquake.

Source	Location			Plane 1*			Plane 2		
	Lat [°]	Lon [°]	D [km]	Strike	Dip	Rake	Strike	Dip	Rake
HRVD	13.9800	-88.9700	15f	276°	74°	175°	7°	86°	16°
NEIC	13.6710	-88.9380	10f	96°	81°	-178°	6°	88°	-9°
CASC	13.6670	-88.8760	1.8						
ISC	13.6990	-88.8740	7.6						
CIG	13.6019	-88.8539	8.0						

\* Indicated by aftershock location [*Bommer et al.*, 2002].

Fault plane solutions give two possible fault planes for the earthquake, one dipping  $\sim 60^\circ$  to the northeast and the other dipping  $\sim 30^\circ$  to the southwest (Table 2.2). Both planes produce essentially identical geodetic displacements at the CORS GPS sites on land. Due to the offshore location of the earthquake and limitations of local and global seismic networks the aftershock locations are not accurate enough to determine which fault plane ruptured in the earthquake. *Vallée et al.* [2003] determined with an analysis of both teleseismic and local seismic data that the  $\sim 60^\circ$  dipping northeast plane was more likely to have ruptured.

Using a forward scheme we find a simple dislocation model that best fits the GPS data. Due to the small number of estimated coseismic displacements we cannot resolve the slip distribution in any detail. Instead we attempt to estimate the moment of the earthquake by estimating average slip on a fixed fault plane. We find that the fit to the GPS data is not very sensitive to variations in fault length or width. Models with smaller fault area required larger slip, indicating that the total seismic moment is well determined. *Vallée et al.* [2003] estimated a main moment release zone of approximately  $25 \text{ km} \times 50 \text{ km}$  with an

average slip of  $\sim 3.5$  m. We fix the width and length of our fault plane to the estimates of *Vallée et al.* [2003] and use a dip of  $56^\circ$  and strike of  $307^\circ$  in accord with the Harvard CMT solution (Table 2.2). The location of the earthquake has been determined by several agencies (Figure 2.2) with estimates ranging from about 20 to 50 km offshore El Salvador. We iteratively estimate the location and slip of a single dislocation in an elastic halfspace using the *Okada* [1985] solutions. We find an optimal slip of 3.5 m with the centroid of the dislocation located at  $12.920^\circ\text{N}$ ,  $88.843^\circ\text{W}$  and at 40 km depth (Figures 2.2 and 2.5). The estimated slip fits well with estimates from *Vallée et al.* [2003]. Our estimated location falls within the range of previous estimates (Figure 2.2 and 2.5). The north location is better constrained by the GPS data than the east component (Figure 2.6a) and the further north we move the fault, the shallower it must be to still fit the data reasonably well (Figure 2.6b). This reflects the tradeoff between the distance and depth of the dislocation relative to the GPS sites, the closer the dislocation is, the shallower it has to be in order to get same amount of slip at the site.

#### 2.4.2 February 13 2001, $M_W$ 6.6 Earthquake

The  $M_W$  6.6 earthquake occurred  $\sim 30$  km east of San Salvador, El Salvador, and caused a  $39 \pm 3$  mm coseismic displacement at the station SSIA (Figures 2.4 and 2.7). No other CORS GPS station in Central America showed significant displacement from the earthquake. The  $M_W$  6.6 earthquake was followed by a swarm of earthquakes occurring in a zone of  $10 \text{ km} \times 30 \text{ km}$  striking approximately  $\text{N}105^\circ\text{E}$ . The focal mechanism for the  $M_W$  6.6 earthquake (Table 2.3) gives either a left-lateral motion on a plane striking  $\text{N}7^\circ\text{E}$  or right-lateral motion on a plane striking  $\text{N}96^\circ\text{E}$ . Previous studies of the earthquake aftershock distribution have determined that the right lateral fault plane was more likely to have ruptured in the earthquake (e.g. [*Bommer et al.*, 2002]). The earthquake did not rupture the surface [*Bommer et al.*, 2002] and both ISC and CIG locate the hypocenter at about 8 km depth (Table 2.3).

Because we have only coseismic displacements at one GPS station there are limited constraints on the earthquake from GPS data. However the displacement and direction observed at SSIA is larger than expected for an earthquake of this magnitude. We used the empirical relationship for strike-slip earthquakes of *Wells and Coppersmith* [1994] and the epicenter and aftershock locations to constrain possible location, width, length, depth, and

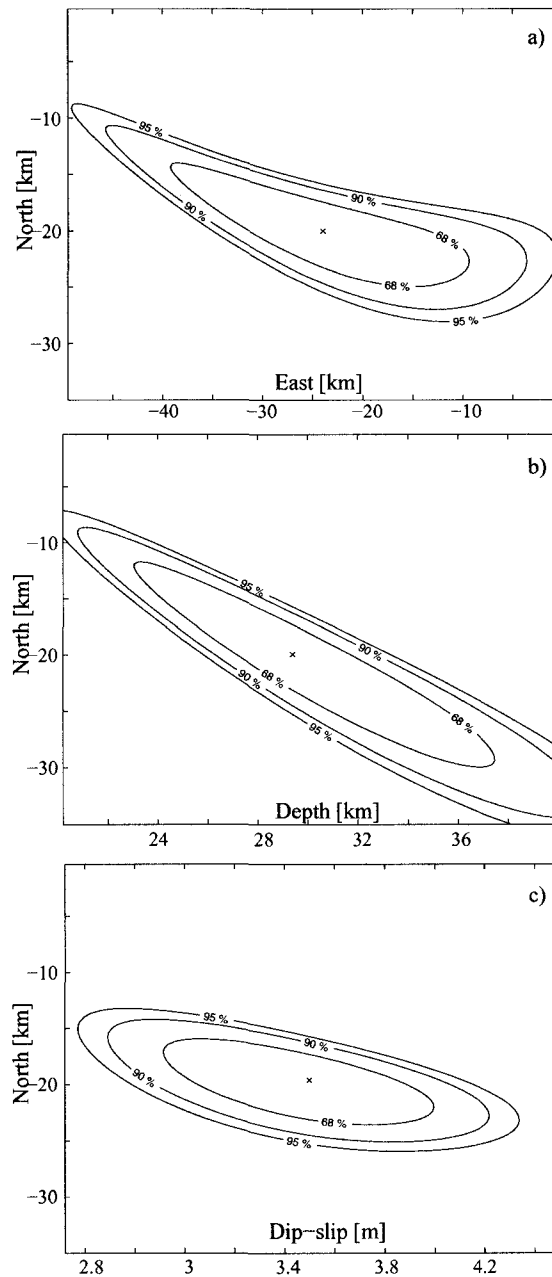


Figure 2.6.  $\Delta\chi^2$  for estimated model parameters. We estimate the optimal location (north, east and depth of the top of the fault) and slip on a fixed fault in elastic half space from the GPS data. Fixing two of four variables we estimate the  $\Delta\chi^2$  for a) the north relative to the east location of the fault; b) the north location relative to the depth (top) of the fault; c) the north location relative to slip on the fault. The north and east show distance from the hypocenter estimated by NEIC (13.049°N, 88.660°W).

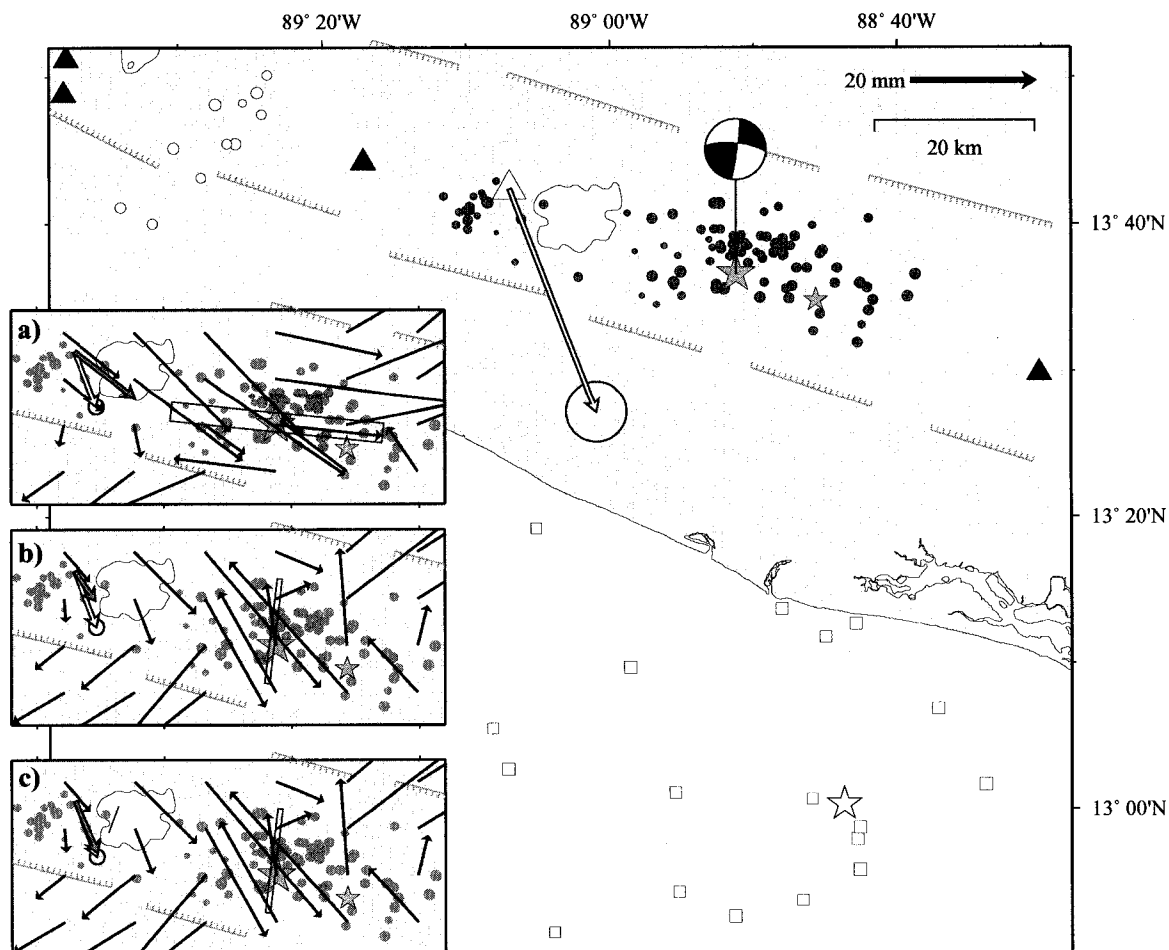


Figure 2.7. Coseismic displacement at the site SSIA in San Salvador from the  $M_W$  6.6 February 13 El Salvador earthquake (with 95% confidence ellipse). The displacement is shown relative to the station MANA. In the inset we show coseismic displacement estimates for three different test models. The black vectors show estimated displacement field for each model, gray vector shows estimated displacement at the site SSIA, and the white vector shows the actual measured coseismic displacement. We fix the strike and dip of the fault models to the fault plane solutions from Harvard CMT and assume depth of 5-15 km depth. a) Right-lateral strike-slip of 1 m on  $30 \text{ km} \times 10 \text{ km}$  fault plane. b) Left-lateral strike-slip of 2 m on  $15 \text{ km} \times 10 \text{ km}$  fault plane. c) Left-lateral strike-slip of 2 m on  $15 \text{ km} \times 10 \text{ km}$  fault plane in addition to a vertical  $4 \text{ km} \times 4 \text{ km}$  left-lateral fault (beneath Lake Ilopango), with a strike of  $20^\circ$  and 0.6 m slip. Aftershocks from February 13-16 (gray circles) are shown for reference. The main shock and the largest aftershock are shown with gray stars (CIG). Seismic activity in the month preceding the earthquake is shown with white circles (CIG) and squares (ISC).

slip of the earthquake. We were unable to reproduce displacement at the site within the  $2\sigma$  confidence region, both for right-lateral and left-lateral faults. The resulting displacements were either too small or had the wrong azimuth (Figure 2.7a-b).

The inability of simple slip models to reproduce the measured displacement at SSIA could suggest additional slip on a fault located closer to the site (see e.g. Figure 2.7c). Such triggered slip has been observed for other recent earthquakes. In 2000 an  $M_S$  6.6 earthquake in Iceland triggered slip on a fault 85 km from the epicenter, revealed later by InSAR and GPS measurements [Pagli *et al.*, 2003]. Triggered seismic activity was observed following the  $M_W$  6.6 El Salvador earthquake west of the GPS site, with earthquakes lining up on a NNE-SSW trending plane. Left-lateral earthquakes on NNE-SSW trending planes have occurred in the tectonic depression along the volcanic arc in the past. In 1986, an  $M_W$  5.2 earthquake ruptured a near vertical  $N32^\circ E$  trending fault plane in a left-lateral earthquake [White *et al.*, 1987].

Triggered seismic activity was also observed on February 17 with an  $M_L$  5.1 event occurring west of the  $M_W$  6.6 aftershock region. Aftershocks from the  $M_L$  5.1 event suggest a NNE-SSW trending fault plane (Figure 2.3e-g). On May 8 similar activity occurred just east of the main aftershock region of the  $M_W$  6.6 event with large aftershocks seemingly trending NNE-SSW (Figure 2.3i-j). A focal mechanism is not available for the February 17 event but the May 8 event has similar focal mechanism to the  $M_W$  6.6 event (Figure 2.3i) [Harvard CMT, 2001]. On January 14 and 24, prior to the February 13 activity, seismic activity was observed further east with several  $M_L$  3-4 events that seem to line up on a NNE-SSW trending plane. The location of these events on parallel NNE-SSW trending planes seems to indicate bookshelf style deformation along the depression, with left-lateral strike-slip faults accommodating right-lateral trench-parallel deformation. Previous upper crustal earthquakes in El Salvador have sometimes occurred in a sequence of earthquakes, e.g. in 1951 three earthquakes  $M_S$  5.5 to 6.0 occurred on May 6-7 within minutes of each other [Ambraseys and Adams, 2001]. Similar activity has been observed in southwest Iceland where parallel N-S trending right-lateral strike-slip faults accommodate left-lateral transform motion in the region [Einarsson, 1991; Árnadóttir *et al.*, 2003]. Studies from Nicaragua indicate that a similar mechanism controls the trench-parallel block motion resulting from the oblique subduction along the Middle America Trench [La Femina *et al.*, 2002]. La Femina *et al.*

[2002] suggest that the bookshelf faulting on northeast striking left-lateral faults accommodate the trench-parallel deformation. The width of the aftershock zone following the  $M_W$  6.6 El Salvador earthquake fits well with 10-20 km long NNE-SSW trending faults lying parallel along the zone. Seismic activity following the earthquake does seem to suggest bookshelf faulting on NNE-SSW trending left-lateral faults.

The timeseries plot of SSIA relative to MANA (Figure 2.6) reveal a post earthquake signal following the  $M_W$  6.6 earthquake. The signal could be attributed to the seismic activity following the  $M_W$  6.6 just east of the GPS station.

## 2.5 Seismicity and Stress Changes Following the January 13 Earthquake

We use changes in Coulomb failure stress ( $\Delta CFS$ ) to study the effect of the January 13 earthquake on stress in the surrounding crust and compare to the observed seismicity. The Coulomb failure stress changes are a quantitative way of estimating if an earthquake brings neighbouring faults closer to or further from failure. Based on the assumption on Coulomb failure criteria for rock (e.g. *Jaeger and Cook* [1969]), the Coulomb failure stress change is given as [*Harris, 1998*]:

$$\Delta CFS = \Delta\tau + \mu(\Delta\sigma_n + \Delta p) \quad (2.1)$$

$$\approx \Delta\tau + \mu'\Delta\sigma_n \quad (2.2)$$

where  $\Delta\tau$  is the change in shear stress in the slip direction on the plane,  $\Delta\sigma_n$  is the change in normal stress,  $\Delta p$  is the change in pore pressure and  $\mu$  is the friction coefficient.  $\mu'$  is the "apparent coefficient of friction" that includes the effect of the pore pressure which changes with time due to pore fluid diffusion. A positive  $\Delta CFS$  would indicate that an earthquake loaded a fault plane, bringing it closer to failure, whereas negative  $\Delta CFS$  would relax the fault plane, bringing it further from failure.

Previous studies of Coulomb failure stress changes following large earthquakes have shown a correlation between the sign of Coulomb failure stress changes and the pattern of aftershocks following the earthquakes (e.g. *King et al.* [1994]). Some studies have also shown a long term correlation between seismicity rate changes at regional ( $> 1$  fault length) distances and simple Coulomb failure stress change calculations [*Wyss and Wiemer, 2000*].

The January 13 earthquake was a normal fault earthquake occurring within the subducting Cocos plate. We use the simple fault plane estimated for the earthquake from the GPS data to estimate static stress changes along the seismically active tectonic depression in the overriding Caribbean plate. We use the program Coulomb 2.6 [Toda and Stein, 2002] to estimate the stress changes. We also calculated Coulomb stress changes for thrust events on the main plate interface. Unfortunately the large scatter in mainshock hypocenter locations suggests that offshore earthquake locations are probably too uncertain to draw conclusions. The events onland were located by a local seismic network and should be much more precise.

A month following the  $M_W$  7.7 earthquake an  $M_W$  6.6 strike-slip earthquake occurred in the overriding Caribbean plate, about 75 km distant from the larger event. Prior to the  $M_W$  6.6 earthquake, seismicity was observed  $\sim 65$  km west of the  $M_W$  6.6 strike-slip event, with several  $M_L$  3-4 events occurring on January 14 and 24. The timing of these events and the  $M_W$  6.6 earthquake suggests connection to the  $M_W$  7.7 earthquake. They are located  $> 1$  fault length from the epicenter, outside the main aftershock region, within another tectonic plate, and of a different mechanism (strike-slip) than the main  $M_W$  7.7 event. This could suggest static stress triggering.

We estimate Coulomb failure stress changes following the  $M_W$  7.7 earthquake, for strike-slip faults at 10 km depth. We use our coseismic slip model and estimate the  $\Delta$ CFS for both right-lateral strike-slip faults striking  $280^\circ$  and left-lateral strike-slip faults striking  $10^\circ$ . We assume vertical dip and use  $\mu' = 0.4$  and  $\nu = 0.25$  (Figure 2.8 and 2.9). Our model suggests that both right-lateral ( $280^\circ$ ) and left-lateral ( $10^\circ$ ) faults in the  $M_W$  6.6 epicentral region were brought closer to failure by the  $M_W$  7.7 earthquake, with an increase in  $\Delta$ CFS in the range of 0.01 to 0.03 MPa. The seismic activity on January 14 and January 24 falls within the estimated stress shadow from the earthquake for  $10^\circ$  left-lateral faults but the locations of these events indicate a NNE-SSW trending fault plane. Our estimated static stress changes are based on assumptions for  $\mu'$  (friction and pore pressure) and Poisson's ratio. We find that with  $\mu' \geq 0.75$  the estimated  $\Delta$ CFS becomes positive, thus the earthquake could have brought left-lateral faults in that region (striking  $10^\circ$ ) closer to failure (Figure 2.10). However regardless of the apparent coefficient of friction, static stress changes for this region are small,  $\Delta$ CFS  $< 0.01$  MPa.



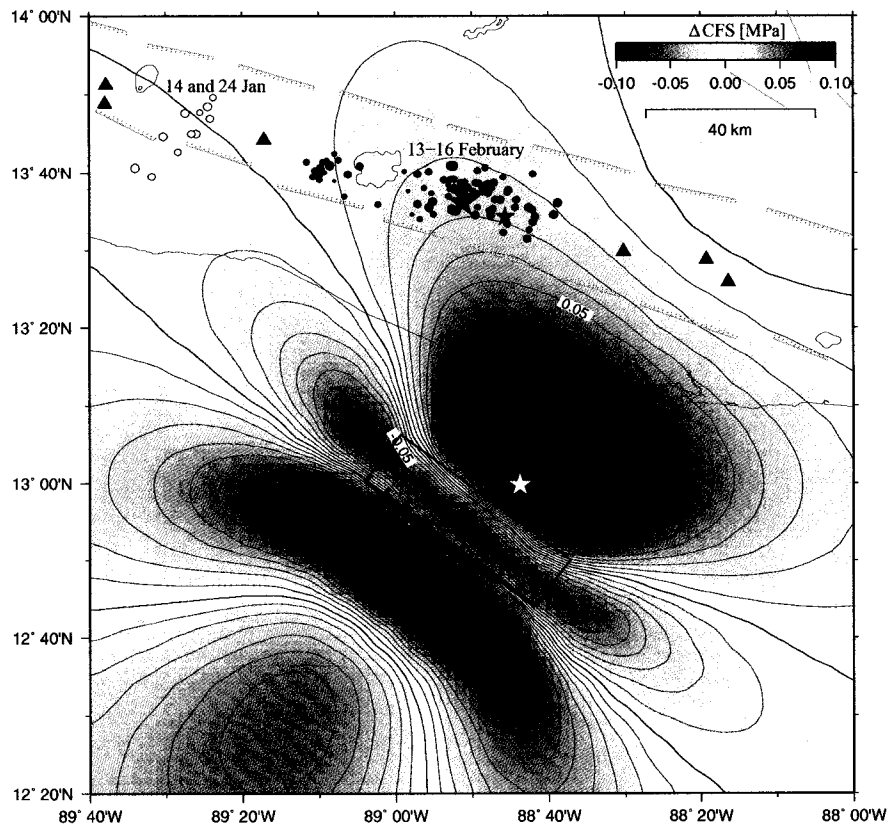


Figure 2.8. Coulomb failure stress change estimated from the  $M_W$  7.7 earthquake for right-lateral strike-slip faults at 10 km depth, with a strike of  $280^\circ$  and dipping  $90^\circ$ . Red stars show the  $M_W$  6.6 event and its largest aftershock, blue circles show earthquakes occurring in the upper crust from 13-16 of February, and white circles show events occurring on the 14 and 24 of January (CIG). The white star shows the estimated location of the  $M_W$  7.7 event from ISC.

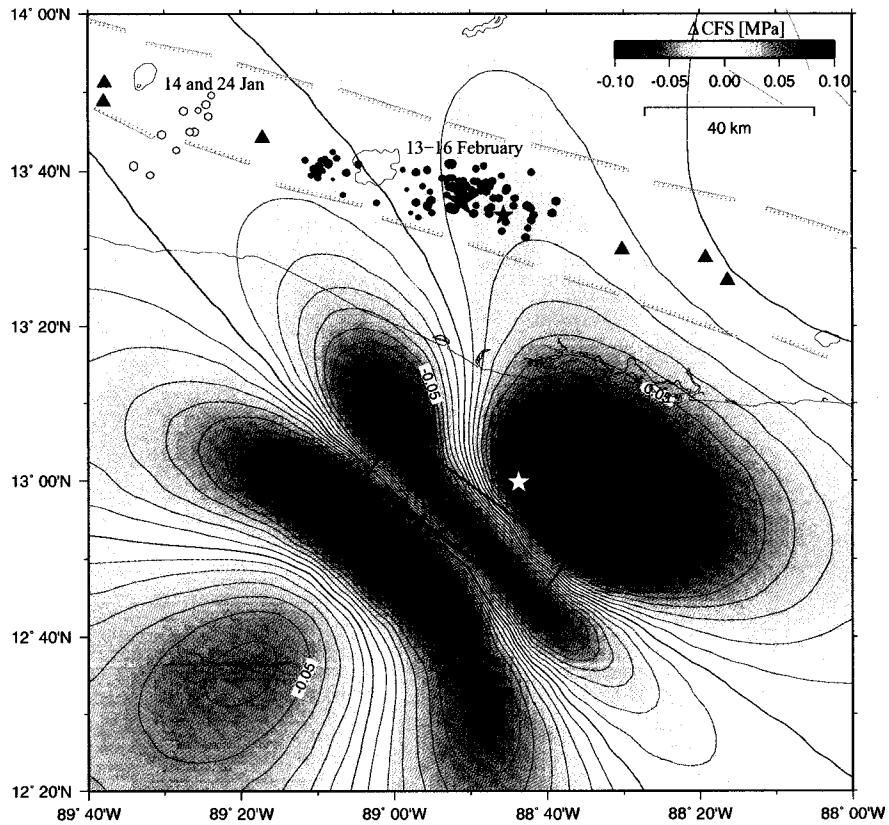


Figure 2.9. Coulomb failure stress change estimated from the  $M_W$  7.7 earthquake for left-lateral strike-slip faults at 10 km depth, with a strike of  $10^\circ$  and dipping  $90^\circ$ . Red stars show the  $M_W$  6.6 event and its largest aftershock, blue circles show earthquakes occurring in the upper crust from 13-16 of February, and white circles show events occurring on the 14 and 24 of January (CIG). The white star shows the estimated location of the  $M_W$  7.7 event from ISC.

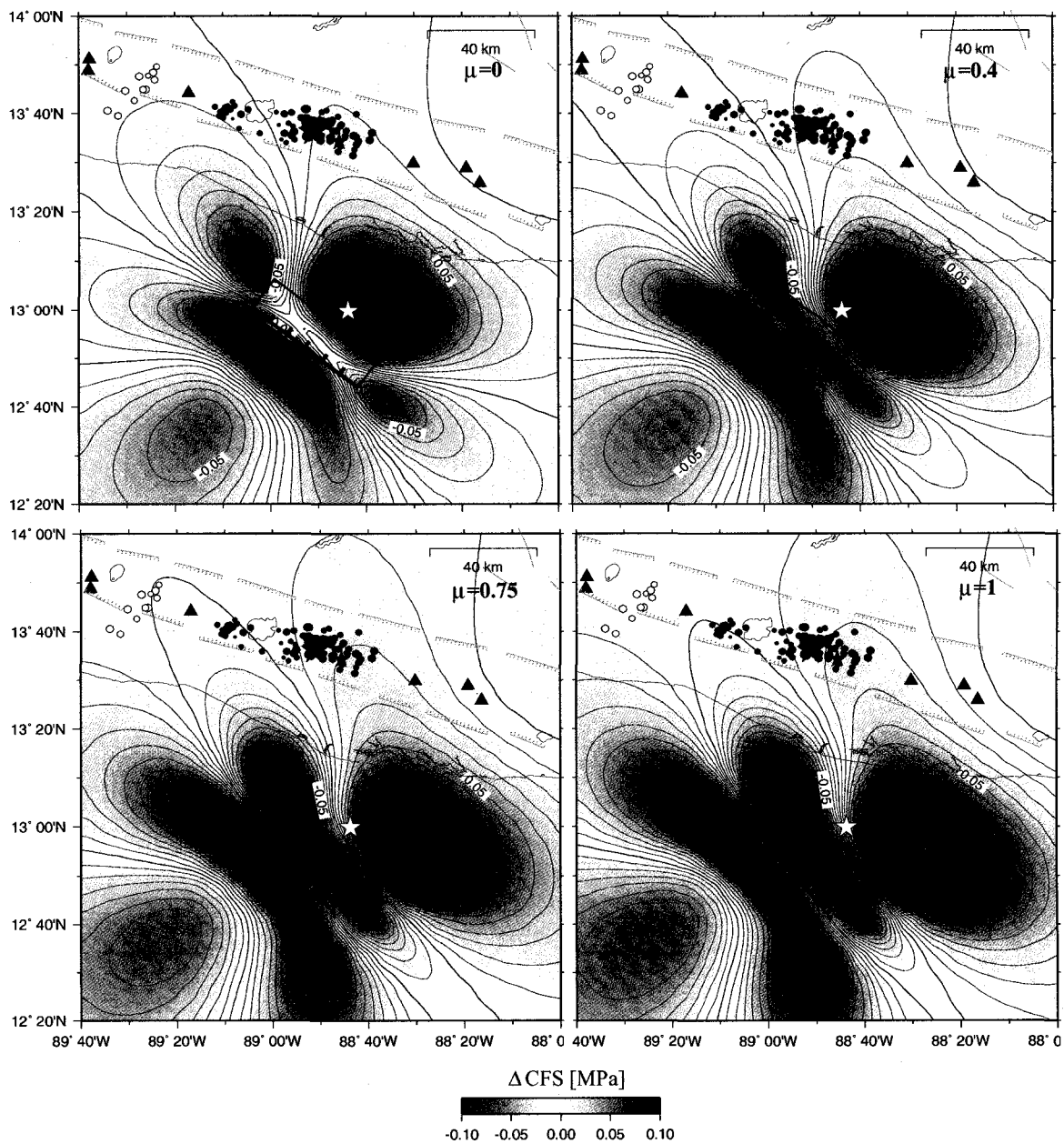


Figure 2.10. Effects of the coefficient of friction. Coulomb failure stress change estimated from the  $M_W$  7.7 earthquake for left-lateral strike-slip faults at 10 km depth, with a strike of  $10^\circ$  and dipping  $90^\circ$  for four different friction values, 0, 0.4, 0.75, and 1.

Following the  $M_W$  6.6 earthquake, aftershocks were detected in a  $10 \text{ km} \times 30 \text{ km}$  long zone east of Lake Ilopango (Figure 2.3). Seismic activity was also observed in San Salvador following the earthquake, west of the main aftershock region (west of Lake Ilopango, Figure 2.3d). The activity suggests that the  $M_W$  6.6 event triggered earthquakes on a NNE-SSW trending plane. On February 17 an  $M_L$  5.1 earthquake occurred just west of this activity, with aftershocks lining up on a parallel plane, trending NNE-SSW (Figure 2.3e-f). This region was in the stress shadow from the  $M_W$  7.7 earthquake, prior to the  $M_W$  6.6 earthquake (Figure 2.10), with no earthquakes being recorded from January 13 to February 13 (CIG). However after the  $M_W$  6.6 earthquake this region became very active seismically for a few weeks (Figure 2.3e-h). We use simple models for the  $M_W$  6.6 earthquake combined with our model for the  $M_W$  7.7 earthquake to estimate static stress change on left-lateral faults in the region (with a strike of  $10^\circ$  and vertical dip). We assume that the epicenter estimated by CIG is at the center of the rupture and estimate both the effect from a simple right-lateral and simple left-lateral rupture. For the right-lateral fault we assume 1 m slip on a  $30 \text{ km} \times 10 \text{ km}$  fault plane, striking  $280^\circ$ . For the left-lateral fault plane we assume 2 m slip on a  $15 \text{ km} \times 10 \text{ km}$  fault plane with a strike of  $10^\circ$ . We assume vertical dip for both fault planes and 5-15 km depth. Both fault models seem to suggest that left-lateral faults (striking  $10^\circ$ ) in this region had been brought closer to failure by the  $M_W$  6.6 earthquake with  $\Delta\text{CFS} > 0.01 \text{ MPa}$  (Figure 2.11).

A few months following the February 13 and February 17 activity another  $M_L$  5.1 strike-slip earthquake occurred in the region, followed by several  $M_L \geq 4$  aftershocks. This event occurred within a positive  $\Delta\text{CFS}$  region (0.01-0.03 MPa) from the  $M_W$  7.7 earthquake, right at the edge of the aftershock zone from the  $M_W$  6.6 event. Our model suggests that after the  $M_W$  6.6 earthquake the epicenter was in a stress shadow, thus retarding potential slip on left-lateral faults in that region. However it is close to a boundary between positive and negative  $\Delta\text{CFS}$ , so small changes in the source model could move them into a positive quadrant.

## 2.6 Conclusions

We have estimated the coseismic GPS displacements for the  $M_W$  7.7 and  $M_W$  6.6 earthquakes at permanent GPS stations in Central America. For the  $M_W$  7.7 event we see 10-15

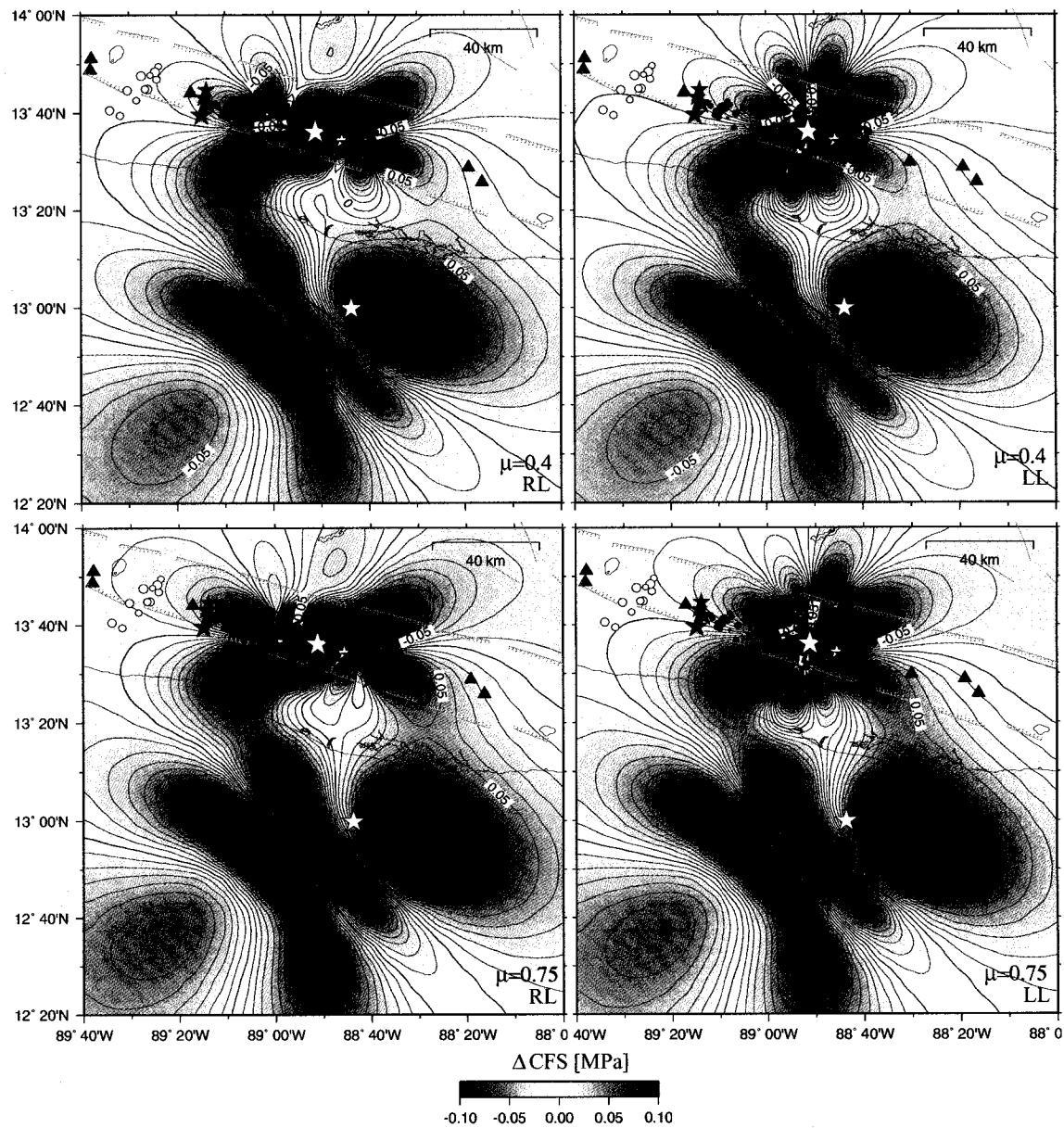


Figure 2.11. Coulomb failure stress change estimated from the  $M_W$  6.6 earthquake for left-lateral strike-slip faults at 10 km depth, with a strike of  $10^\circ$  and dipping  $90^\circ$

mm coseismic displacement at three sites up to 200 km distance from the epicenter. Despite the small number of GPS sites and relatively long distances between the sites we can use the estimated coseismic displacements to reveal important aspects of the earthquakes. The data indicate a 3.5 m normal faulting on a fixed (50 km  $\times$  25 km) fault plane at about 30-50 km depth. Our slip estimate for the  $M_W$  7.7 event fits well with the estimates from Vallée *et al.* [2003]. Our model location falls within the general cluster of location estimates based on seismic data. The  $M_W$  6.6 earthquake occurred in a region of increased  $\Delta$ CFS from the  $M_W$  7.7 earthquake by 0.01 to 0.03 MPa. The  $M_W$  6.6 event further modified the static stress, triggering slip on faults west of the main aftershock region. We suggest that the seismic activity along the tectonic depression is related to bookshelf-style deformation, with left-lateral strike-slip on multiple NNE-SSW trending strike-slip faults that accommodate the right-lateral deformation in the region. This has been suggested for deformation in the tectonic depression in Nicaragua, east of El Salvador [La Femina *et al.*, 2002].

## 2.7 Acknowledgments

This study would not have been possible without the GPS data from CORS and earthquake locations from CIG and ISC. We thank Douglas Christensen and Evelyn Price for discussions.

## References

- Ambraseys, N. N., and R. D. Adams (2001), *The Seismicity of Central America: A Descriptive Catalogue 1898-1995*, Imperial College Press, London.
- Árnadóttir, T. S. Jónsson, R. Pedersen, and G. B. Gudmundsson (2003), Coulomb stress changes in the South Iceland seismic zone due to two large earthquakes in June 2000, *Geophys. Res. Lett.*, *30*(5), 1205, doi:10.1029/2002GL016495.
- Bommer, J., B. Benito, M. Ciudad-Real, A. Lemoine, M. López-Menjívar, R. Madariaga, J. Mankelow, P. Méndez de Hasbun, W. Murphy, M. Nieto-Lovo, C. Rodríguez-Pineda, and H. Rosa (2002), The El Salvador Earthquakes of January and February 2001: Context, characteristics and implications for seismic risk, *Soil Dyn. Earthq. Eng.*, *22*(5), 398-418.
- Burkart, B., and S. Self (1985), Extension and rotation of crustal blocks in northern Central America and effect on the volcanic arc, *Geology*, *13*, 22-26.

- DeMets, C., R. G. Gordon, D. F. Argus, and S. Stein (1994), Effect of recent revisions to the geomagnetic reversal time scale on estimates of current plate motions, *Geophys. Res. Lett.*, *21*, 2191-2194.
- Dewey, J. W., and G. Suárez (1991), Seismotectonics of Middle America, in *Neotectonics of North-America*. edited by D. B. Slemmons, E. R. Engdahl, M. D. Zoback, and D. D. Blackwell, pp. 309-321, The Geological Society of America, Inc.
- EERI (2001), Preliminary observations on the El Salvador earthquake of January 13 and February 13, 2001, edited by C. Paulson and J. Bommer, *EERI Special Earthquake Report*.
- Einarsson, P. (1991), Earthquakes and present day tectonism in Iceland, *Tectonophysics*, *189*, 261-279.
- Harris, R. A. (1998), Introduction to special section: Stress triggers, stress shadows, and implications for seismic hazard, *J. Geophys. Res.*, *103*, 24347-24358.
- Harvard CMT Catalogue (2001), *On-line Bulletin*, <http://www.seismology.harvard.edu/-CMTsearch.htm>, Harvard, USA.
- ISC, International Seismological Centre (2001), *On-line Bulletin*, <http://www.isc.ac.uk/-Bull>, Internatl. Seis. Cent., Thatcham, United Kingdom.
- Jaeger, J. C., and N. G. W. Cook (1969), *Fundamentals of Rock Mechanics*, Chapman and Hall, London.
- King, G. C. P., R. S. Stein, and J. Lin (1994), Static stress changes and the triggering of earthquakes, *Bull. Seismol. Soc. Am.*, *84*, 935-953.
- La Femina, P. C., T. H. Dixon, and W. Strauch (2002), Bookshelf faulting in Nicaragua, *Geology*, *30*(8), 751-754.
- NEIC, USGS Earthquake Information Center (2001), *On-line data base, 1973-Present*, <http://wwwneic.cr.usgs.gov/neis/epic/epic.html>, United States Geological Survey, USA.
- Okada, Y. (1985), Surface deformation due to shear and tensile faults in a halfspace, *Bull. Seis. Soc. Amer.*, *75*(4), 1135-1154.
- Pagli, C., R. Pedersen, F. Sigmundsson, and K. L. Feigl (2003), Triggered fault slip on June 17, 2000 on the Reykjanes Peninsula, SW-Iceland captured by radar interferometry, *Geophys. Res. Lett.*, *30*(6), 1273, doi:10.1029/2002GL015310.
- Snay, R. A. (2000), The national and cooperative CORS system in 2000 and beyond, *Proc. INP GPS-2000*, Salt Lake City, UT, 55-58, Sep. 19-22.

- Spofford, P. R., and N. D. Weston, (1998), National geodetic survey continuously operating reference station project. Status and plan, *ACSM Bulletin*, 172, 20-25.
- Toda, S., and R. S. Stein (2002), Response of the San Andreas fault to the 1983 Coalinga-Nuñez Earthquake: An application of interaction-based probabilities for Parkfield, *J. Geophys. Res.*, 107, 10.1029/2001JB000172.
- Vallée M., M. Bouchon, and S. Y. Schwartz (2003), The 13 January 2001 El Salvador earthquake, A multidata analysis, *J. Geophys. Res.*, 108(B4), 2203, doi:10.1029/2002JB001922.
- Wells, D. L., and K. J. Coppersmith (1994), New empirical relationships among magnitude, rupture length, rupture width, rupture area, and surface displacement, *Bull. Seismol. Soc. Am.*, 84, 974-1002.
- White, R. A. (1991), Tectonic implications of upper-crustal seismicity in Central America, in *Neotectonics of North-America*, edited by D. B. Slemmons, E. R. Engdahl, M. D. Zoback, and D. D. Blackwell, pp. 232-338, The Geological Society of America, Inc.
- White, R. A., and D. H. Harlow (1993), Destructive upper-crustal earthquakes of Central America since 1900, *Bull. Seis. Soc. Amer.*, 83, 1115-1142.
- White, R. A., D. H. Harlow, and S. Alvarez (1987), The San Salvador earthquake of October 10, 1986-Seismological aspects and other recent local seismicity, *Earthquake Spectra*, 3, 419-434.
- Wyss, M. and S. Wiemer (2000), Change in the probability for earthquakes in southern California due to the Landers magnitude 7.3 earthquake, *Science*, 290.



## Chapter 3

### Coseismic Slip Distribution of the 2002 $M_W$ 7.9 Denali Fault Earthquake, Alaska, Determined from GPS Measurements <sup>2</sup>

#### 3.1 Abstract

On 3 November 2002 an  $M_W$  7.9 earthquake occurred in central Alaska. The earthquake ruptured portions of the Susitna Glacier, Denali, and Totschunda faults. Inversion of the GPS-measured displacement field indicates that the event was dominated by a complex, right-lateral strike-slip rupture along the Denali fault. GPS sites closest to the epicenter show the effect of thrust motion on the Susitna Glacier fault. The preferred coseismic slip model, with  $M_W$  7.8, indicates relatively low slip on the western part of the rupture and high slip from about 60 km east of the hypocenter extending to the junction of the Denali and Totschunda faults. We find mostly shallow slip from the surface to 15 km depth, but the inversion suggests one large deep slip patch about 110 km east of the hypocenter. Our model predicts surface slip in good agreement with surface geological observations, where model resolution is good.

#### 3.2 Introduction

On 3 November 2002, an  $M_W$  7.9 earthquake occurred on the Denali fault, central Alaska. The earthquake was preceded by an  $M_W$  6.7 right-lateral strike-slip earthquake on 23 October, with its epicenter only 22 km west of the  $M_W$  7.9 epicenter [Eberhart-Phillips *et al.*, 2003]. These earthquakes are the largest earthquakes to occur on the Denali fault in recorded history. The 2002 Denali fault earthquake ruptured the surface for about 340 km along three major faults. It first ruptured 40 km along the Susitna Glacier fault, a thrust fault south of and splaying off of the Denali fault. Then it ruptured for 220 km along the Denali fault, with nearly pure right lateral slip, to the junction of the Denali and Totschunda faults where it stepped over to the Totschunda fault and ruptured another 80 km [Eberhart-Phillips *et al.*, 2003].

Many existing GPS points in Alaska were surveyed following the  $M_W$  7.9 earthquake. Here we present coseismic displacements for the  $M_W$  7.9 Denali fault earthquake for sites

---

<sup>2</sup>Published under the same title with authors S. Hreinsdóttir, J. T. Freymueller, H. J. Fletcher, C. F. Larsen, and R. Bürgmann in *Geophys. Res. Lett.*, 30(13), 1670, doi:10.1029/2003GL017447, 2003.

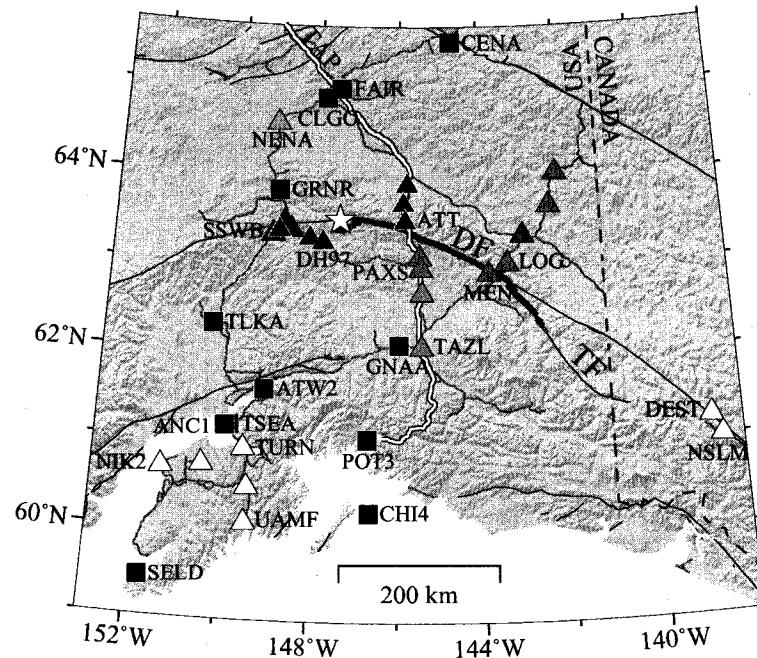


Figure 3.1. GPS sites used in this study. Triangles show campaign GPS sites and squares show permanent GPS sites. Black sites were measured within a day of the earthquake, white sites were measured more than a week after the earthquake. Shades of gray show intermediate times. The epicenter of the  $M_W$  7.9 Denali fault earthquake is shown with a white star and its surface rupture is shown with the thick gray line [Eberhart-Phillips *et al.*, 2003]. Black lines indicate major faults in Alaska, gray lines show roads, and the Trans-Alaska oil pipeline (TAP) is shown with a white line. Names of selected sites are shown. Note that 6 GPS sites are located between DH97 and SSWB, W and SW of the epicenter. DF-Denali fault, TF-Totschunda fault.

measured within one week of the earthquake and permanent GPS sites in Alaska. We invert these GPS data to determine the coseismic slip distribution of the earthquake.

### 3.3 GPS Data and Analysis

We use data from 40 GPS sites in this study (Figure 3.1, Table A.1); 28 campaign GPS sites from the interior of Alaska (21), south central Alaska (5), and the Yukon (2) (triangles) and 12 permanent GPS sites in the interior and south central Alaska (black squares).

To limit the impact of postseismic deformation on the coseismic displacements we mostly used data from sites that were surveyed within one week of the  $M_W$  7.9 earthquake. To increase spatial coverage of site distribution for the inversion we included data from a few

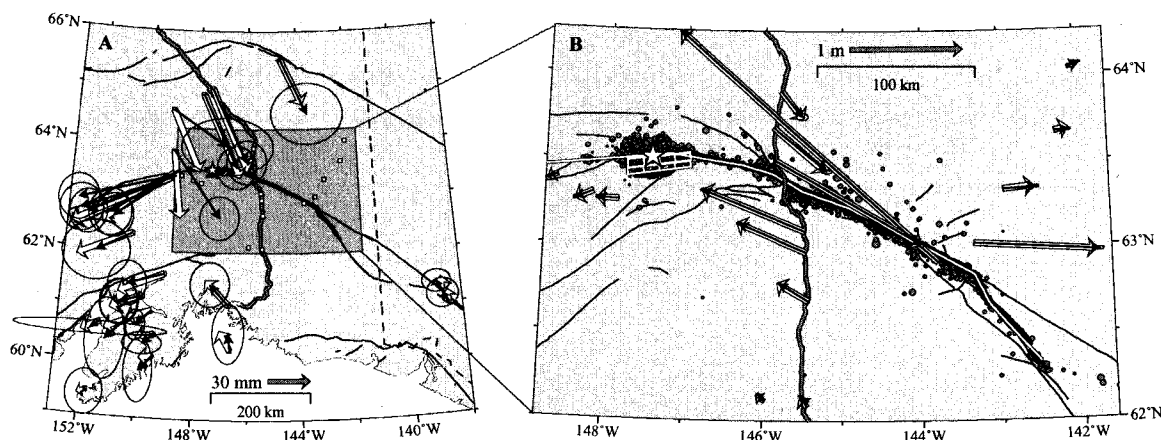


Figure 3.2. Coseismic displacements (black) from the  $M_W$  7.9 earthquake with 95% confidence ellipses and inversion results (white), for far-field (A) and near-field (B) sites. The white star shows the  $M_W$  7.9 epicenter, circles show relocated aftershocks [Ratchkovski *et al.*, 2003], thick line indicates earthquake rupture [Eberhart-Phillips *et al.*, 2003]. The white line (B) shows the model fault used in this study. Displacements are shown at two different scales in the two panels.

far-field sites measured about 10 days after the earthquake. We selected two sites in the Yukon that were closest to the rupture south-east of the fault, and sites in south central Alaska that had at least two days of post earthquake measurements and antennas centered and leveled at pickup.

All the sites used here had multiple years of measurements prior to the earthquake, and most had precise velocities [Fletcher, 2002; Zweck *et al.*, 2002]. Twelve of these sites were surveyed following the 23 October  $M_W$  6.7 earthquake, all within 80 km of its epicenter. Other sites were last surveyed from 2 months to 2 years prior to the earthquake. In addition to these measurements, 12 permanent GPS sites were operating within 500 km of the epicenter.

We analyzed the GPS data using the GIPSY/OASIS II software (release 5) developed at the Jet Propulsion Laboratory (JPL) using the JPL non-fiducial orbits. Data from each day were processed separately to obtain loosely constrained daily network solutions. The daily GPS solutions were then transformed into the International Terrestrial Reference Frame 1997 (ITRF97) [Boucher *et al.*, 1999] using about 15 global reference sites (variable day to day) to define the 7 parameter Helmert transformation [Freymueller *et al.*, 2000].

We used two different methods to estimate displacements due to the earthquake. For permanent sites and sites measured following the  $M_W$  6.7 earthquake we averaged the four days prior to and four days following the earthquake and estimated displacements from these merged solutions. For other sites we fit a line plus offset to the station time series. We only used the first 3 days of post-earthquake measurements at each site to limit postseismic signal in the data. The uncertainties in the displacements were scaled based on the scatter in the measurements, considering each component independently.

The GPS data show a right lateral deformation field (Figure 3.2). North of the fault, sites show eastward motion and sites to the south show westward motion, relative to ITRF97. The largest measured horizontal displacement of  $3.107 \pm 0.004$  m was at a site (MEN) just south of the main strand of the Denali fault, near where the maximum surface offset was measured in the eastern part of the rupture [Eberhart-Phillips *et al.*, 2003]. Observed vertical displacements were generally smaller than the horizontal, indicating mostly strike slip motion (Figure 3.3). With a few exceptions, sites north of the fault moved up and sites south of the fault moved down. Only 6 sites had more than 5 cm of measured vertical displacement and all but one had less than 10 cm. The maximum subsidence of  $0.246 \pm 0.007$  m was measured at MEN. Sites southwest of the epicenter have a more northerly coseismic displacement than expected for pure strike slip motion, supporting seismic and geological data that indicate thrusting along the Susitna Glacier fault [Eberhart-Phillips *et al.*, 2003].

### 3.4 Inversion for Fault Slip Model

We used a 9 plane geometric approximation to the surface rupture of the Denali and Totschunda faults for the inversion of the GPS data. The model was extended to the west, using the mapped Denali fault trace, in order to span both the aftershock region for the  $M_W$  6.7 and  $M_W$  7.9 earthquakes and thus test for re-rupture of the  $M_W$  6.7 segment. Each plane was split into  $3 \text{ km} \times 3 \text{ km}$  tiles extending down to 18 km depth with a dip of  $90^\circ$  in accord with teleseismic body wave analysis [Kikuchi and Yamanaka, 2002]. We applied Laplacian smoothing between the tiles, with a zero slip boundary condition below 18 km depth. For the Susitna Glacier thrust fault we added 8 tiles with a strike of  $81^\circ$ . For the lower 4 tiles, intersecting the Denali fault at about 8 km depth, a dip of  $48^\circ$  was as-

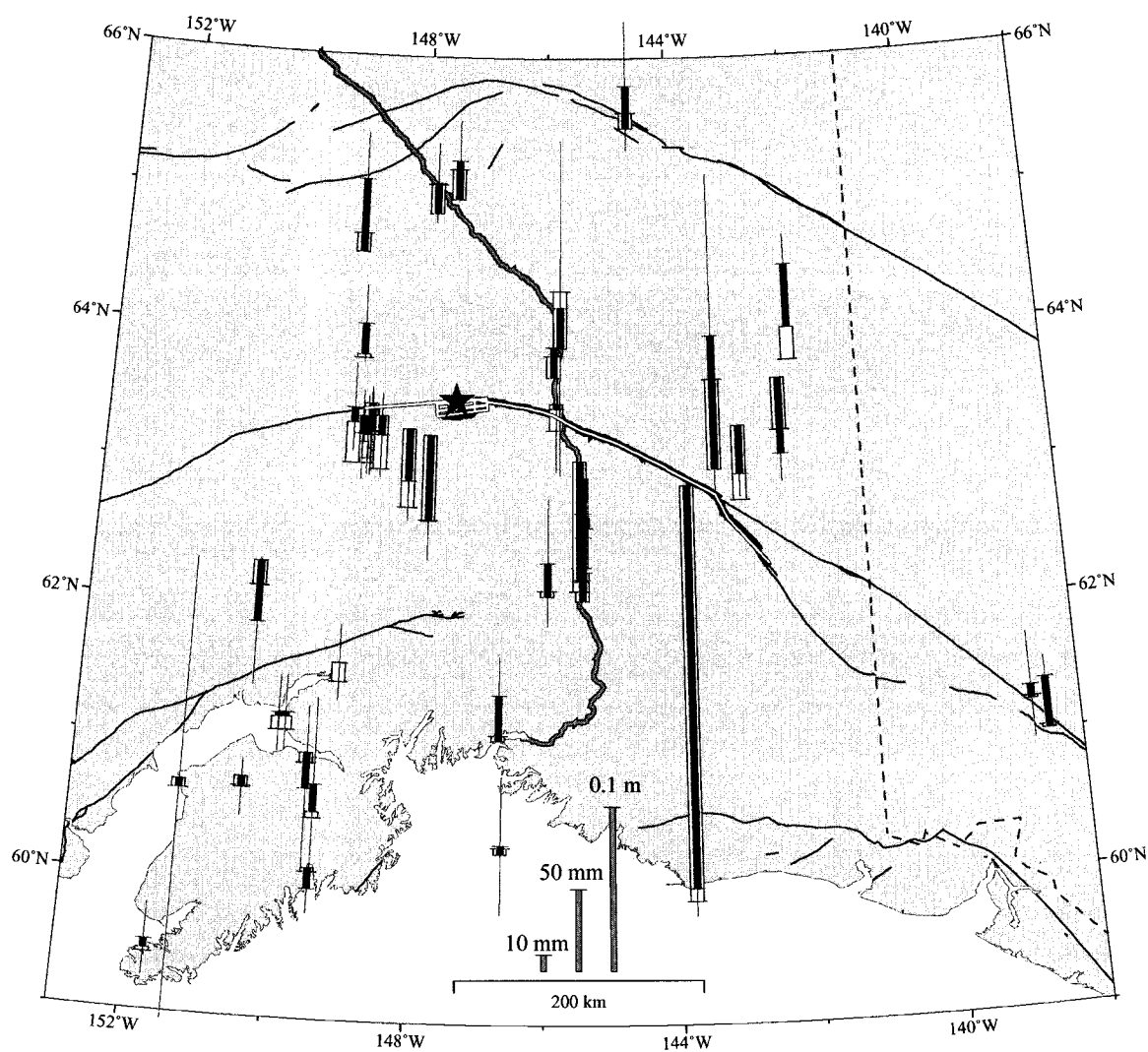


Figure 3.3. Vertical coseismic displacements (blue) from the  $M_W$  7.9 earthquake and inversion results (yellow). The star shows the  $M_W$  7.9 epicenter, thick red line indicates earthquake rupture [Eberhart-Phillips *et al.*, 2003] and the white line shows the model fault used in this study. Black lines indicate major faults in Alaska and the the Trans-Alaska oil pipeline (TAP) is shown with a gray line.

sumed based on the focal mechanism from the local network [Eberhart-Phillips *et al.*, 2003]. The upper 4 tiles, intersecting the surface at the mapped surface rupture, were fixed to 25° dip to match field observations [Eberhart-Phillips *et al.*, 2003], with Laplacian smoothing between the tiles.

We used a bounded variable least squares (BVLS) inversion [Stark and Parker, 1995] to estimate coseismic slip on each model fault tile, allowing only right lateral slip on the Denali and Totschunda faults and only thrust motion on the Susitna Glacier fault (both assumptions are consistent with seismic results). We computed the Green’s functions,  $\mathbf{G}$ , relating slip on each fault tile,  $s_i$ , to displacement at a GPS site,  $\vec{d}_j$ , assuming an elastic half space and a Poisson’s ratio of 0.25 [Okada, 1985]. For the inversion we used displacements relative to the southernmost station in the network, SELD. We used 117 data to estimate 770 model parameters, so an additional constraint such as smoothing is required to make the inversion stable. We measured roughness using the Laplacian operator,  $\mathbf{L}$ , weighted roughness using a smoothing factor  $\beta$ , and minimized the (unitless) weighted residual sum of squares (WRSS) and the roughness of the model:

$$\underbrace{\|\mathbf{W}(\mathbf{G}\vec{s} - \vec{d})\|^2}_{\text{mis fit}} + \beta^2 \underbrace{\|\mathbf{L}\vec{s}\|^2}_{\text{roughness}} \quad (3.1)$$

( $\mathbf{W}^T\mathbf{W} = \Sigma^{-1}$  where  $\Sigma$  is the GPS data covariance matrix.)

Changing  $\beta$  changes the importance assigned to data fit and smoothness, and produces a family of models with varying misfit and roughness (Figure 3.4). We want to select a smoothing factor for which the solution fits the data well, but is not excessively rough. Selecting the smoothing factor based only on a tradeoff curve can be highly subjective, so we also used the Cross-Validation Sum of Squares (CVSS) to determine the most reasonable smoothing factor [Matthews and Segall, 1993; Freymueller *et al.*, 1994]. The CVSS is a measure of the model’s ability to predict observations. Each station in turn is taken out of the data set and its displacement predicted based on a model fit to the other data. The CVSS is the sum of squares of the predicted residuals. In this case, the three stations with the largest coseismic displacements (MEN, LOG, and ATT) turned out not to be predictable by the other stations and had prediction residuals 1-2 orders of magnitude larger than the sum of squares for all other sites. We therefore decided to use the CVSS test without these

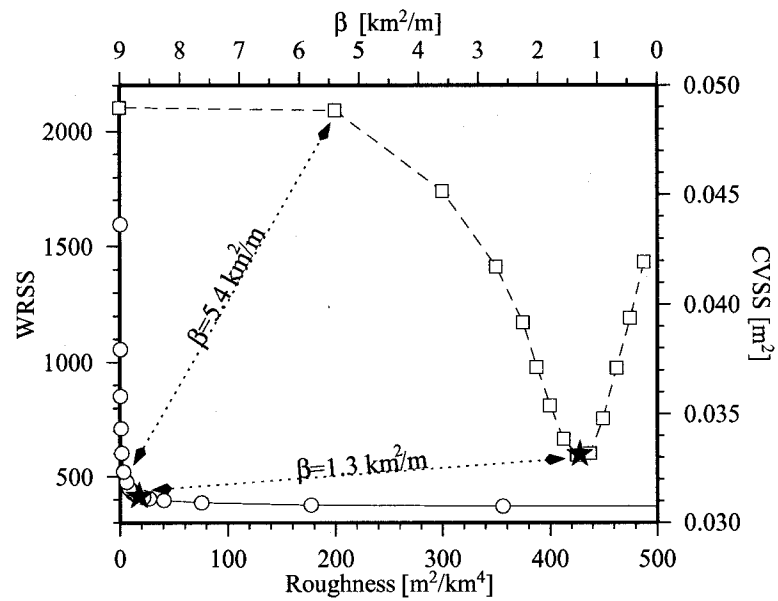


Figure 3.4. Trade-off curve between roughness and misfit (circles and solid line) and the CVSS as function of smoothing factor (squares with dashed line). Dotted lines connect two models with the same smoothing factor. We exclude the three sites with the largest coseismic displacement in estimating the CVSS. The stars show the preferred model, with smoothing of  $\beta = 1.3 \text{ km}^2/\text{m}$ .

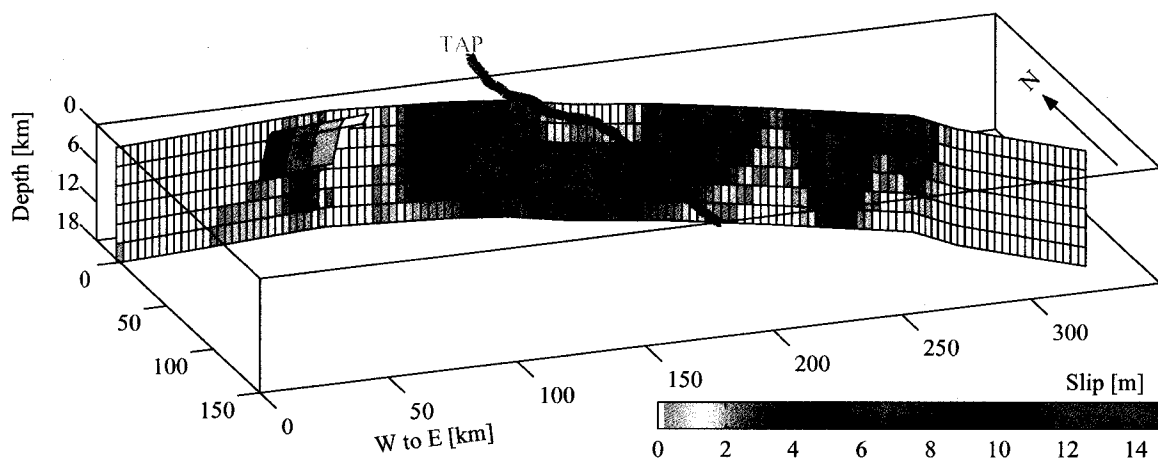


Figure 3.5. Coseismic slip distribution for the  $M_W$  7.9 Denali fault earthquake for the preferred model. The model has up to 15 m of right lateral slip along the Denali fault and up to 4 m of thrusting on the Susitna Glacier fault. Most slip is found above 12-15 km depth, but we find a deep slip patch just east of where the pipeline (TAP) crosses the fault. The star indicates the hypocenter of the  $M_W$  7.9 earthquake, located at the Sustina Glacier thrust fault.

three sites. This gives a minimum CVSS for  $\beta \sim 1.3 \text{ km}^2/\text{m}$  which also gives a reasonable roughness versus misfit tradeoff (stars in Figure 3.4). The three sites excluded in the CVSS analysis are located in very sensitive locations for the inversion. MEN and LOG are closest to where the maximum geological offset was measured and are relatively isolated from other sites (40 km from the next site). ATT is located where geological observations indicate a gradient in the surface offset. This indicates that we might benefit from the use of spatially variable smoothing, but for this paper we restrict ourselves to a constant smoothing factor. The preferred coseismic slip model is shown in Figure 3.5. The corresponding predicted coseismic displacements are shown in Figure 3.2 (white vectors).

### 3.5 Discussion and Conclusions

The modeled slip distribution varies considerably from west to east along the Denali fault. Relatively low slip is estimated for the westernmost 60 km of the rupture but further east, to the junction of the Denali and Totschunda faults, high slip is resolved. Little to no slip is found on the Totschunda fault but up to four meters of thrust motion is estimated on the Susitna Glacier fault. The total moment release of the preferred model is  $5.8 \times 10^{20} \text{ Nm}$  ( $M_W$



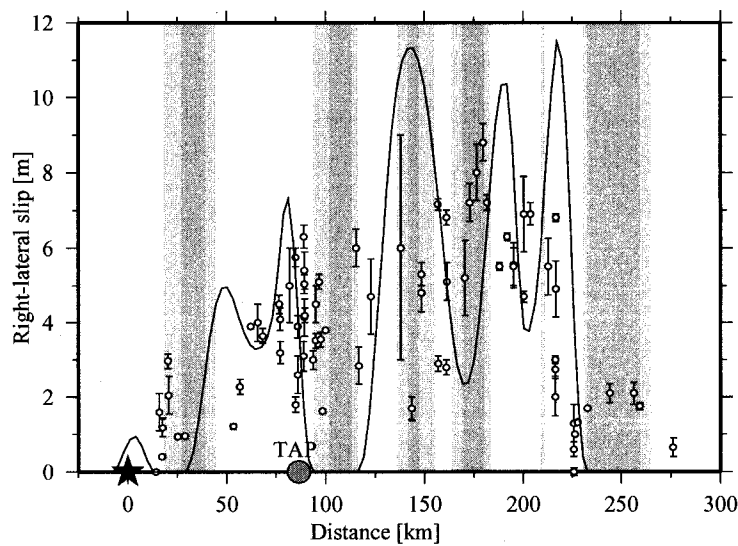


Figure 3.6. Estimated right lateral surface offset of the preferred model (line) compared to geological surface measurements from *Eberhart-Phillips et al.*, [2003]. By inverting synthetic data of uniform slip we identified areas of poor model resolution along the surface, with dark gray areas showing < 50 % resolved and light gray < 70 %.

7.8), slightly lower than estimated from teleseismic data [*Eberhart-Phillips et al.*, 2003].

The modeled surface slip shows a similar pattern to the measured surface offsets, varying from little to no dextral offset in the epicentral region to about 10 m of slip just west of the Denali-Totschunda fault junction (Figure 3.6). The surface slip observations were not used in the inversion, so they provide an independent test of the model. Although there are slight offsets between the locations of peak slip in the two data sets, the overall agreement is good. The average 2 m of thrust motion on the Susitna Glacier fault, corresponding to an  $M_W$  7.0 subevent, is also consistent with surface observations but has a slightly lower seismic moment than estimated from teleseismic data [*Eberhart-Phillips et al.*, 2003].

Surface measurements resolve dextral offsets of up to 2 m along the Totschunda fault but in the preferred model very little slip is found on the fault. The Totschunda fault is not well covered by the coseismic GPS data and tests with inverting synthetic data of uniform slip at given depth indicate that model resolution for shallow slip on the fault is very poor. Resolution for slip from 6-12 km depth is good, so the lack of slip in the model may indicate that coseismic slip on the Totschunda fault was shallow.

No slip is estimated west of the epicenter where the  $M_W$  6.7 earthquake ruptured the

Denali fault prior to the  $M_W$  7.9 earthquake. Tests with synthetic data show that this part of the model is well resolved, so the lack of model slip shows that the  $M_W$  7.9 earthquake did not re-rupture the  $M_W$  6.7 rupture zone. Very little slip is found on the Denali fault near the hypocenter, although model resolution here is not as good as to the west. About 2-4 m of deep slip is found below the thrust fault which might indicate rupture of both faults, or might be the result of a trade off between slip on the Susitna Glacier fault and the Denali fault.

In general, slip on the fault extends from the surface to 10-15 km depth. However, the model has a patch of very deep slip just east of the pipeline crossing, corresponding to an  $M_W$  7.4 subevent. All relocated aftershocks are less than 10 km deep and do not give any indication of deep slip [Ratchkovski *et al.*, 2003]. We have done several tests, removing stations from the inversion, adding potential splay faults to the model, and allowing dip slip motion along the fault, but we find a similar deep slip patch in all inversions. These tests indicate that this result is probably real and reflects some local complication. The deep slip is found in a complex area where there are many splay faults both north and south of the Denali fault [Plafker *et al.*, 1994]. Aftershocks are spread over a broad area and the largest aftershock of the Denali fault earthquake,  $M$  5.8 on 3 November, occurred in this region (no focal mechanism is available for this aftershock, as it occurred within the coda of the  $M_W$  7.9 event) [Ratchkovski *et al.*, 2003].

The GPS coseismic displacements from the  $M_W$  7.9 earthquake agree with right lateral strike slip motion along the Denali and Totschunda faults and thrust motion on the Susitna Glacier fault. The earthquake did not re-rupture the  $M_W$  6.7 rupture zone. Variations in coseismic slip along the fault and with depth reflect the complex nature of the earthquake. Our results are in good agreement to surface offsets and seismic measurements.

### 3.6 Acknowledgments

Data from the Yukon were provided by P. Flück and M. Schmidt at the Geological Survey of Canada. We are grateful to E. Calais, J. Elliot, J. Greenberg, L. Hennig, M. Jadamec, B. Johns, J. Kalbas, B. MacCormack, D. Moudry, E. Price, K. Ridgway, F. Rolandone, N. Rozell, J. Sklar, J. Stachnik, D. Templeton, and T. Tin for fieldwork assistance. We thank N. Ratchkovski for discussions on aftershock locations. The manuscript benefited from

helpful reviews and suggestions from N. King and an anonymous reviewer. This research was supported by NSF grant EAR-0328043 to J. Freymueller and R. Hansen, by the Alaska Earthquake Information Center, and by the UAF Geophysical Institute.

## References

- Boucher, C., Z. Altamimi, and P. Sillard (1999), The 1997 International Terrestrial Reference Frame (ITRF97), *IERS Tech. Note 27*, Int. Earth Rotation Serv., Paris.
- Eberhart-Phillips D., P. J. Haeussler, J. T. Freymueller, + 23 coauthors (2003), The 2002 Denali fault earthquake, Alaska: A large magnitude, slip-partitioned event, *Science*, 1113-1118, 2003.
- Fletcher, H. J., Tectonics of interior Alaska from GPS measurements (2002), Ph.D. thesis, 257 pp., Univ. Alaska Fairbanks, Fairbanks, Alaska.
- Freymueller, J. T, S. C. Cohen, and H. J. Fletcher (2000), Spatial variations in present-day deformation, Kenai Peninsula, Alaska, and their implications, *J. Geophys. Res.*, 105(B4), 8079-8102.
- Freymueller, J. T., N. E. King, and P. Segall (1994), The co-seismic slip distribution of the Landers earthquake, *Bull. Seis. Soc. Amer.*, 84(3), 649-659.
- Kikuchi, M., and Y. Yamanaka (2002), Source rupture processes of the central Alaska earthquake of Nov. 3, 2002, inferred from teleseismic body waves (+ the 10/23 M6.7 event), EIC seismological note - No. 129, Earthquake Research Institute (ERI), Univ. Tokyo, Tokyo.
- Matthews, M, and P. Segall (1993), Statistical inversion of crustal deformation data and estimation of the depth distribution of slip in the 1906 earthquake, *J. Geophys. Res.*, 98(B7), 12153-12163.
- Okada, Y. (1985), Surface deformation due to shear and tensile faults in a halfspace, *Bull. Seis. Soc. Amer.*, 75(4), 1135-1154.
- Plafker, G, L. Gilpin, and J. Lahr (1994), Neotectonic map of Alaska, Map in *The Geology of North America, Decade of North American Geology*, vol. G-1, edited by G. Plafker and H. C. Berg, Geol. Soc. Amer., Boulder, Colorado.
- Ratchkovski, N. A., R. A. Hansen, and J. C. Stachnik (2003), The 7.9 Denali fault earthquake of November 3, 2002: Aftershock locations, moment tensors, and focal mechanisms

from the regional and temporary seismic network data, *Seis. Res. Lett.*, 74(2), SSA 2003 Annual Meeting, 236.

Stark, P. B., and R. L. Parker (1995), Bounded-variable least-squares: An algorithm and application, *Comput. Stat.*, 10(2), 129-141.

Zweck, C., J. T. Freymueller, S. C. Cohen (2002), Three-dimensional elastic dislocation modeling of the postseismic response to the 1964 Alaska earthquake, *J. Geophys. Res.*, 107(B4), doi:10.1029/2001JB000409.

## Chapter 4

### Coseismic Deformation of the 2002 Denali Fault Earthquake: Insights from GPS Measurements<sup>3</sup>

#### 4.1 Abstract

We estimate coseismic displacements from the 2002  $M_W$  7.9 Denali Fault earthquake at 232 GPS sites in Alaska and Canada. Displacements along a N-S profile indicate right-lateral slip on a near vertical fault with a significant component of vertical motion, north-side up. We invert both GPS displacements and geologic surface offsets for slip on a 3D fault model in an elastic half-space. We restrict the motion to right-lateral slip and north-side up dip-slip. Allowing for oblique slip along the Denali and Totschunda faults improves the model fit to the GPS data by about 30%. We see mostly right-lateral strike-slip motion on the Denali and Totschunda faults but in a few areas we see a significant component of dip-slip. The slip model shows increasing slip from west to east along the Denali fault, with four localized higher-slip patches, three near the Trans-Alaska pipeline crossing and a large slip patch corresponding to a  $M_W$  7.5 subevent about 40 km west of the Denali-Totschunda junction. Slip of 1-3 m was estimated along the Totschunda fault with the majority of slip being at shallower than 9 km depth. We have limited resolution on the Susitna Glacier fault but the estimated slip along the fault is consistent with a  $M_W$  7.2 thrust-sub-event. Total estimated moment in the Denali Fault earthquake is equivalent to  $M_W$  7.89. The estimated slip distribution along the surface is in very good agreement with geological surface offsets but we find that surface offsets measured on glaciers are biased toward lower values.

#### 4.2 Introduction

On November 3rd 2002, the  $M_W$  7.9 Denali Fault earthquake ruptured about 340 km along three faults in the interior of Alaska [Eberhart-Phillips *et al.*, 2003; Haeussler *et al.*, 2004] (Figure 4.1). The earthquake initiated with thrust motion on the Susitna Glacier fault, but continued along the Denali and then the Totschunda fault with right-lateral strike-slip motion, rupturing unilaterally from west to east. Ten days earlier an  $M_W$  6.7 right-lateral strike-slip earthquake, the Nenana Mt. earthquake, occurred on the Denali fault with an

---

<sup>3</sup>Submitted to *Journal of Geophysical Research*, February 2005, under the same title with authors S. Hreinsdóttir, J. T. Freymueller, R. Bürgmann, and J. Mitchell.

epicenter only 22 km west of the Denali Fault earthquake epicenter [Eberhart-Phillips *et al.*, 2003].

The Denali fault is part of a system of active intra-continental faults in North America that accommodate deformation associated with the transition of the North American-Pacific plate boundary from transcurrent (Queen Charlotte-Fairweather transform-fault system) to convergent (Aleutian megathrust) (Figure 4.1). The transition is complicated by the Yakutat terrane, located in the junction and currently colliding with the North American plate, causing extremely active and complex deformation [Page *et al.*, 1991; Plafker and Berg, 1994; Fletcher and Freymueller, 2003].

Prior to the 2002 earthquake sequence, the level of recorded seismicity along the Denali fault was very low. The seismic behavior of the Denali fault seems to be characterized by infrequent large earthquakes with quiet periods in between [Ratchkovski *et al.*, 2003]. Paleoseismologic data from a test pit close to where the Trans-Alaska pipeline (TAP) crosses the Denali fault show two earlier events probably of comparable size to the Denali Fault earthquake, suggesting a recurrence interval of 350-400 yr [Plafker *et al.*, 2004]. In 1912 an M7.2 earthquake occurred in the region (between -144.5 to -149.5° E) and possibly ruptured the Denali fault [Doser, 2004]. Available phase and waveform information for the earthquake are consistent with, but not limited to, a shallow source depth and right-lateral earthquake rupture [Doser, 2004]. Studies of trees damaged in the Denali Fault earthquake around the Trans-Alaska pipeline crossing reveal damage related to an earlier earthquake, with tree ring counts dating back to around 1912 [Plafker *et al.*, 2004]. Several large (>M4.5) earthquakes occurred in the interior of Alaska in the 80 years prior to the Denali Fault earthquake but on adjacent strike-slip faults and thrust faults north and south of the main Denali fault trace that appear to play an important role in the regional deformation [Doser, 2004].

Plafker *et al.* [1994] estimated a rate of 8-12 mm/yr of right-lateral slip along the Denali fault during the Holocene, and paleoseismic data from two major events in the last millennium indicate an average long term slip rate possibly as high as 15 mm/yr [Plafker *et al.*, 2004]. Terrestrial geodetic measurements conducted in the 1970s and 1980s indicated a low slip rate on the fault, indistinguishable from zero, but with an uncertainty of several mm/yr [Page and Lahr, 1971; Page, 1972; Savage and Lisowski, 1991]. GPS geodetic measurements in the period 1995 to 2002 suggest slip rates of 6-9 mm/yr on the Denali

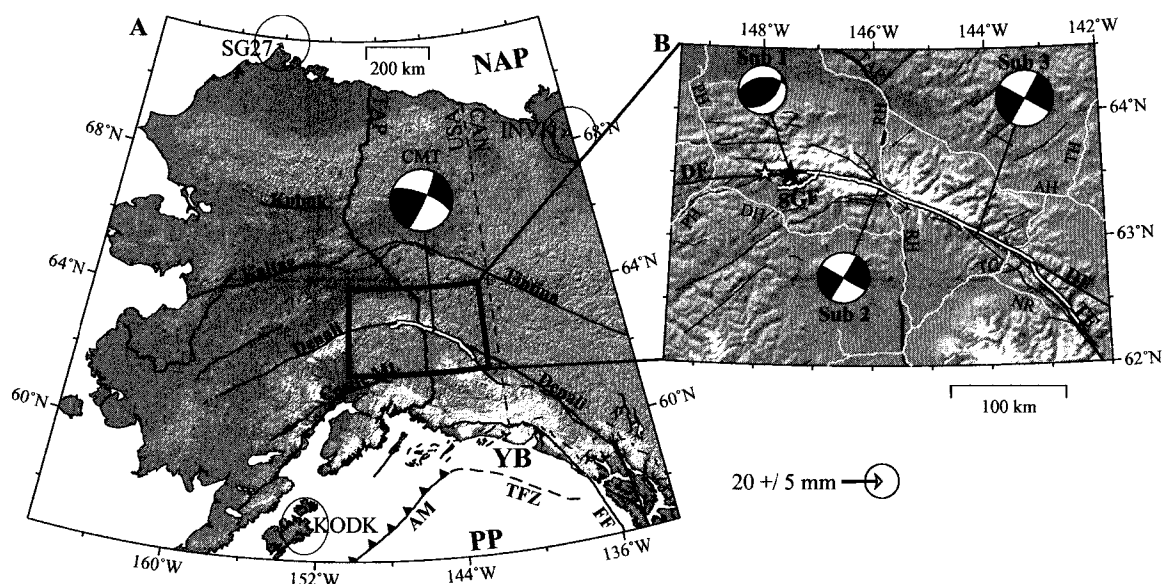


Figure 4.1. Tectonic setting of the Denali Fault earthquake. A) Major tectonic boundaries between the North American plate (NAP), the Pacific plate (PP), and the Yakutat block (YB). The Alaska megathrust (AM) and the Fairweather fault (FF), take up the majority of the deformation between the plates but a small fraction of the relative plate motion is distributed on other major faults (black lines), both offshore (e.g. the Transition fault zone (TFZ)) and in the interior of Alaska (USA) and the Yukon (CAN). The white line indicates the Denali Fault earthquake rupture [Haeussler *et al.*, 2004] and the focal mechanism is the Harvard CMT solution for the earthquake. Far-field GPS sites INVK, SG27, and KODK, did not have a significant coseismic displacement in the earthquake (shown with 95% confidence ellipse; scale to lower right). B) The Denali Fault earthquake ruptured 3 major faults, the Susitna Glacier (SGF), Denali (DF) and Totschunda faults (TF). The dark star shows the epicenter of the Denali Fault earthquake and the smaller open star shows the epicenter of the  $M_W$  6.7 Nenana Mt. earthquake [Ratchkovski *et al.*, 2004]. The focal mechanisms shown are for the first motion solution (sub1) and the two largest subevents from waveform inversion (sub2 and sub3) [Eberhart-Phillips *et al.*, 2003]. The Trans-Alaska pipeline (TAP) and roads parallel to and crossing the fault are shown for reference: Parks Hwy (PH), Denali Hwy (DH), Richardson Hwy (RH), Alaska Hwy (AH), Tok Cutoff (TC), Nabesna Rd (NR), and Taylor Hwy (TH). Faults taken from *Plafker et al.* [1994].

fault [Fletcher, 2002].

The Denali Fault earthquake initiated with an  $M_W$  7.2 thrust event rupturing about 48 km of the surface along the Susitna Glacier fault, with an average dip-slip of 4 m [Eberhart-Phillips et al., 2003; Crone et al., 2004]. The earthquake then ruptured along 226 km of the Denali fault with increasing right-lateral offset from west to east, reaching a maximum surface offset of 8.8 m about 40 km west of the Denali-Totschunda fault junction. Strong motion inversions suggest two main strike-slip subevents along the Denali fault following the initial thrust event (Figure 4.1) [Eberhart-Phillips et al., 2003]. The second subevent ( $\sim M_W$  7.3) occurred about 90 km east of the epicenter, around where the Trans-Alaska pipeline crosses the fault. The third and largest subevent,  $M_W$  7.6, occurred in the region where the maximum surface offset was measured, about 40 km west of the Denali-Totschunda fault junction. The aftershock distribution shows several persistent clusters and aseismic patches along the fault, with the majority of events occurring at shallower than 11 km depth [Ratchkovski et al., 2004]. The aftershock seismicity is in general rather diffuse and does not clearly align with the rupture trace. About 230 km east of the epicenter both aftershocks and the surface rupture abandon the Denali fault and jump over to the Totschunda fault, on which the earthquake ruptured another 66 km [Haeussler et al., 2004; Ratchkovski et al., 2004]. Relatively low surface offsets, less than 2 m on average, were measured along the Totschunda fault.

The Denali Fault earthquake is one of the largest strike-slip earthquakes in recorded history and provides an opportunity to study such an earthquake with modern technology. Hreinsdóttir et al. [2003] previously presented a coseismic slip model using GPS displacements at 40 sites measured in the week following the earthquake. Wright et al. [2004] used the same GPS data in addition to InSAR data from the epicentral region to estimate the slip distribution. Source processes of the earthquake have also been studied using teleseismic [e.g. Ji et al. 2004; Kikuchi and Yamanaka, 2002; Ozacar et al., 2003; Ozacar and Beck, 2004] and strong motion data [e.g. Frankel, 2004; Dreger et al., 2004; Oglesby et al., 2004].

An accurate coseismic slip model is needed both for studies of earthquake ruptures and for driving models of postseismic deformation. InSAR data are limited to roughly the western third of the rupture, and do not constrain the section of the fault that experienced the greatest slip during the earthquake [Wright et al., 2004]. A limited number of high



precision GPS measurements had been made in the interior of Alaska prior to the earthquake with the aim of studying regional deformation, but the distribution of available sites was not ideal [Fletcher, 2002; Hreinsdóttir et al., 2003]. Due to the popular use of GPS in surveying, a large amount of additional GPS data existed from highway survey markers prior to the earthquake. Although the earthquake rupture was remote, several highways lie conveniently parallel and perpendicular to the fault (Figure 4.1). We devoted an extensive effort to gathering the most complete GPS displacement data set possible for this earthquake.

Here we present new and updated coseismic displacements for the  $M_W$  7.9 Denali Fault earthquake at GPS sites in Alaska and Canada. We correct the displacements, as necessary, for interseismic and postseismic displacements. We use the GPS data and geological surface offset measurements to estimate a realistic slip distribution for the earthquake. We then compare the preferred model to surface offset data and seismological observations.

### 4.3 GPS Data and Analysis

We estimate coseismic displacements from the 2002 Denali Fault earthquake for 232 sites in Alaska and Canada, of which 180 campaign sites and 12 permanent stations are within one rupture length ( $\sim 350$  km) of the earthquake rupture (Figure 4.2). Three of these sites were measured using only EDM and theodolite prior to the earthquake, but all other sites were measured using dual frequency GPS receivers both before and after the earthquake. We also estimate coseismic displacements for the Nenana Mt. earthquake at 14 GPS sites and use the measurements to estimate and remove its effect on other sites not measured between the two earthquakes (Figure 4.3). The geodetic survey markers and permanent GPS stations used in this study are listed along with their measurement history in Table B.1.

Coseismic displacements for 40 sites measured within the first week of the earthquake were previously presented by Hreinsdóttir et al. [2003]. We have re-analyzed the data and re-evaluated the displacements, here presenting updated coseismic displacements for these sites. This analysis has resulted in more than 1 cm change in the horizontal displacement at 5 sites. Four of these changes result from improved interseismic corrections (0999, 2999, MEN and 7297), and one is a result of using a later and more reliable post-earthquake survey (TURN). In addition we fixed a reference frame error on the order of few mm affecting sites

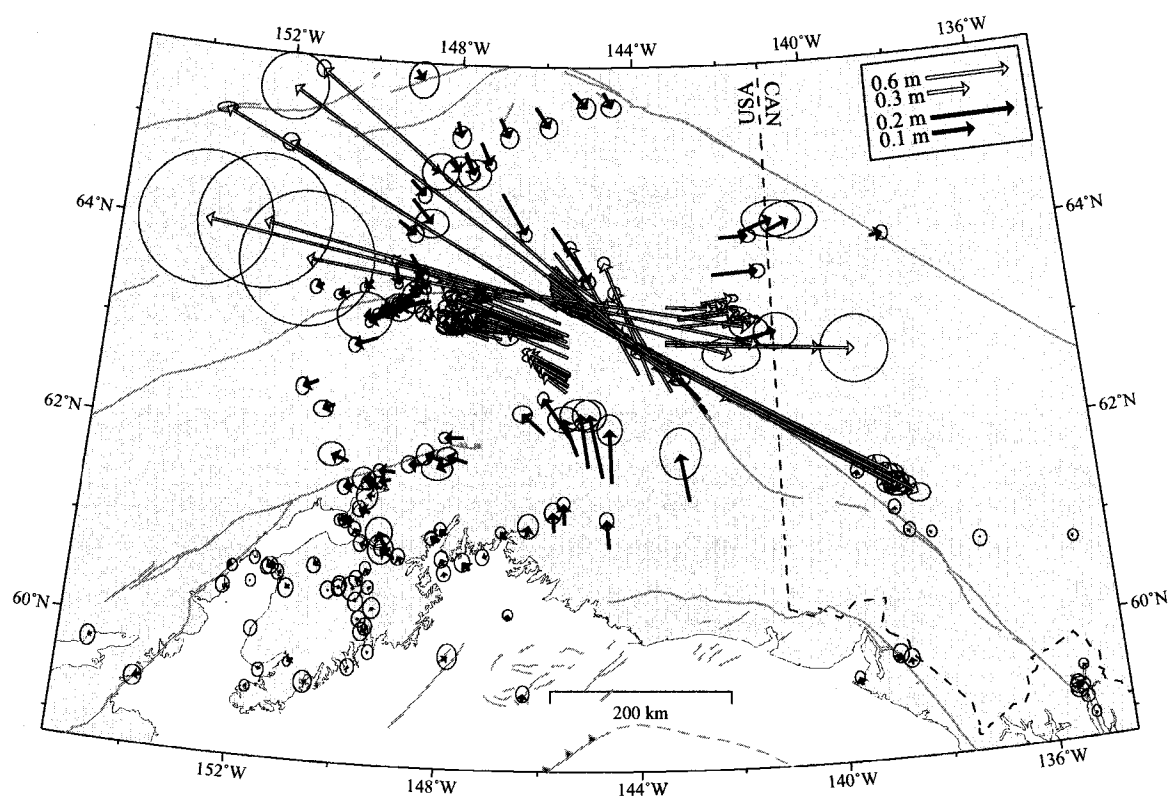


Figure 4.2. Horizontal coseismic displacements from the  $M_w$  7.9 Denali Fault earthquake. For clarity we divided the displacement by magnitude,  $> 0.2$  m (yellow vectors) and  $\leq 0.2$  m (blue vectors) and show at two different scales (1:3). Displacements for ORTT, FM11 and FM12 are not shown here (see Figure 4.4) as their displacements are strongly influenced by local effects. The red star shows the earthquake's epicenter and the red line indicates the earthquake's surface rupture [Eberhart-Phillips *et al.*, 2003].

that were not measured in the few weeks before the earthquake.

#### 4.3.1 Pre-Earthquake Survey Data

The pre-earthquake GPS data come from multiple sources and date as far back as 1990. We only used data from sites that were measured for at least one hour with a dual frequency receiver. The GPS data can be divided into two categories:

1. GPS geodetic measurements of 8+ hr per day, usually for multiple days, with the aim of achieving mm level accuracy.
2. GPS surveys of 1+ hr with the aim of achieving cm level accuracy.

About 40% of the sites had been measured repeatedly in multiple years with category 1 accuracy, allowing us to estimate their pre-earthquake velocities. Another 40% had only been measured with category 2 accuracy. The remaining sites had high accuracy pre-earthquake surveys, but their measurement history was too short to estimate a precise pre-earthquake velocity.

Unfortunately most of the earliest data (1990-1991) turned out to be problematic due to poor data quality from very old equipment, and we could only use data from three of these sites. In addition we only used data from far-field sites that either had a good pre-earthquake time series or were measured just before and just after the earthquake, thus excluding sites where uncertainties in the interseismic correction may outweigh the coseismic signal.

The main sources of pre-earthquake data were:

1. University of Alaska Fairbanks (UAF) geodesy lab: Multiple 8-24 hr geodetic measurements of sites from 1995 to 2002. Trimble receivers.
2. NASA Goddard Space Flight Center (NASA): Multiple 8-24 hr geodetic measurements of sites in 1993, 1995, and 1997. Turborogue and Trimble receivers.
3. USGS: Multiple 8-24 hr geodetic measurements of sites in 1993, 1995, 1997 and 2000. Turborogue (1993, 1995) and Ashtech (1997, 2000) receivers.

4. NOAA Pacific Photogrammetric Party for the National Geodetic Survey (NOAA): Multiple  $\sim$  8 hr geodetic measurements of sites in 1992, 1993, 1995 and 1996. Trimble receivers.
5. Geological Survey of Canada, Pacific Geoscience Center (GSC/PGC): Multiple 8-24 hr geodetic measurements 1999 to 2002. Ashtech receivers.
6. Aeromap USA, Anchorage (AERO): 8+ hr surveys of sites in 2002. Trimble receivers.
7. University of Alaska Fairbanks (UAF), glaciology lab: 1+ hr surveys in 1993 and 2002. Trimble receivers.
8. Crazy Mountains Joint Venture Anchorage (CMJV): 1+ hr surveys of sites in 1990, 1991, 1994, and 2002. Ashtech (1990-1994) and Javad Legacy (2002) receivers.
9. Alaska Department of Transportation (ADOT): 1+ hr surveys of sites in 1994, 1999, 2001, and 2002. Leica receivers.
10. OceanTech, Anchorage, for Alyeska Pipeline Service Company: 1+ hr surveys of sites in 1994. Ashtech receivers.

In addition to the pre-earthquake GPS data we used geodetic measurements from five sites around the upper Black Rapids glacier. These sites are part of a geodetic network surveyed using EDM and theodolite. For these sites we estimated horizontal displacements by comparing GPS surveys to the 1970s terrestrial survey measurements.

#### **4.3.2 Post Nenana Mt. Earthquake Data**

Following the  $M_W$  6.7 Nenana Mt. earthquake, 23rd October 2002, 13 GPS sites around the epicenter were measured (UAF, Trimble receivers). In addition we have one permanent site, GRNR, within 100 km of the epicenter. All but one site (B124) had several years of pre-earthquake measurements and six of the sites (including B124) were measured in the four months prior to the earthquake.

### 4.3.3 Post Denali Fault Earthquake Data

The Denali Fault earthquake occurred during the winter of 2002. Due to snow cover and harsh weather conditions we had a limited time window to conduct fieldwork following the earthquake. In the immediate response to the earthquake, 32 sites in Alaska (UAF and UC Berkeley, Trimble receivers) and 6 in Canada (GSC/PGC, Ashtech receivers) were measured, all but one by mid-November 2002 [Hreinsdóttir *et al.*, 2003]. In addition, Aeromap was surveying sites in Southeast Alaska at the time of the earthquake and measured 6 sites before, during, and after the earthquake (Trimble receivers). An additional 4 sites were measured in south central Alaska by the end of November (USGS, Trimble receivers, and ADOT, Leica receiver).

From May to November 2003 we measured about 200 additional pre-existing GPS sites (Trimble receivers). We divided the sites into *long* and *short* survey sites depending on the quality of the pre-earthquake data and the security level of the sites. Short survey sites were measured for a minimum of 2 hours but long survey sites were measured for at least two 8+ hour surveys, and typically multiple 24 hour surveys. Most of the sites were measured during two GPS campaigns, spring (May-June) and fall (Oct-Nov) in cooperation between UAF, UC Berkeley and Purdue. Other sites were measured during various UAF GPS campaigns in Alaska. Additional post-earthquake data were provided by the USGS (Ashtech receivers).

The search for pre-earthquake data and GPS sites around the Denali fault still continues and additional sites were measured in 2004. Due to difficulties with postseismic correction we only include data from one site here (MAT) that was not found until May 2004, but which is important for resolving slip at the Totschunda-Denali fault junction.

### 4.3.4 GPS Data Analysis

We analyzed the GPS data from 1992 to 2004 using the GIPSY/OASIS II software (release 6) developed at the Jet Propulsion Laboratory (JPL). Data from each day were analyzed separately to obtain reference frame-free daily network solutions. For data from 1992 to 1994 we estimated loosely constrained orbits using global solutions with reference clock ALGO. All available global GPS sites were used. A set of 13 to 37 global reference sites (a

generally increasing number with time but also variable from day to day based on availability) was used to define a 7 parameter Helmert transformation for the daily solutions to the International Terrestrial Reference Frame 1997 (ITRF97) [Boucher *et al.*, 1999]. For data from 1995-2004 we fixed the JPL non-fiducial orbits in the analysis. The daily GPS solutions were then transformed into ITRF97 using 7-18 reference sites surrounding Alaska (again variable day to day based on availability) to define the 7 parameter Helmert transformation. More details on the analysis strategy are given in Freymueller *et al.* [2000].

The 1990-1991 positions were derived from baseline vector solutions using Ashtech GPPS differential GPS processing software. Most of the data were collected using Ashtech L-XII receivers, which were quite noisy and had unreliable L2 tracking. These data were generally acquired in baseline mode by two receivers with the network constructed by stepwise addition of baseline vectors. The baseline vectors (dX, dY, dZ) were added to estimated ITRF positions for well documented control stations (SOUR, STRI, FAIR) to produce the final coordinates. The survey accuracy for these baselines is of the order of 1-5 ppm. As a result, it was only possible to add a few baseline vectors to the more precise control stations before survey errors became unacceptably large.

#### 4.3.5 Black Rapids Glacier Geodetic Network

The Black Rapids glacier in the Alaska Range follows the Denali fault for about 30 km. In 1973, a geodetic network was installed and measured along the glacier as a reference network for monitoring and studying glacier surges. The network was measured using theodolite and electronic distance measuring equipment and site coordinates were reported in a local coordinate system, approximately aligned with UTM zone 6 [Heinrichs, 1994; Heinrichs *et al.*, 1995]. In 1993 two sites in the network, BRLA and BRWE, were measured with GPS. We use these GPS data to more rigorously tie the local system to UTM.

The 1993 GPS data from BRWE and BRLA were processed in our standard solutions giving coordinates in ITRF97. The coordinates were transformed into UTM zone 6 using GMT's mapproject utility [Wessel and Smith, 1998]. Using conversions estimated by Heinrichs [1994] from their NAD83-based analysis of the GPS data, the coordinates of BRWE

and BRLA were converted from UTM to the local coordinate system:

$$UTMEasting = 0.999618X + 516,000 \quad (4.1)$$

$$UTMNorthing = 0.999618Y + 7,026,000 \quad (4.2)$$

Assuming that the local coordinate system is internally consistent we use these GPS derived coordinates to tie the local coordinate system to UTM, estimating rotation ( $\theta$ ), translation ( $c$  and  $d$ ), and scaling ( $s$ ) from the local coordinate system ( $X', Y'$ ) to the GPS-tied coordinate system ( $X, Y$ ):

$$X = s(X' \cos \theta - Y' \sin \theta) + c \quad (4.3)$$

$$Y = s(X' \sin \theta + Y' \cos \theta) + d \quad (4.4)$$

The estimated transformation, scaling of  $s = 0.99996833$ , rotation of  $\theta = -0.0387^\circ$  and translation  $c = -129.6585$  m and  $d = 179.0492$  m was used to transform the local network coordinates of *Heinrichs* [1994] to the GPS corrected local coordinates. We then transformed the local coordinates to UTM and estimated Easting and Northing relative to BRWE. We estimated east and north displacements from the UTM coordinates and post-earthquake GPS coordinates transformed to UTM.

In the period between the 1973 geodetic measurements and the 1993 GPS measurements 20 years of interseismic deformation probably distort the network only slightly. Fortunately both the sites measured with GPS in 1993 are on the north-side of the fault, and both are relatively close to the fault ( $< 2$  km). Given the 6-9 mm/yr slip rate of the Denali fault [Fletcher, 2002], we can assume that they did not move significantly relative to each other in the 20 year time period between the measurements. A simple screw dislocation model using 7 mm/yr and a 12 km locking depth [Fletcher, 2002] gives less than 5 mm of relative motion between these sites over 20 years, and the reported coordinates are given with precision of 1 cm.

#### 4.3.6 Estimating Coseismic Displacements

Of the 232 GPS sites for which we estimate coseismic displacement, 37 were measured just before and after the earthquake (19 were continuous stations). For other sites interseismic

deformation must be corrected for. Many of the sites had been measured multiple times over period of years prior to the earthquake allowing us to estimate interseismic velocity at the sites. Unfortunately this is true for less than half of the stations. For other sites we had to estimate the interseismic correction based on velocities at neighboring sites. In order to minimize possible errors from erroneous interseismic corrections, we only used data from sites that had predetermined interseismic velocities based on their own time series (90 sites), data from sites that were measured just before and after the earthquake (37 sites), and data from sites where we expect a low interseismic rate (based on surrounding sites) and/or large coseismic displacements compared to the interseismic correction (105 sites). This eliminated some potential far-field sites from the southern coast of Alaska, where the interseismic correction would have been of the same order as the coseismic displacement or larger. Fortunately, the interior of Alaska and the Yukon has fairly low interseismic rates [Fletcher, 2002], so all of the data near the fault and north of it were usable.

For all sites first measured more than two weeks after the earthquake, a postseismic correction was estimated based on a simple model fit to postseismic displacements, and applied to correct the displacement estimates.

We used four different methods to estimate displacements due to the earthquake, depending on the temporal distribution of data.

- 1) For permanent sites and sites measured in the week prior to and in the two weeks following the earthquake we merged together the last four pre-earthquake solutions and the first four post-earthquake solutions containing the site. We scaled the uncertainty by the scatter in the solutions and estimated displacements from the pre-earthquake and post-earthquake solutions. For these sites interseismic corrections were not required.

- 2) For sites that had multiple years of pre-earthquake data, but were not measured in the week prior to the earthquake, we used all available pre-earthquake solutions from 1992 to 2002 to estimate a site location at the time of the first post-earthquake measurement assuming linear motion with time. For the post-earthquake location we merged together the first four days of post-earthquake measurements, scaling the uncertainties by the scatter in the network solution. We then estimated the coseismic displacement by subtracting the pre-earthquake estimate from the merged post-earthquake solution.

- 3) For sites that had less than a year span of pre-earthquake measurements, therefore not



allowing us to estimate a precise velocity at the site, we estimated the displacements using the last pre-earthquake data and first post-earthquake data, correcting for the interseismic deformation using an estimate based on the interseismic velocities measured at surrounding sites.

4) For sites for which pre-earthquake data were measured prior to 1992 we estimated baseline changes relative to a nearby site measured at the same time but for which we have later and more reliable GPS measurements. For sites in the Black Rapids Glacier geodetic network, measured in 1973 with EDM, the post earthquake GPS data were first transformed from ITRF97 to UTM where coseismic changes were estimated in Easting and Northing. At sites where coseismic displacement was estimated in baseline mode, we used a simple screw dislocation model to estimate an interseismic correction for the Denali Fault using a locking depth of  $12 \pm 2$  km and slip rate of  $7 \pm 1$  mm/yr [Fletcher, 2002].

### **Interseismic Correction**

For sites with less than a year span of pre-earthquake measurements we estimated interseismic corrections by interpolating between sites with available interseismic rate estimates. The largest gap between sites over which we interpolated was just over 120 km for two sites north of the fault. We ran into a problem when trying to interpolate interseismic velocities for sites in two areas close to the Denali fault; for three sites north of the Black Rapids glacier, and 3 sites south of the fault, on the Nabesna Rd. We did not want to interpolate across the fault and we had a limited number of sites with known velocities in the area. We estimated interseismic rates at these sites assuming a tectonic model of Southern Alaska block rotation [Fletcher, 2002], using the strike of the fault and the interseismic rate of sites on the same side and at a similar distance to the fault. Interseismic corrections for these sites are less than 5% of the measured displacements. The interseismic corrections are given in Table B.3.

### **Postseismic Correction**

Postseismic deformation is variable in space and time and must be removed from all sites not surveyed immediately after the earthquake. It is the fastest right after an earthquake and probably a result of more than one mechanism; e.g. afterslip, poroelastic relaxation,

and viscoelastic relaxation, all potentially decaying at different time scales and affecting regions differently.

In order to study postseismic deformation after the Denali Fault earthquake many new sites along with coseismic sites were surveyed and 11 continuous GPS stations were installed around the fault in the first two weeks after the earthquake. In spring and fall 2003 all these sites were re-surveyed to estimate postseismic displacements for each period. A number of additional sites were measured in the spring of 2003 and again in the fall. We use the observed postseismic displacements at these sites to construct an empirical correction for nearby sites that need a postseismic correction. There was certainly some postseismic deformation in the first 1-2 weeks after the earthquake but we lack the data to remove this component from the coseismic displacement field, so early postseismic motion is included in the coseismic estimate.

We chose to use a simple geophysical model as a means of interpolating and extrapolating measured postseismic displacements. We estimated an afterslip model using available postseismic data for both time periods. We used the model to estimate postseismic corrections for coseismic sites first measured in 2003. Although it is unlikely that afterslip is the only active postseismic mechanism, this model provides a sensible interpolation of the observed postseismic displacements at nearby coseismic observation points in most areas. In two regions the afterslip model could not explain the postseismic displacements, giving systematic misfits of more than 10%. For these regions, the Taylor Hwy, NE of the rupture, and Denali Hwy, south of the western rupture, we used direct interpolation between sites with postseismic measurements. The same was done for the site MAT on Nabesna Rd, not measured until May 2004, The postseismic corrections applied to the data are given in Table B.3.

#### **4.3.7 Nenana Mt. Earthquake**

Ten days prior to the Denali Fault earthquake, on 23rd October 2002, the  $M_W$  6.7 Nenana Mt. earthquake ruptured the Denali fault, with an epicenter only 22 km west of the Denali Fault earthquake epicenter (Figure 4.3). No surface rupture was observed after the earthquake [Eberhart-Phillips *et al.*, 2003]. Aftershocks occurring within an hour of the earthquake indicate that the earthquake ruptured about 30 km of the Denali fault towards

the west from the epicenter. Relocated aftershocks show that the majority of the aftershocks occurred between 3 to 12 km depth, forming a vertical plane beneath the surface trace [Ratchkovski *et al.*, 2003].

We estimated coseismic displacements from the Nenana Mt. earthquake for 14 available GPS sites, all within 50 km of the main aftershock region (Figure 4.3, Table B.2). All but two of the GPS sites are west of the aftershock region, with most along the Parks Hwy which lies perpendicular to and crosses the fault west of the epicenter (Figure 4.3). The GPS data generally show displacements toward the epicenter at sites north of the Denali fault and away from the epicenter at sites south of the fault, as we would expect from a right-lateral strike-slip earthquake. The maximum observed displacement was just over 4 cm (GRIZ).

*Wright et al.* [2003] inverted InSAR data from the Nenana Mt. earthquake and estimated a best fitting single dislocation model of a near-vertical dislocation ( $21.5 \pm 1.0$  km long and  $15.4 \pm 1.3$  km wide plane, dipping  $81.2 \pm 1.7^\circ$  north), with 1 m of slightly oblique right-lateral strike-slip (north-side up). The model shows general agreement with GPS observations but the misfit is well above the level expected from measurement errors alone (Figure 4.3). Using their model as a starting point and varying the horizontal location of the fault but keeping all other fault parameters fixed we found a significantly improved fit to the GPS data (Figure 4.3). Our estimated fault location differs by 2.8 km from theirs which cannot be explained by reference frame errors or model location error alone. We excluded the site DH97 when finding the best model. It is located directly south of the epicenter and shows northward displacement but its uncertainty is relatively high. The aftershock distribution indicates that the fault ruptured towards the west from the epicenter so we expected a displacement toward NW at this site. This apparent bias is presently unexplained; the site had a well-determined pre-earthquake velocity from 1997 to 2000 and a good post-Nenana Mt. earthquake survey, and the survey mark is in a stable bedrock setting.

We used this slightly modified *Wright et al.* model to correct for coseismic displacements of the Nenana Mt. earthquake at sites in the region not measured between the Nenana Mt. and Denali Fault earthquakes (Table B.3). Four sites required correction ranging from 28 to 38 mm but all other sites had less than 20 mm correction.

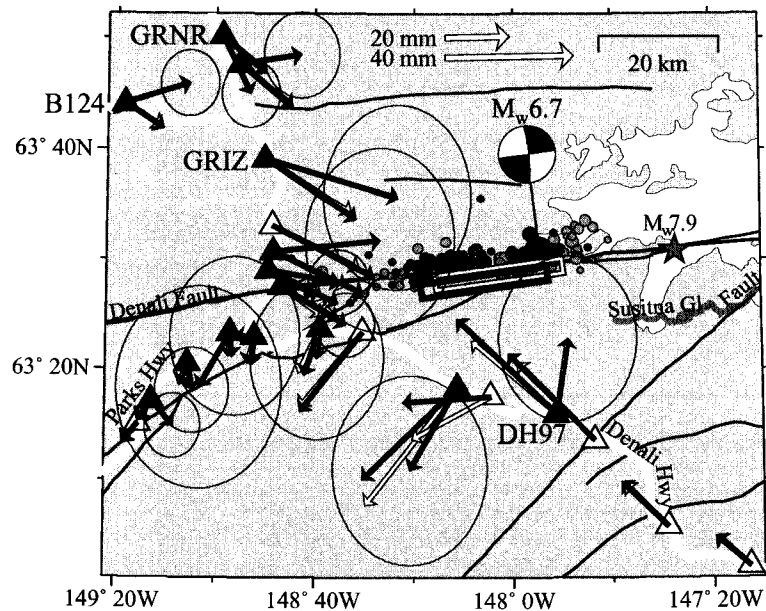


Figure 4.3. The  $M_W$  6.7 Nenana Mt. earthquake setting. Black triangles show sites for which we have coseismic measurements from the Nenana Mt. earthquake (red vectors). White triangles show sites for which we estimate a coseismic correction from the earthquake based on a dislocation model estimated from InSAR data by *Wright et al.* [2003] (yellow box shows their model location and yellow vectors show the corresponding model prediction). We modified this model slightly, finding a better fit to the coseismic GPS data by varying only the location of the fault (blue box), giving us a model correction for the Nenana Mt. earthquake (blue vectors). The epicenter (large red dot) and first motion focal mechanism from AEIC are shown in addition to aftershocks which occurred within 1 hr (red), 5 hr (orange) and a day (yellow) of the earthquake (from AEIC online catalog). The gray star shows the epicenter of the Denali Fault earthquake and the gray thick line shows the corresponding rupture along the Susitna Glacier fault. Black lines show mapped faults in the region [*Plafker et al.*, 1994]. White thick lines are roads.

#### 4.4 Coseismic Displacements

We have estimated coseismic displacements at 232 sites in Alaska and Canada (Table B.4, Figures 4.1, 4.2, 4.4, and 4.5). In general the sites show a typical right-lateral deformation pattern. Sites south of the fault move toward the east and sites north of the fault move toward the west. Sites SW and NE of the fault move toward the fault whereas sites NW and SE move away from the fault (Figures 4.2 and 4.4). The largest horizontal displacements, just over 3 m, were measured at two sites just south of the fault, near Mentasta ( $3.13 \pm 0.02$  m at MEN) and Tok Cutoff ( $3.25 \pm 0.1$  m at MACL) (Figure 4.4). The vertical displacements also show a systematic pattern that is consistent with a strike-slip fault that ruptures the surface [Chinnery, 1965]. In general there is subsidence in the SW and NE corners and uplift in the SE and NW corners of the deformation field (Figure 4.5). Very close to the fault, in the region where maximum surface offset was measured around Tok Cutoff, that pattern of vertical motion is reversed; sites on the north-side of the fault show uplift but sites on the south side show subsidence. The maximum vertical displacement measured was subsidence of  $1.24 \pm 0.05$  m at a site along the Trans-Alaska pipeline (FM11), only a few tens of m from the main fault rupture. Horizontal deformation at the site suggests that it was within a broad distributed deforming zone surrounding the fault. A site just south of the fault, outside the main rupture zone, subsided  $0.71 \pm 0.04$  m (MILC). Uplift of about 0.3 m was measured at several sites just north of the fault, along the Richardson Hwy. Far-field sites included in the analysis (INVK, KODK, KDK1, and SG27) verify that the deformation field does dissipate to zero with distance (Figure 4.1). This indicates that we have successfully determined absolute displacements without systematic biases.

Though we have managed to measure and estimate coseismic displacement at a great number of sites, the distribution of GPS sites is heterogeneous. Displacement uncertainties also vary by 2 orders of magnitude. The sites tend to follow the main road system, with the highest concentration along the Richardson, Parks, and Denali highways (Figure 4.4). Large areas in the near-field of the fault lack any GPS data. In other near-fault regions, however, we have a large number of sites that can give us detailed insight into slip distribution on the fault. We examine in more detail the displacements in several sub-regions, each of which reveals important characteristics of the earthquake slip distribution.

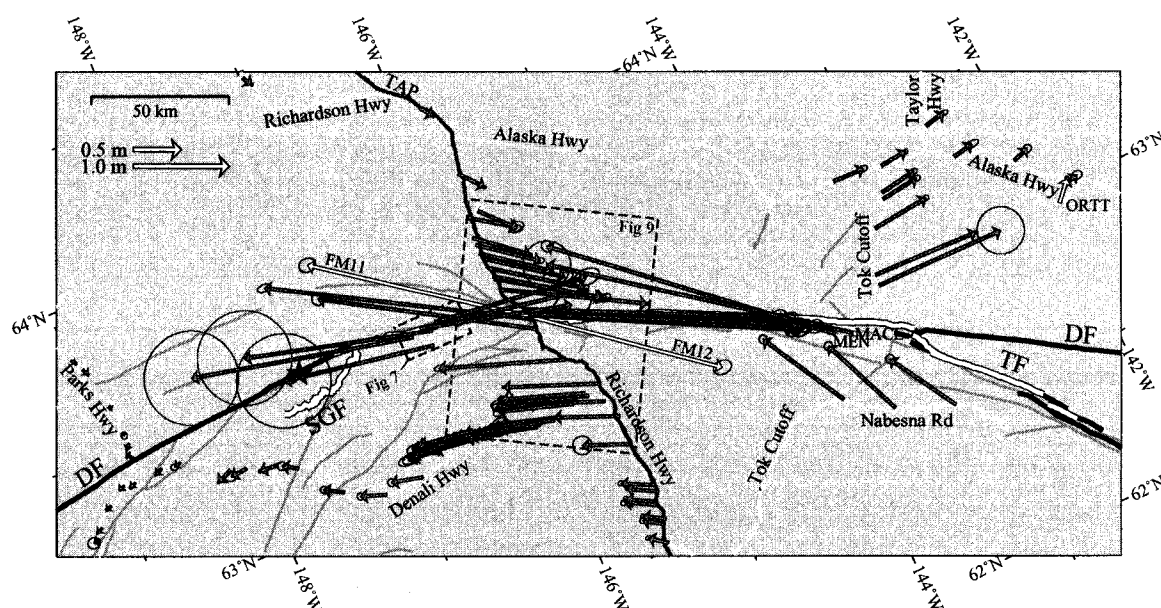


Figure 4.4. Near-field coseismic displacements from the Denali Fault earthquake. The largest horizontal displacements, just over 3 m, were measured at MEN and MACL (Tok Cutoff, just south of the fault). White vectors (FM11, FM12, and ORTT) indicate displacements biased by local effects, as discussed in the text. Green dashed boxes indicate the locations of Figures 4.7 and 4.9. The red star indicates the epicenter of the Denali Fault earthquake and the white line shows the surface rupture along the Susitna Glacier (SGF), Denali (DF) and Totschunda faults (TF) [Eberhart-Phillips *et al.*, 2003]. Other mapped faults are shown with gray lines [Plafker *et al.*, 1994]. The Trans-Alaska pipeline (TAP) and major roads are shown for reference.

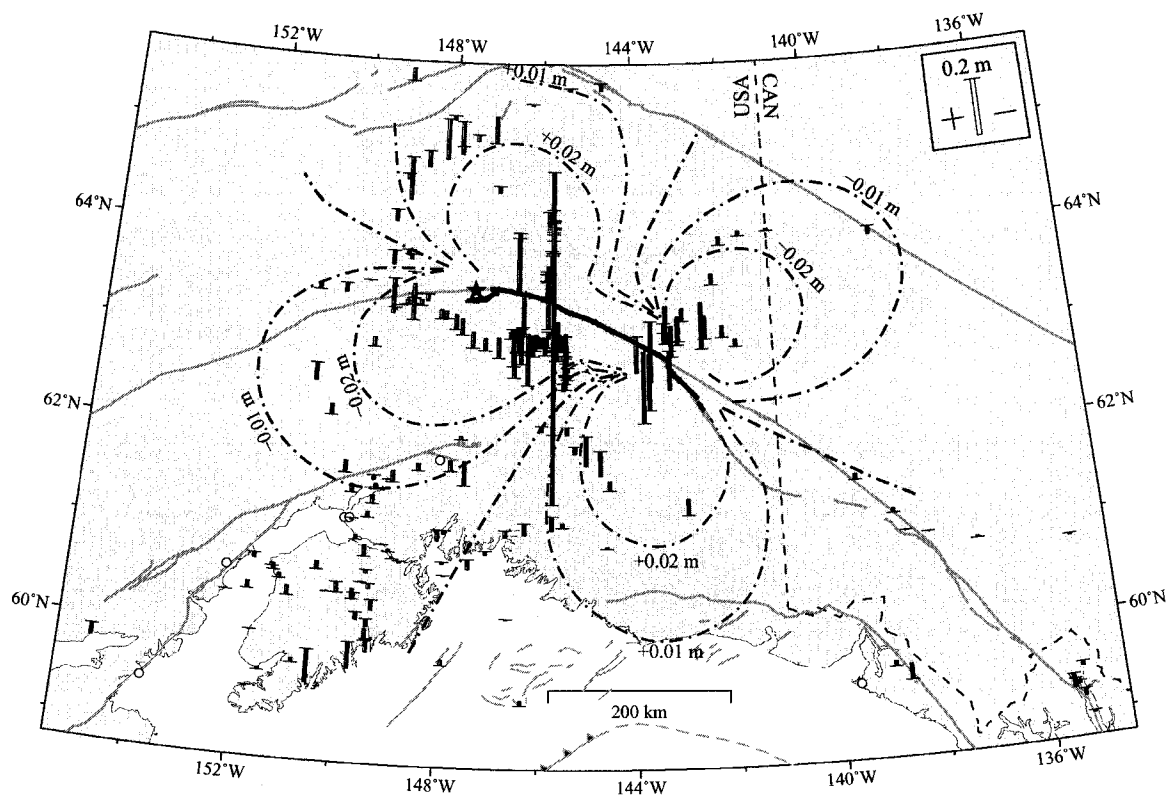


Figure 4.5. Vertical coseismic displacements from the  $M_w$  7.9 Denali Fault earthquake. Subsidence is shown with blue bars and uplift with orange bars. Error bars are not shown for clarity (see Table B.4 for details). Displacements for ORTT, FM11 and FM12 are not shown as their displacements are strongly influenced by local effects. Dashed lines show approximate contour lines for 0.01 m and 0.02 m vertical change (based on model evaluation from Section 4), red indicating uplift and blue indicating subsidence. Sites with  $< 1$  mm vertical change are shown as open circles. The vertical uncertainty varies from  $\sim 0.01$  m to  $\sim 0.2$  m.

#### 4.4.1 Denali Hwy Profile

The Denali Fault earthquake occurred in a remote area. The nearest road to the epicenter, the Denali Hwy, parallels the fault to the south (Figure 4.4). The Denali Hwy lies about 20 km south of the westernmost tip of the Susitna Glacier thrust fault and roughly 40 km south of and parallel to the earthquake rupture along the Denali fault. A dense profile of GPS sites was measured along the eastern part of the highway in the summer of 2002, paralleling the Denali Fault rupture for about 60 km. In addition, sites spaced at  $\sim 20$  km intervals along the highway had been measured earlier. This dataset provides an outstanding along-strike profile (Figure 4.6). The displacements decrease from east to west, with the maximum displacement at the eastern end of  $0.86 \pm 0.02$  m (F113) and displacement at the westernmost site of  $0.067 \pm 0.005$  m (L2C6). The sites subsided about 5 cm on average along the highway. The decreasing horizontal displacements reflect that the highway lies parallel to the western end of the fault rupture. The vectors rotate along the profile, following the curvature of the Denali fault. South of the Susitna Glacier fault we see the effect of the thrust fault on the sites, where displacements are rotated more toward the fault. We see slight variations in displacements along the highway reflecting the slightly variable distance of each site to the fault. For reference we predicted displacements at the Denali Hwy sites using a synthetic model of uniform 4 m right-lateral strike-slip motion down to 18 km depth along the Denali and Totschunda faults, and uniform 4 m thrust motion on the Susitna Glacier fault (using the same fault geometry as in Section 4.2, later), giving a total moment magnitude of  $M_W$  7.9 (Figure 4.6). The dashed line in Figure 4.6 shows the effect of strike-slip motion along the Totschunda and Denali faults, and the solid line adds the displacement caused by slip on the Susitna Glacier fault. The comparison between the east-west component of this reference model and the measurements show that four meters of uniform slip underpredicts the data east of  $146.5^\circ\text{E}$  but overpredicts the data to the west. This indicates variable slip along the Denali fault, with slip increasing from west to east. Geological surface offset data also indicate increasing slip along the Denali fault, reaching a maximum at about 190 km east of the epicenter. The N-S component is more sensitive to the Susitna Glacier thrust fault and shows that the thrust model with uniform 4 m slip does not adequately explain the observations under-predicting measurements in that region.



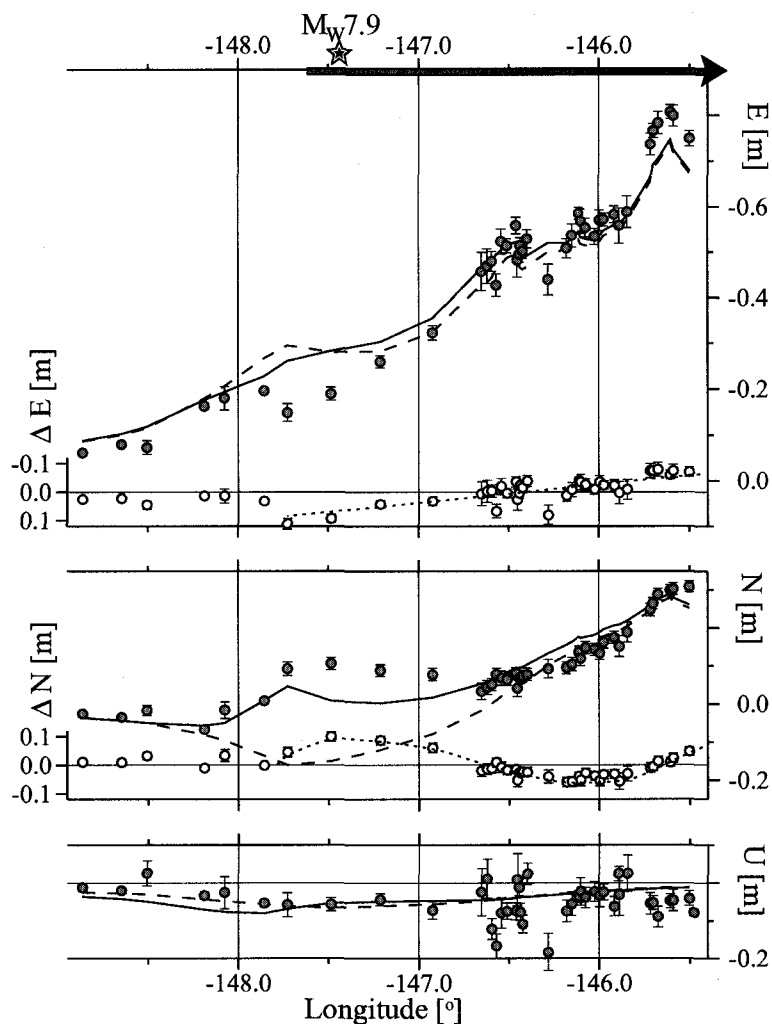


Figure 4.6. GPS data along Denali Hwy, south of and parallel to the Denali fault. The gray dots show the measured coseismic displacements from the earthquake. The star shows the epicenter and the arrow indicates the earthquake rupture. For reference we show a synthetic model of uniform 4 m right-lateral slip on the Denali and Totschunda faults and dip-slip on the Susitna Glacier fault (solid line). The dashed line shows the effect of the strike-slip motion only. The open circles show the misfit between horizontal data and model and dotted lines show the approximate trend of the misfit.

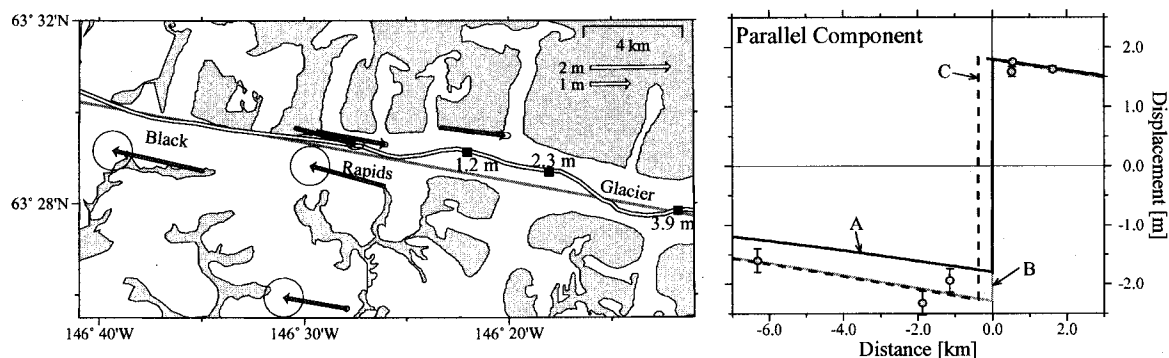


Figure 4.7. Black Rapids Glacier network. The left panel shows the measured coseismic displacements along Black Rapids glacier. Black squares show location of geological measurements along the earthquake rupture. Gray line shows location of 2-d screw dislocation model (azimuth N100.5°E) and outlined line shows the earthquake rupture [Eberhart-Phillips *et al.*, 2003]. The right panel shows a profile of the displacements compared to simple 2-d models. A (black solid line) shows a best fitting model inverting for slip (3.6 m), assuming locking depth of 12 km and a vertical dip. B (gray solid line) shows a best fitting model iterating for both slip (4.1 m) and dip (79° from south). C (dashed) shows a best fitting model, iterating simultaneously for the slip (4.1 m), dip (80° from south), and fault offset of rupture (0.4 km).

#### 4.4.2 Black Rapids Glacier

Of the 340 km of surface rupture, about 99 km broke through glacier ice [Haeussler *et al.*, 2004]. Glaciers made geological measurements of the surface offsets more difficult due to a wider and more complex fault trace. As a result geologists were unable to measure offsets on long stretches along the fault [Haeussler *et al.*, 2004]. The biggest gap in geological data is along the Susitna and Black Rapids glaciers (31 to 55 km distance along the fault from the epicenter).

Six geodetic stations from the Black Rapids Glacier geodetic network were remeasured in May 2003 to estimate coseismic slip of the fault in this region (Figure 4.7). The sites are distributed along about 9 km of the Denali fault (about 44.5 to 53.5 km distance along the fault from the epicenter) and are all within 7 km of the fault. The sites were displaced parallel to the fault in a right-lateral sense, with displacements of up to  $2.3 \pm 0.2$  m at a site on the south side of the fault. The geodetic data suggest a minimum of 3.5 m of slip in the region. The limited geological measurements on the glacier show 1-2 m of slip, and could

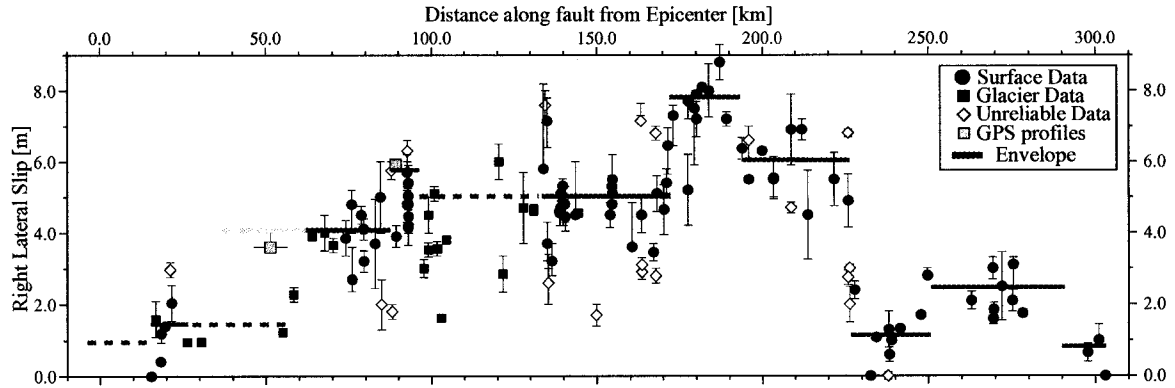


Figure 4.8. Geological surface offset measurements and estimated average slip (graphical method) from *Haeussler et al.* [2004] modified with information from near-fault GPS data (yellow squares). Red circles show reliable surface offset measurements, blue squares measurements from glaciers, and white diamonds show datapoints regarded to be unreliable and culled by *Haeussler et al.* [2004]. *Haeussler et al.* identified 10 slip sections where the amount of surface slip is internally consistent (green lines). GPS data from the Black Rapid Glacier network ( $\sim 50$  km) give slip estimates significantly higher than geologic measurements on the glacier do (section 3.2). GPS data from the Richardson Hwy profile ( $\sim 90$  km) agree with and give similar estimates to nearby surface offset measurements (section 3.3).

be interpreted to indicate slip of 2 m or less for the first 66 km east of the epicenter (Figure 4.8). This discrepancy between the GPS data and geological measurements either suggests that slip on the fault is highly variable in this region or that geological measurements on glacier ice are biased to lower slip values.

Using a simple 2D screw dislocation model we inverted the fault-parallel component of the displacements to estimate slip on the fault (Figure 4.7). We fixed the fault location to roughly match the surface rupture using the local fault strike of  $100.5^\circ$ . Assuming a vertical fault and rupture depth of 12 km we estimated slip of  $3.6 \pm 0.1$  m in the region ( $\chi^2_{dof}=4.3$ ) (profile A). The deformation field does not appear to be symmetrical across the fault. The two sites within 2 km of the rupture on the south side of the fault show larger displacements than the three sites on the north-side of the fault, suggesting a southward fault dip in the region or a mislocation of the fault. Allowing the dip of the fault to vary using a forward scheme we estimated coseismic slip of 4.1 m for a optimal dip of  $79^\circ$  to the south (profile B). According to *Haeussler et al.* [2004] the ice fabric seemed to influence the surface trace,

locally paralleling medial moraines and glacier ogives. This suggests that the fault trace at the surface may not match the fault trace at the base of the glaciers. The glacier is about 2 km wide in this region so the fault trace below the glacier might lie several hundred meters to the south of the mapped glacier surface rupture. Allowing the fault location to vary affects the above results only slightly. Within the 68 % confidence region the fault can lie anywhere beneath the glacier, giving optimal fault offset of 0.4 km, with 4.1 m of slip and dip of  $80^\circ$  to the south.

#### 4.4.3 Richardson Hwy/Trans-Alaska Pipeline Profile

The Richardson Hwy and the Trans-Alaska pipeline cross the fault about 93 km east of the epicenter. Geological surface offsets of  $3.9 \pm 0.3$  m were measured along the highway [Haeussler *et al.*, 2004] but single frequency GPS measurements and photogrammetric surveys along the Trans-Alaska pipeline indicated about 5.8 m of slip across a 1000 m wide zone [Carver *et al.*, 2004]. According to Haeussler *et al.* [2004], this zone is atypical in the sense of being wider than usual, presumably due to the influence of thick Quaternary cover and saturated glacial outwash sediments. Geological measurements 3 km east of the Richardson Hwy did show  $5.7 \pm 0.5$  m of slip.

The GPS dataset gives us a dense N-S profile across the Denali fault rupture with 15 sites located within 5 km of the fault (Figure 4.9). The measurements show right-lateral coseismic deformation in the region. In addition, sites on the south side of the fault subsided in the earthquake, whereas uplift was measured at sites just north of the fault. Displacements of two sites located  $\sim 800$  m north and south of the rupture indicate a total right-lateral offset of  $5.57 \pm 0.05$  m and vertical change of  $0.97 \pm 0.08$  m. Four sites, 500-600 m north of the fault, had on average  $2.82 \pm 0.03$  m of horizontal coseismic displacements, showing increasing displacements toward the fault. The two survey markers closest to the fault on each side are only 130 m apart, about 60 m in the fault-perpendicular direction. They moved in opposite directions (right-lateral sense) by 4.42 m ( $2.38 \pm 0.03$  m at FM11 south of the fault, and  $2.04 \pm 0.04$  m for FM12 north of the fault). This is only 79% of the signal measured between the sites 800 m from the fault and strongly indicates that these two sites are within a broad deforming zone surrounding the fault. Both sites had significant motion, about 0.02 m, toward the fault, and the site south of the fault subsided  $1.24 \pm 0.05$  m. The

GPS data indicate that the width of the deforming zone is wider than 60 m but narrower than 1000 m.

In order to get a better estimate for average slip on the fault in this region, we estimate the slip and rupture width for a simple 2D screw dislocation model that best fit the data within 30 km of the fault, excluding the two sites (FM11 and FM12) that appear to be within the deforming zone around the fault. The strike of the Denali fault where the Richardson Hwy crosses the fault is about  $123^\circ$  [M. Metz, pers. comm. 2003; T. E. Dawson, pers. comm. 2004]. However the average strike for a 30 km section of the fault in this region is about  $120^\circ$ . We use this average strike to estimate the components of the deformation field, fault-parallel and perpendicular to the fault (Figure 4.10). Inversion of the parallel component of the GPS displacements gives an estimate of  $5.81 \pm 0.02$  m of slip, and a rupture width of  $10.56 \pm 0.07$  km with  $\chi_{dof}^2 = 75$ . This very high  $\chi_{dof}^2$  indicates the model's poor ability to explain the data. The model gives a good fit to sites near the fault but at sites more than 5 km from the fault the fit worsens; sites north of the fault moved less than the model predicts and sites on the south of the fault moved more than the model predicts. This poor model fit to far-field data could be attributed to both complex fault geometry and variation in slip along the fault. The fault is not a simple infinite plane as assumed by the screw dislocation. The fault rupture curves in an arcuate shape, thus focusing displacements inside the arc (south side of the fault). The near-fault data are less sensitive to the fault curvature and variation in slip along the fault. Inversion of GPS data within 5 km of the fault, fixing the rupture width at 11 km, gives a slip of  $5.91 \pm 0.02$  m with  $\chi_{dof}^2 = 5.6$ . The near-fault data do not favor a dipping fault. Using a forward scheme we found a best fit slip of  $5.9 \pm 0.1$  m and dip of  $90 \pm 2^\circ$  for the near-fault data.

Deformation at near-fault sites suggests a significant component of dip-slip in the region. We see displacement away from the fault and uplift at near-fault sites north of the fault but displacement toward the fault and subsidence at sites just south of the fault. We use a very simple edge dislocation to find a best fit dip-slip and rupture width for the vertical data. A best fit model gives a vertical motion of 0.83 m, north-side up, with possible slip values from 0.5 to 1.3 m within a 68% confidence region. The vertical motion requires a shallower rupture width than the fault-parallel model with the best fit depth of 6 km ( $\chi_{dof}^2 = 10.6$ ). The perpendicular component of the horizontal displacement field is strongly affected by

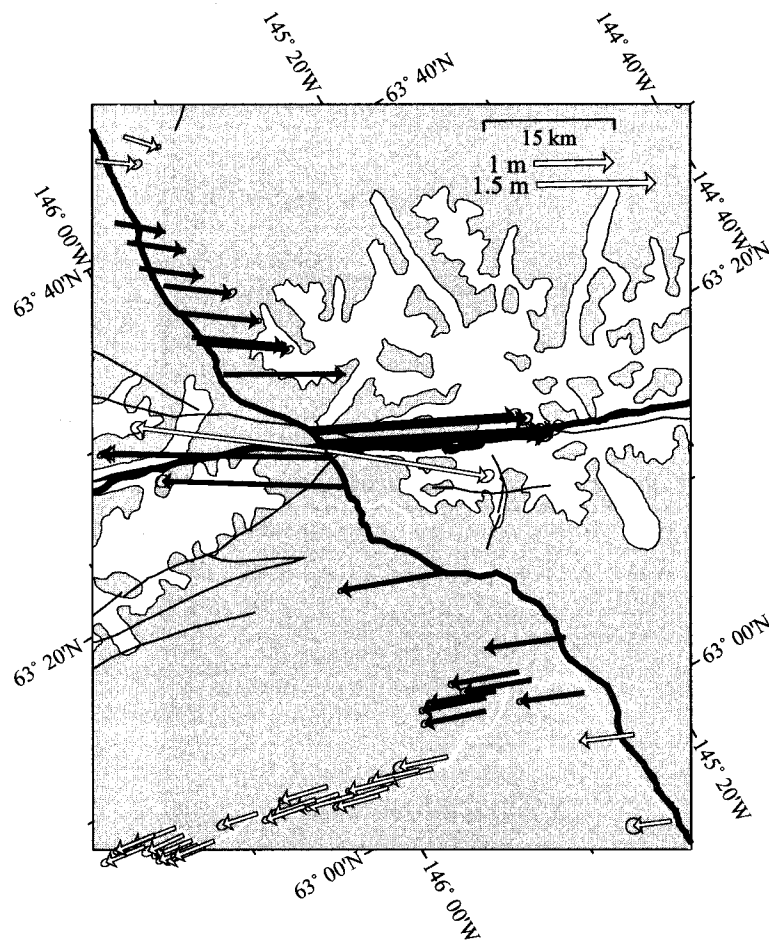


Figure 4.9. Coseismic displacements along Richardson Hwy profile. Blue vectors indicate sites within 30 km distance of the surface rupture and yellow vectors indicate sites more than 30 km distance. White vectors show sites within the deforming rupture zone (FM11 and FM12). The earthquake rupture is shown with a thick red line, mapped faults with thin black lines, the TAP with a thick brown line and roads with white thick lines. White areas indicate glaciated regions.

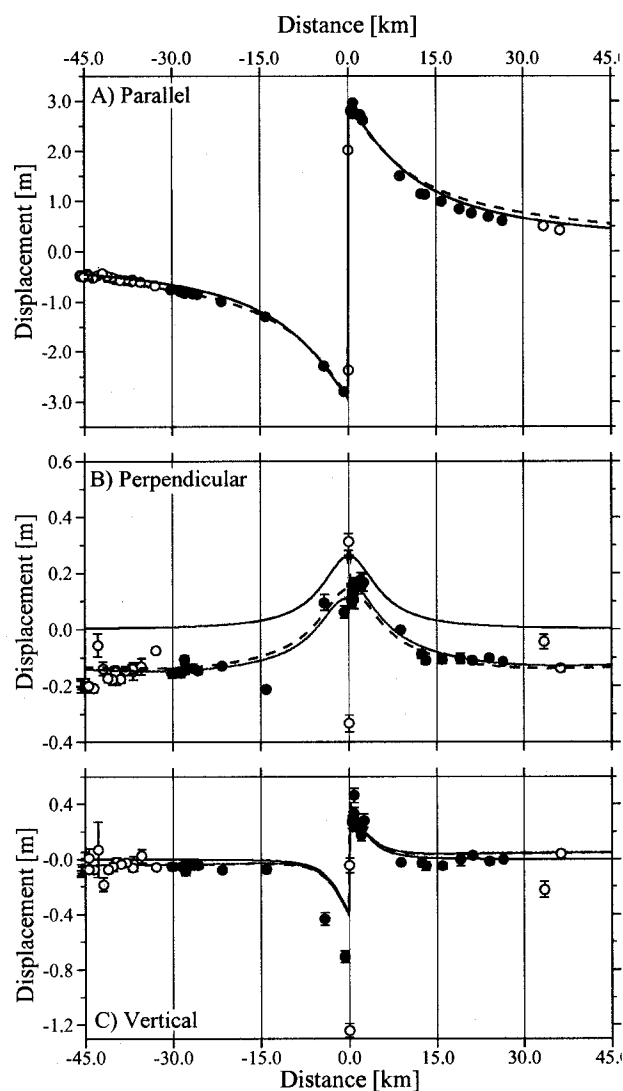


Figure 4.10. Richardson Hwy Profile (azimuth  $N120^{\circ}E$ ). Blue dots indicate sites within 30 km distance of the fault and yellow dots indicate sites more than 30 km distance. White dots show sites (FM11 and FM12) located within the brittle deforming rupture zone that were not used when estimating 2d model profiles. A best fit screw dislocation model (A - black line) suggests right-lateral strike-slip of 5.9 m and rupture width of about 11 km. A simple edge dislocation (assuming vertical fault) that best fits the vertical component (C) suggests dip-slip of 0.8 m (north-side up) and rupture width of 6 km (red lines). Allowing variable strike-slip along strike, with higher slip east of the profile and lower slip west of the profile, we get a much improved fit for the perpendicular data (dashed lines). Allowing a slightly dipping fault further improves the fit to the perpendicular component (green lines) but by changing the strike by only  $1^{\circ}$  a vertical fault would fit the data better.

additional signals. Far-field sites show displacements toward the fault at sites north of the fault but displacements away from the fault south of the fault. This pattern strongly indicates variable slip along the fault, with higher slip to the east. We cannot therefore reliably estimate the dip-slip from the horizontal data without taking a more complicated slip distribution into account. However, the model estimated from the vertical data with the addition of a high strike-slip patch a few tens of km east of the Trans-Alaska pipeline crossing fits the perpendicular component of the GPS data reasonably well. Allowing the fault to dip slightly off vertical (about  $85^\circ$  south) we get an improved fit to the data. The perpendicular component is very sensitive to any variation in strike; for a strike of  $119^\circ$ , a vertical fault fits the data better than a dipping fault.

The GPS data along the profile suggest about 5.9 m of strike-slip motion and 0.8 m of dip-slip on a near vertical fault. The profile shows the effect of variable slip along the fault and curvature of the fault. It is apparent that simple 2-D models are not adequate to study this size earthquake with the complex fault geometry.

## 4.5 Inversion on 3D Fault Model in Elastic Half Space

### 4.5.1 Data

We use the GPS data to invert for the coseismic slip distribution of the Denali Fault earthquake. We use 224 GPS sites in the inversion, excluding faraway sites (Figure 4.1) in addition to three sites biased by local effects. FM11 and FM12 are located within a broad brittle deforming zone around the fault, and the site ORTT is located within a zone of large liquefaction effects from the earthquake. All three sites showed displacements very different from those of surrounding sites.

In addition to the GPS data we have surface offset data along the Denali and Totschunda faults from *Haeussler et al.* [2004] (Figure 4.8). We ran inversions of the GPS data both with and without the surface offset data. We excluded all measurements from glaciers as they have been shown to be unreliable (see section 3.2). We also decreased the weight of each surface offset measurement by adding  $\pm 0.5$  m uncertainty to the measurement uncertainty. For sites where lateral slip was measured but not the dip-slip we assumed zero dip-slip but assigned a large uncertainty,  $0 \pm 2$  m.



#### 4.5.2 Fault Model

We use an 11-plane geometric approximation to the Denali, Totschunda and Susitna Glacier faults, dividing each plane into  $3 \text{ km} \times 3 \text{ km}$  tiles. For the Susitna Glacier fault we used a two plane approximation to the fault, dividing the fault into upper and lower planes. The upper plane, from 0 to 2 km depth, intersects the surface roughly at the observed surface rupture with a dip of  $19^\circ$  to match estimates from geological field-measurements [Crone *et al.*, 2004]. From 2 to 8.6 km depth we use a plane with a dip of  $48^\circ$  to match the first motion focal mechanism from the local network [Ratchkovski *et al.*, 2003]. The lower plane intersects with the Denali fault at its base. Both planes have a strike of  $81^\circ$  to match the first motion focal mechanism and surface rupture. For the Totschunda fault we use a 2-plane approximation to the surface rupture. Relocated aftershocks delineate a simple vertical plane along the fault with an indication of more complex faulting near the end of the mapped rupture [Ratchkovski *et al.*, 2004]. We therefore assume a vertical dip along the fault, extending both planes from the surface to 18 km depth. For the Denali fault we use a 7-plane approximation to the surface rupture [Eberhart-Phillips *et al.*, 2003], extending the westernmost plane west of the epicenter along the Denali fault where discontinuous ground cracks, with no apparent offset, were observed after the earthquake [Haeussler *et al.*, 2004]. We limited its western extent to match the down dip end of the Susitna Glacier fault because Hreinsdóttir *et al.* [2003] have previously concluded that the  $M_W$  7.9 Denali Fault earthquake did not rerupture the  $M_W$  6.7 Nenana Mt. earthquake rupture zone to the west. We did not extend the model east along the Denali fault past the Denali-Totschunda fault junction, as both the surface rupture and aftershocks step over to the Totschunda fault and abandon the main Denali fault trace in that region [Haeussler *et al.*, 2004; Ratchkovski *et al.*, 2004]. Relocated aftershocks from the Denali Fault earthquake show rather diffuse seismicity along the Denali fault with the majority of aftershocks within the upper 12 km of the crust but not restricted to the main ruptured fault plane [Ratchkovski *et al.*, 2004]. Surface offset measurements indicate a subvertical fault in most locations [Haeussler *et al.*, in press 2004]. This agrees with our models from the Richardson Hwy profile of a near vertical fault. We assume a vertical dip along the Denali fault, extending all planes from the surface to 18 km depth.

### 4.5.3 Inversion Method

We used a damped least-squares inversion scheme [Price and Bürgmann, 2002] to estimate the optimal coseismic slip value on each model fault tile from the geodetic data. For the GPS data we computed the Green's functions,  $\mathbf{G}$ , relating slip on each fault tile,  $\vec{s}_i$ , to displacement at each GPS site,  $\vec{d}_j$ , assuming an elastic half-space and a Poisson's ratio of 0.25,  $\mathbf{G}\vec{s} = \vec{d}$  [Okada, 1985]. For the surface offset data we directly relate measured surface offset to slip at a corresponding tile,  $\vec{s} = \vec{d}$ .

We have reliable surface data on 47 of 107 surface tiles along the Denali and Totschunda faults. We use the largest right-lateral offset measured within each tile under the assumption that maximum measured offset best reflects the actual offset in the earthquake [P. Haeussler, pers. comm., 2004]. This is also consistent with our observations from the Richardson Hwy profile in the TAP corridor (Section 3.3, Figure 4.8). The thrust motion on the Susitna Glacier fault produced a complex pattern of surface rupture. According to Crone *et al.* [2004] the typical near-surface dip-slip was on the order of 4.0 m (assuming a dip of 19°), with the majority of surface offsets ranging from 3 to 5 m dip-slip and no significant lateral slip along the fault. We do not have adequate GPS data coverage to resolve the shallow slip distribution on the Susitna Glacier fault so we rely primarily on the surface observations. We use this reported typical near-surface dip-slip of  $4 \pm 2$  m and strike-slip of  $0 \pm 1$  m to relate slip on all 11 Susitna Glacier surface tiles.

We use 763 data (221 three-component GPS data, 3 two-component EDM-GPS data, and 47 two-component surface offset data) to estimate 1394 model parameters (dip-slip and strike-slip at 697 tiles) with additional constraints on the surface tiles of the Susitna Glacier fault (22 parameters). We constrain the slip on each model tile using a bounded variable least squares (BVLS) algorithm [Stark and Parker, 1995]. We restricted the slip to right-lateral strike-slip motion and north-side up dip-slip in accord with geological measurements [Crone *et al.*, 2004; Haeussler *et al.*, 2004]. We put upper bounds of 3 m dip-slip for the Denali and Totschunda faults but the maximum measured vertical surface offset was 2.7 m in the Denali-Totschunda fault transfer zone. The bounds on the inversion are tested and discussed more fully in section 4.4.

In order to make the under determined problem stable we add smoothing constraints, applying discrete Laplacian smoothing between tiles. We measure roughness using the

Laplacian operator,  $\mathbf{L}$ , weight roughness using a smoothing factor,  $\beta$ , and minimize the weighted residual sum of squares (WRSS) and the roughness of the model:

$$\underbrace{\|\mathbf{W}(\mathbf{G}\vec{s} - \vec{d})\|^2}_{\text{misfit}} + \beta^2 \underbrace{\|\mathbf{L}\vec{s}\|^2}_{\text{roughness}} \quad (4.5)$$

( $\mathbf{W}^T\mathbf{W} = \mathbf{\Sigma}^{-1}$  where  $\mathbf{\Sigma}$  is the data covariance matrix, here containing the variance of the displacement measurements and the covariances between the east, north, and up components of the GPS data.) Changing  $\beta$  changes the relative importance assigned to data fit and smoothness, and produces a family of models with varying misfit and roughness (Figure 4.11). We estimate a range of smoothing factors for which the solution fits the data well, but is not excessively rough, giving a reasonable smoothing parameter  $\beta \sim 2$  to  $3 \text{ km}^2/\text{m}$ . Selecting the smoothing factor based only on a tradeoff curve can be highly subjective, so we also estimate the model's ability to predict observations using the Weighted Cross-Validation Sum of Squares (WCVSS) [Matthews and Segall, 1993]. Each station in turn is taken out of the data set and its displacement predicted based on a model fit to the other data. The WCVSS is the weighted sum of squares of the predicted residuals and gives us optimal smoothing for  $\beta = 7 \text{ km}^2/\text{m}$  (Figure 4.11). This smoothing factor, however, gives a much smoother solution than we consider reasonable given the high misfit ( $\sim 20\%$  higher WRSS than for  $\beta = 2$ ). The WCVSS is dominated by sites close to the earthquake rupture but relatively isolated from other sites. The smoother the model, the better prediction we get for such isolated near-fault sites. In order to compromise between the two we consider reasonable smoothing factors to be in the range from  $2.5$  to  $7 \text{ km}^2/\text{m}$ , with smoothing of  $\beta = 4 \text{ km}^2/\text{m}$  being the best compromise between fit to the data and prediction ability. In Figure 4.12 the range of reasonable models is shown, from the smoothest to the roughest. The models estimated within this range of smoothing values are all very similar; 3-6 m dip-slip on the Susitna Glacier fault, highly variable, up to 11 m predominantly strike-slip motion on the Denali fault and relatively low (1-3 m) strike-slip motion at shallow depths on the Totschunda fault.

The preferred slip model (Figure 4.13) fits the GPS data well. Only a few sites have residuals that exceed 95% confidence, and the misfit seems to be random (Figure 4.14). This misfit could be a result of inadequate postseismic correction, in particular at near-fault sites,

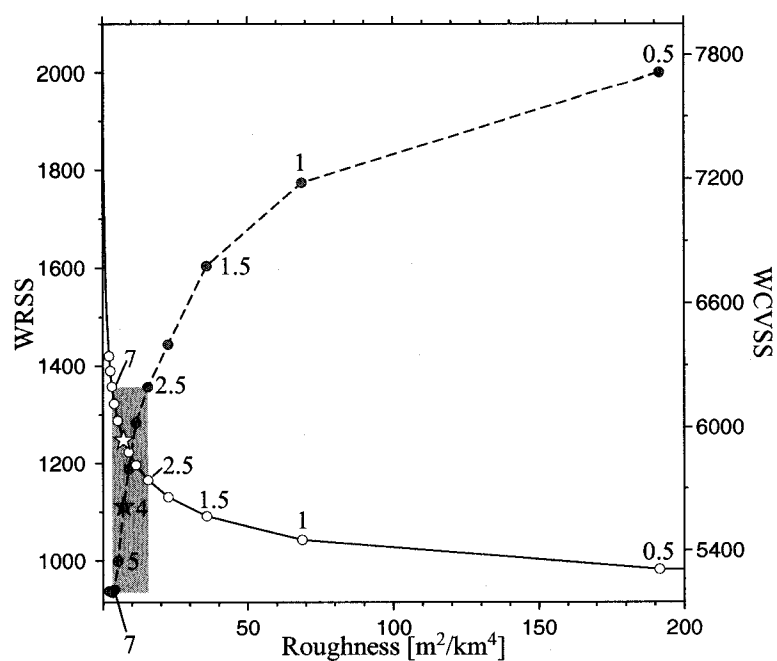


Figure 4.11. Weighted residual sum of squares (solid line) and weighted cross-validation sum of squares (dashed line) were used to estimate optimal smoothing parameter for the inversion. We estimate a range of reasonable smoothing factors (shaded region) with  $\beta = 4 \text{ km}^2/\text{m}$  giving the optimal smoothing (stars). Labels at data points indicate smoothing factor (in  $\text{km}^2/\text{m}$ ).

and/or interseismic correction and unaccounted for measurement errors.

#### 4.5.4 Coseismic Slip Distribution

The preferred coseismic slip model ( $\beta = 4 \text{ km}^2/\text{m}$ ) reveals a heterogeneous slip distribution along the Susitna Glacier (SGF), Denali (DF1-DF7), and Totschunda (TF1-TF2) faults (Figure 4.13) with a total moment of  $6.81 \times 10^{20} \text{ Nm}$  ( $M_W$  7.89) assuming a rigidity of 30 GPa. We see about 4.7 m average dip-slip on the Susitna Glacier fault (moment magnitude of  $M_W$  7.2), but we lack data close to the fault to resolve the slip distribution in any detail. On the Denali fault we see mostly right-lateral strike-slip motion with increasing slip from west to east. There is little or no slip on the Denali fault in the epicentral region (DF1) where discontinuous cracks were found at the surface. Moderate slip, smoothly varying from 1-4 m, is estimated about 20 to 60 km east of the epicenter (DF2) where aftershock activity was low. A significant component of north-side up dip-slip is estimated in this region. From about 60 to 140 km from the epicenter (DF3-DF5) we estimate highly variable slip with 3 larger slip patches (slip exceeding 8 m) about 85, 105, and 130 km east of the epicenter. A significant component of dip-slip was estimated at shallow depths from 60 up to about 90 km from the epicenter. From about 140 to 170 km east of the epicenter (DF6), intermediate ( $\sim 5 \text{ m}$ ) but shallow (0-9 km) strike-slip is estimated. From about 180 to 200 km east of the epicenter (about 40 km west of the Denali-Totschunda fault junction) we see a large patch of high and slightly oblique slip (an average of 8.9 m over a  $15 \text{ km} \times 18 \text{ km}$  area of the fault). This coincides with where geological observations estimate maximum slip of 8.8 m. In general we see fairly shallow (0-9 km) and relatively low (1-3 m) strike-slip on the Totschunda fault (TF1-TF2). However, just east of the Denali-Totschunda fault junction we estimate high slip with a large component of dip-slip. This might be a result of our model being too simple in the stepover region where surface faulting was discontinuous and geometrically complex.

The majority of slip occurs at 0-9 km depth which coincides with the depth range of the majority of aftershocks [Ratchkovski *et al.*, 2004]. In general the slip tapers off at greater depth but we do see significant slip below the aftershock zone coinciding with the main slip patches along the fault. In order to test the maximum depth of slip required by the data we ran models varying the maximum depth of the Denali and Totschunda faults from 9 to

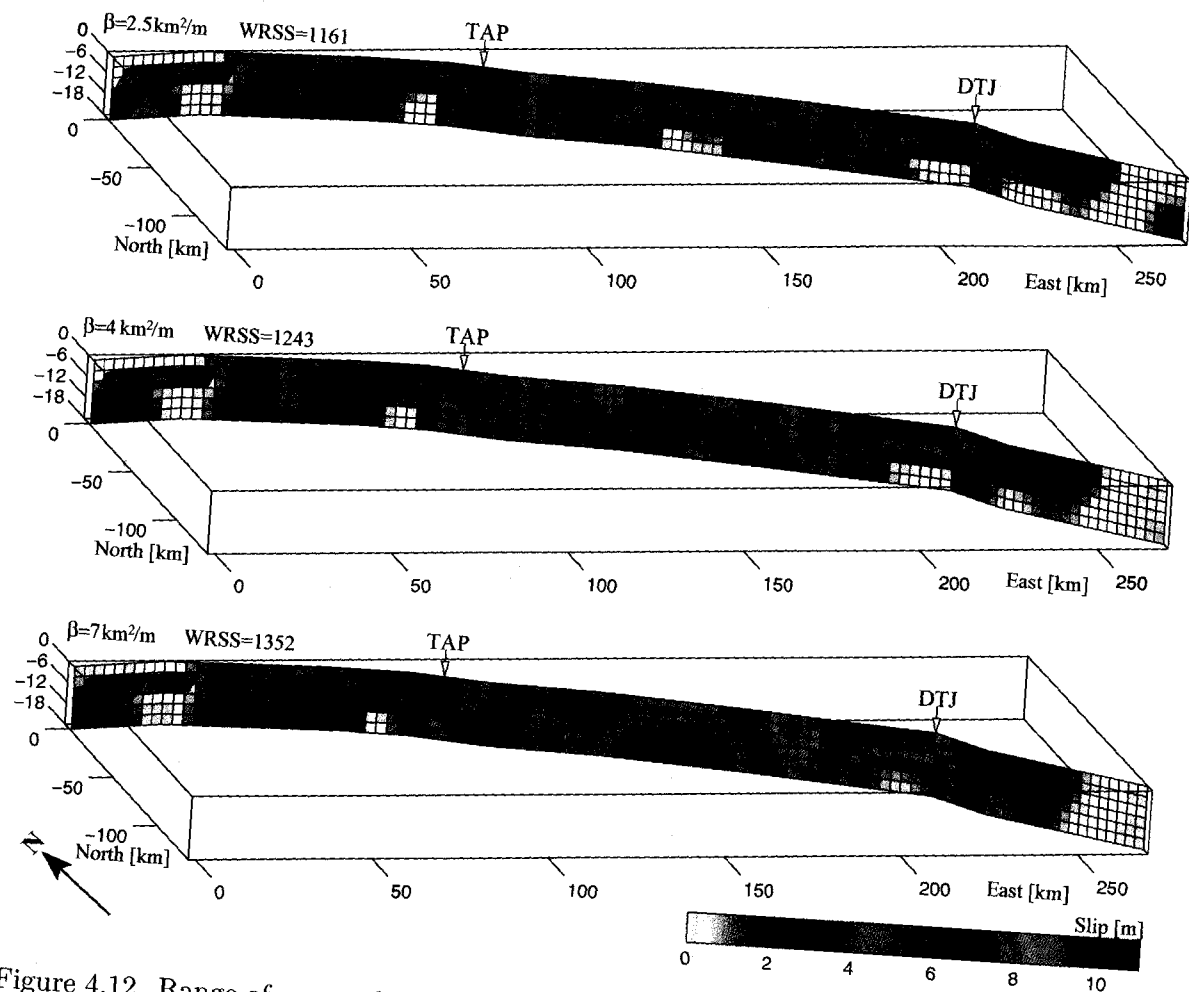


Figure 4.12. Range of reasonable coseismic slip models from the roughest ( $\beta = 2.5 \text{ km}^2/\text{m}$ ) to the smoothest ( $\beta = 7 \text{ km}^2/\text{m}$ ). The axes show easting, northing and depth in km. TAP-Trans-Alaska pipeline, DTJ-Denali-Totschunda fault junction. The red star indicates the Denali Fault earthquake hypocenter.

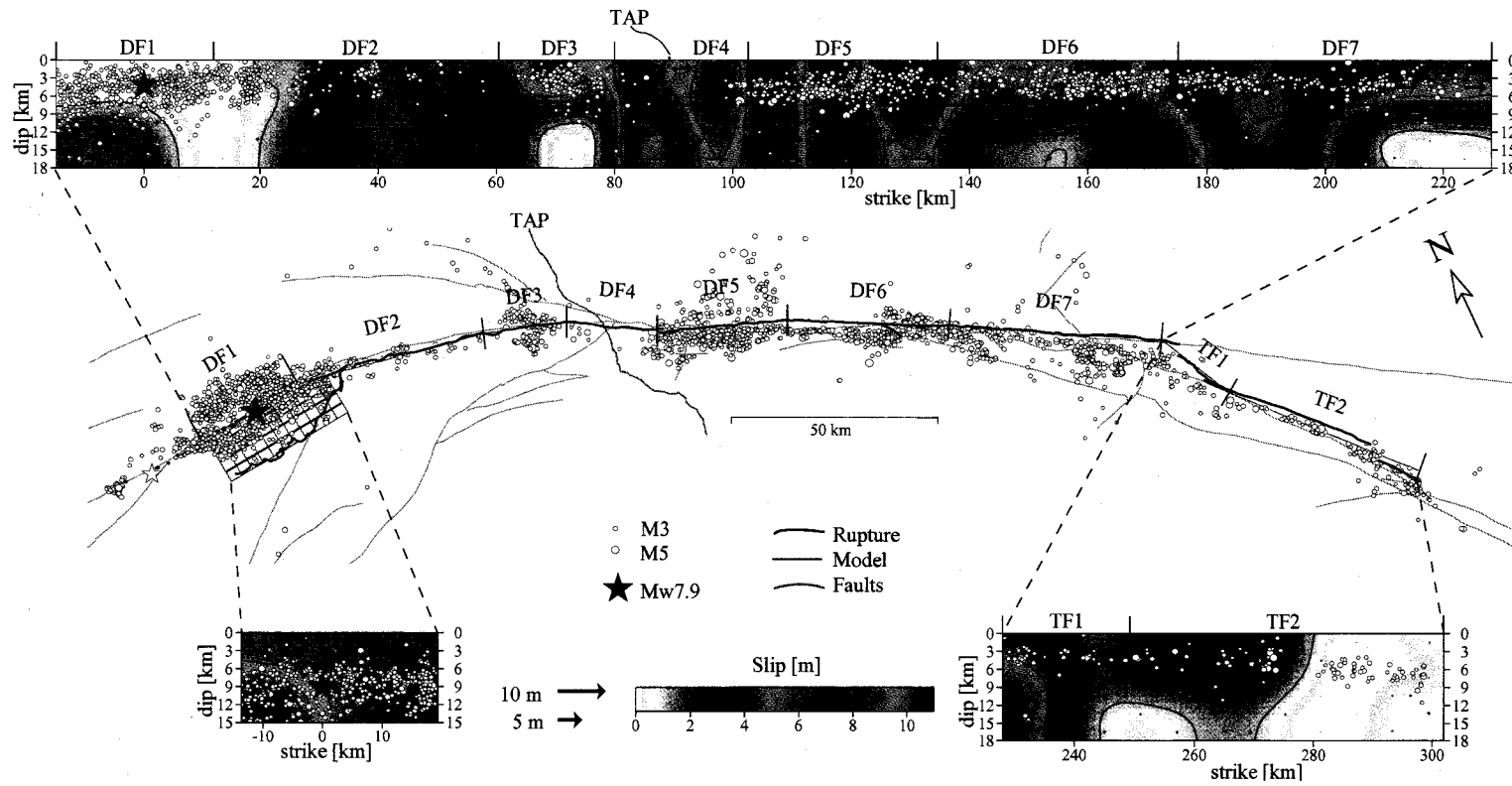


Figure 4.13. Coseismic slip model of the Denali Fault earthquake ( $\beta = 4 \text{ km}^2/\text{m}$ ). Center panel shows the earthquake rupture (red line) and fault model (green line) used in the inversion. The Denali fault (upper panel) is divided into seven planes (DF1-7), Totschunda fault (lower right panel) in two (TF1-2), and the Susitna Glacier fault (lower left panel) in two (SGF1-2). In the lower panel we show the estimated coseismic slip distribution, with vectors indicating slip direction and scale of the north-side relative to an observer on the south side. Relocated aftershocks from *Ratchkovski et al.* [2004] are shown for reference and the hypocenter of the earthquake is indicated with red stars. TAP-Trans-Alaska pipeline. Faults from [Plafker et al., 1994].

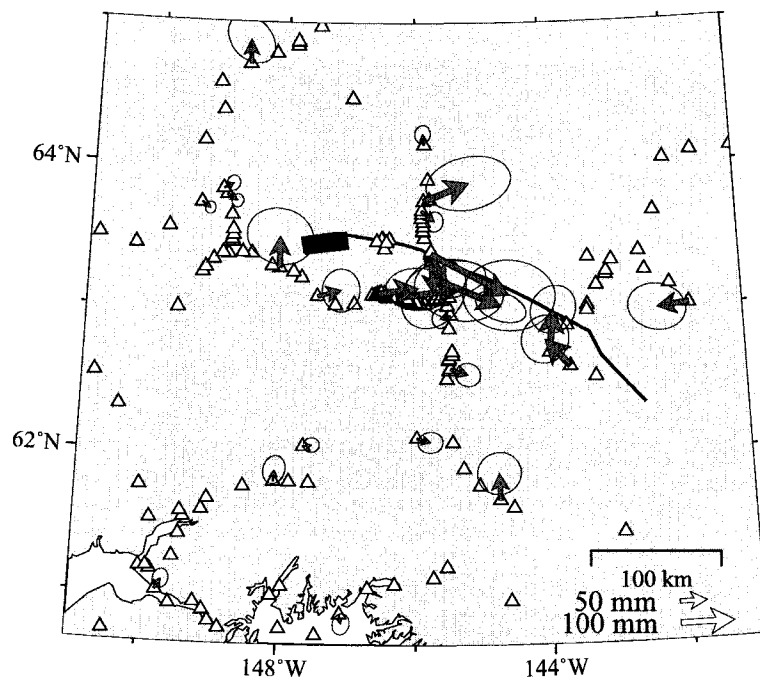


Figure 4.14. Model residuals exceeding 95% confidence region of measured displacements. Triangles show all sites used in the inversion within the region. The fault model is shown with black line.



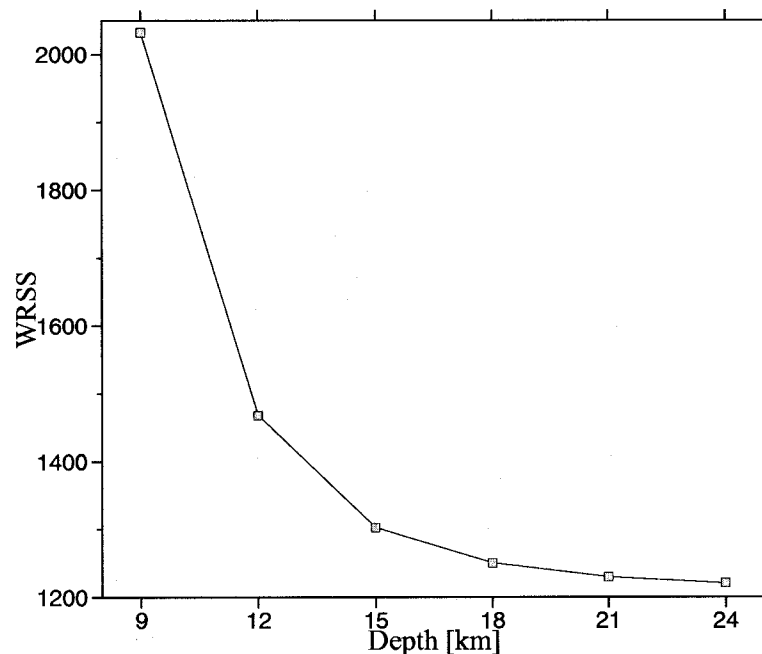


Figure 4.15. Weighted Residual Sum of Squares as a function of maximum depth of slip allowed in the model. We see a greatly improved fit to data (about 15% lower misfit) when extending the model from 12 to 18 km depth but only a small (about 2%) improvement when the maximum depth of slip is increased from 18 to 24 km depth.

24 km, keeping all other parameters, including the tile size and smoothing factor, the same (Figure 4.15). The misfit decreases significantly when increasing the maximum depth of slip from shallow (9 km) to intermediate (15 km) depth, but there is little improvement of the fit by allowing slip deeper than 18 km. From this we conclude that our model covers a sufficient depth range for the GPS data and significant slip is not required below 18 km given the assumed elastic half-space model. (Layered models do, in general, show slip at greater depths than elastic half-space models, e.g. *Hearn and Bürgmann* [submitted 2004]).

In Figure 4.16 we show the comparison between the modeled slip at the surface and the geological surface offset data from *Haeussler et al.* [2004] used in the inversion. We excluded all data from glaciers (blue squares) and only used the largest lateral offset measurement within each tile (red circles) in the inversion. The comparison between the model and the surface offset data is extremely good. In fact, model estimates based only on GPS data

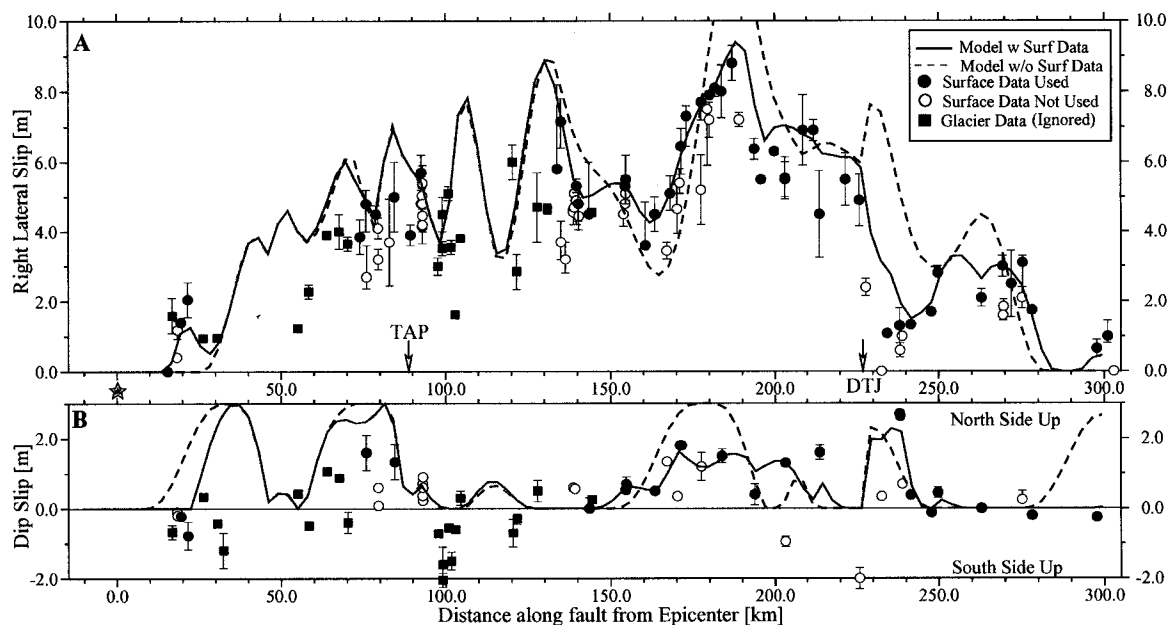


Figure 4.16. Comparison between modeled surface offset (lines) and geological surface offset data. A) Lateral offset, B) vertical offset. The location of the Trans-Alaska pipeline crossing (TAP) and the Denali-Totschunda fault junction (DTJ) is shown for reference. Geological offset data from *Haeussler et al.* [2004]. Distance shown as distance from epicenter along fault model. See text for an explanation of which surface offset data were used.

also agree very well with the geologic data (dashed line). From the epicenter to about 140 km east of the epicenter we get almost the same surface slip estimates but further east, where the GPS data coverage is not as good the surface offset data provide more significant constraints.

Geological surface offset measurements show dominantly north-side up motion along the Denali fault, the only exceptions being in limited areas at the eastern and western ends of the Denali fault rupture where south-side up dip-slip was measured [*Haeussler et al.*, 2004] (Figure 4.16). We therefore restricted the dip-slip component at all tiles to north-side up. Allowing north-side up dip-slip along the Denali and Totschunda faults decreases the misfit to the GPS data by about 30%, while inversions allowing only south-side up dip-slip show very small (2% or less) improvement in fit to data (Figure 4.17).

We set 3 m bounds on the dip-slip in accord with the maximum observed vertical surface offset (2.7 m). We ran tests to see if this constraint limits the quality of the model fit to

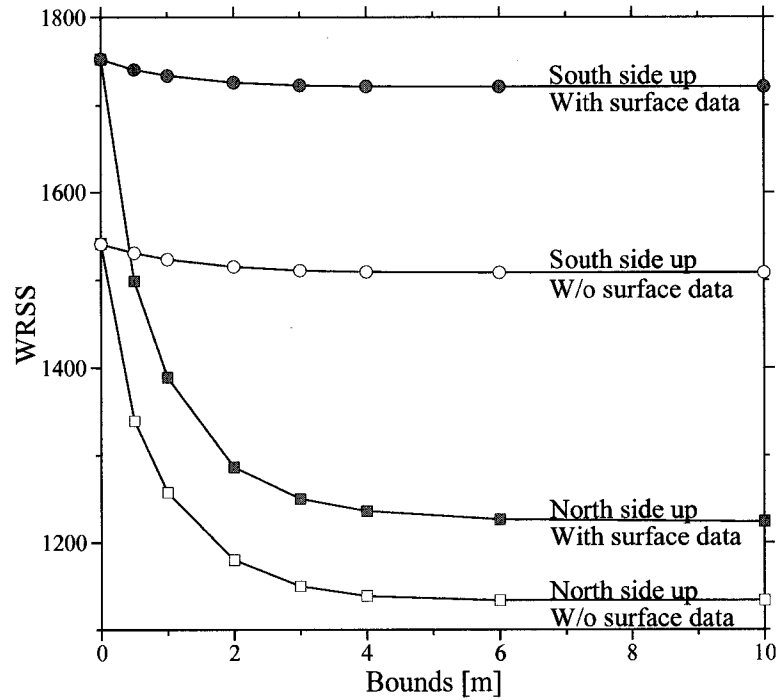


Figure 4.17. Weighted Residual Sum of Squares as a function of dip-slip bounds in the BVLS inversion. When allowing only north-side up dip-slip (squares) we get about a 30% improvement in fit to data whereas allowing only south-side up dip-slip (circles) only results in 2% improvement. Inversions without surface offset data show the same trend (white points). There is little improvement in the misfit when the slip bounds are relaxed to allow more than 3 m dip-slip.

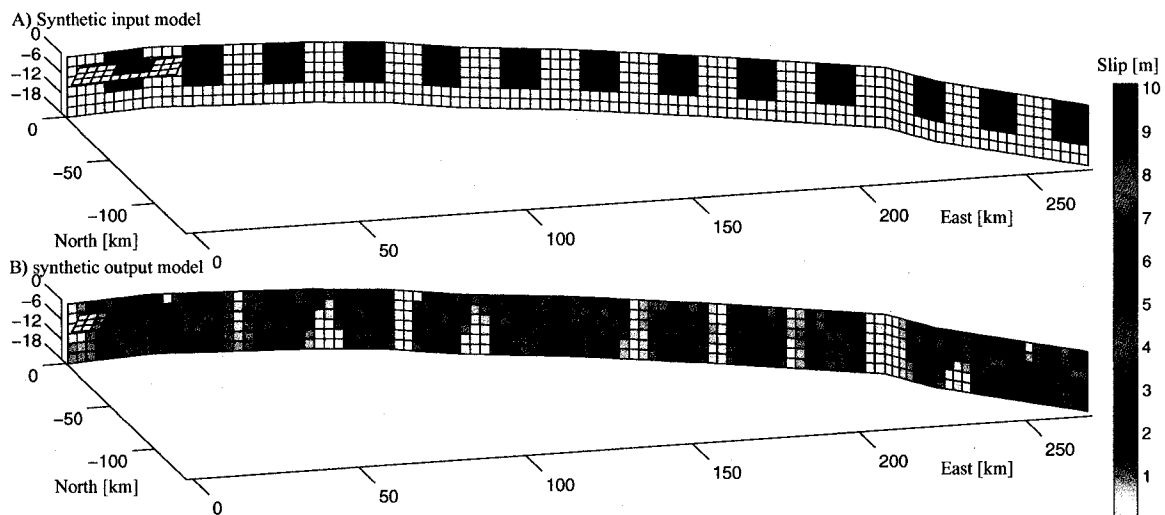


Figure 4.18. Inversion result from a synthetic dataset calculated using a synthetic checkerboard model of  $12 \text{ km} \times 12 \text{ km}$  slip patches with 10 m right-lateral strike-slip.

the data, but models both with and without the surface data do not show significantly improved fit when allowing more dip-slip (Figure 4.17).

#### 4.5.5 Resolution and Uncertainty

We conducted a series of synthetic tests to assess the resolution and precision of the coseismic slip model. We calculated displacements at the GPS sites and surface offsets for synthetic slip models (examples shown in Figure 4.18 and 19). We then inverted the synthetic datasets for the slip distribution on the fault using our optimal smoothing value. We did not apply any noise to the data but assumed the same uncertainty for the synthetic data set as that of the measured coseismic data.

We started with very simple uniform slip models with right-lateral strike-slip on the Denali and Totschunda faults and thrust motion on the Susitna Glacier fault. Inverting the synthetic dataset from a uniform 4 m slip model, we recovered the input slip model almost exactly. We tested slip models that were uniform with depth but varying along strike. The resulting inverse models are only slightly smoother versions of the synthetic models. Where the GPS data coverage is the most dense (around the Trans-Alaska pipeline crossing) the models recover the sharp edges in the input slip model with smearing across only 2 tiles (6

km). Smearing increases with depth.

We assessed the resolution further using checkerboard tests with patches of 10 m slip separated by patches of no slip both along strike and with depth. With a  $3 \text{ km} \times 3 \text{ km}$  synthetic checkerboard models we only recovered good resolution along surface tiles that are close to near-fault GPS data; along the Black Rapids Glacier network ( $\sim 50 \text{ km}$  east of the epicenter), the Richardson Hwy profile ( $\sim 90 \text{ km}$  east of the epicenter) and around Mentasta ( $\sim 30 \text{ km}$  west of the Denali-Totschunda fault junction). In other places and at depth the checkerboard pattern is significantly smeared. With increasing patch size we can resolve more of the slip patches. For  $9 \text{ km} \times 9 \text{ km}$  checkerboard tests, the near-surface tiles where we have surface offset data are well resolved. For tests with  $12 \text{ km} \times 12 \text{ km}$  checkerboard models (Figure 4.18), all shallow patches can be identified in the resulting slip models. Some are considerably smeared out but others are reasonably sharp along strike. All are smeared at their lower edges, indicating the expected loss of resolution with depth. For slip patches at 3-15 km depth we can resolve well slip patches located from about 60 to 110 km and about 210 to 225 km east of epicenter. Other slip patches get pushed down and smeared out along the bottom tiles.

We also examined a simple synthetic model for which the inverted synthetic data give a slip model that strongly resembles the best coseismic slip model (Figure 4.19). We kept the synthetic model as simple as possible. We put higher slip patches (both strike-slip and dip-slip) on top of a uniform slip model in order to reconstruct the general features of the coseismic slip model. This test shows how rough a slip distribution might be and still produce an estimated model like the one we determine. In most places along the fault it was straightforward to construct the synthetic model. However for a patch about 110 km from the epicenter, we had to put a deep high slip patch (15 m) in order to get something that even resembles the coseismic slip model.

We used this synthetic model to evaluate the uncertainty of the estimated coseismic slip distribution using a Monte Carlo simulation. Noise with the same distribution as the covariance of the real data was applied to the synthetic GPS and surface offset data and the modified dataset was inverted to estimate a slip model. We repeated the simulation 1000 times and estimated the uncertainty of the inverted slip distribution based on the RMS scatter of the resulting models (Figure 4.20). We see up to 0.9 m of scatter in the

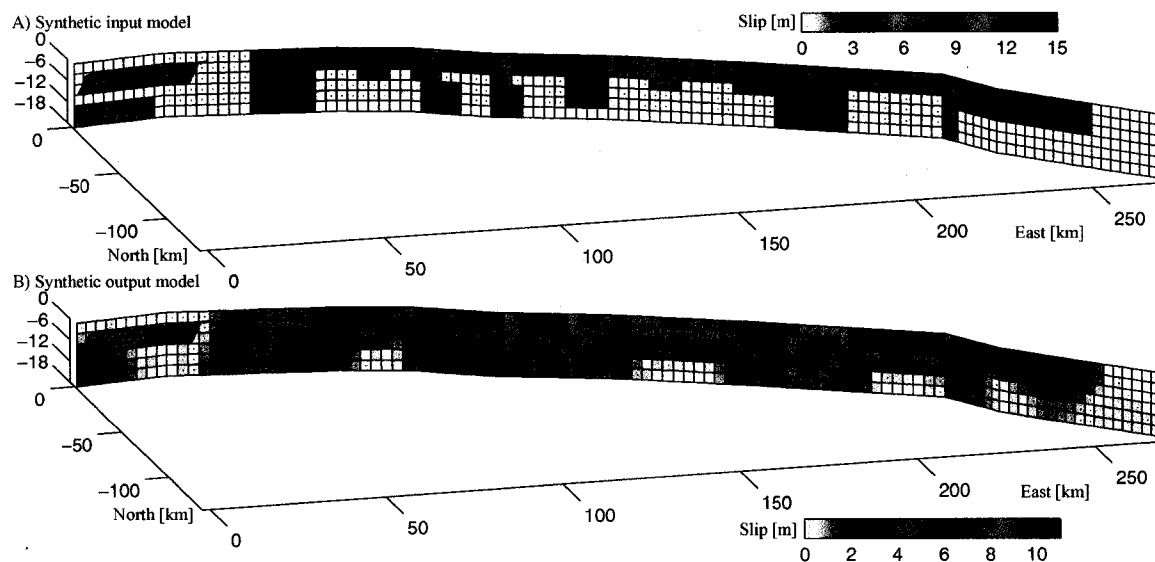


Figure 4.19. Inversion result from a synthetic dataset calculated using a simple synthetic model. The resulting model of slip distribution closely resembles that estimated from the measured coseismic GPS and surface offset dataset.

estimated slip on individual tiles. The highest uncertainty is along the surface, reflecting the high uncertainty of the surface offset data (0.5 to 2 m uncertainty after downweighting), and also along the fault edges. We also see high uncertainty along the bottom tiles of the Denali and Totschunda faults where we have the poorest GPS coverage, e.g. below the Susitna Glacier fault, about 50 km west of the Denali-Totschunda fault junction and on the easternmost portion of the Totschunda fault. We see very low uncertainty in regions where we have near-fault GPS data, in particular around where the Trans-Alaska pipeline crosses the fault. Notably, we see low uncertainty at tiles where we estimated no slip in the inversion of the real data. This uncertainty is due purely to random errors in the data, and does not include the effect of uncertainty in the optimal smoothing or the impact of poor resolution in parts of the model.

#### 4.6 Discussion

The estimated coseismic slip model of the Denali Fault earthquake is a great improvement from the coseismic model presented by *Hreinsdóttir et al.* [2003], which was based on a much smaller dataset. The large number of additional GPS sites presented here results in

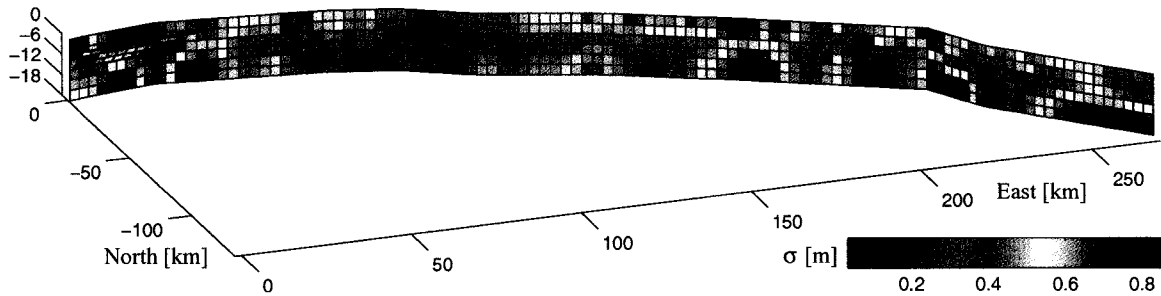


Figure 4.20. Estimated uncertainty of the coseismic slip distribution using a Monte Carlo simulation. We added noise to the synthetic dataset consistent with the data covariance and inverted to estimate a slip model. By iterating this process 1000 times we estimated the slip uncertainty,  $\sigma$ , for each fault tile based on the RMS scatter of the estimated slip.

greatly improved model resolution along the entire earthquake rupture. The addition of geologic surface offset data also adds valuable information at shallow depth.

We estimate a total moment of  $6.81 \times 10^{20}$  Nm assuming a rigidity of 30 GPa, giving a average moment release of  $2.0 \times 10^{18}$  Nm/km along strike (Figure 4.21). This is comparable to other estimates by the Harvard CMT solution ( $7.5 \times 10^{20}$  Nm), *Wright et al.* [2004] ( $7.6 \times 10^{20}$  Nm), *Oglesby et al.* [2004] ( $7.5 \times 10^{20}$  Nm), and *Frankel* [2004] ( $6.8 \times 10^{20}$  Nm). The moment varies considerably along strike (Figure 4.21). We see four major pulses of moment along the Denali Fault at 85, 105, and 130 km east of the epicenter (2a, 2b, and 2c) and the largest moment pulse about 40 km west of the Denali-Totschunda fault junction (3). We identify lower than average moment along the Denali fault for the first 30 km east of the epicenter and along the Totschunda fault. Our coseismic slip distribution shows significant variation in the slip rake along the Denali fault, consistent with north-side up dip-slip.

In general the slip model shows the same general features as other slip models estimated both from geodetic and/or seismic data (e.g. models of *Frankel* [2004], *Hreinsdóttir et al.* [2003], *Ji et al.* [2004], *Kikuchi and Yamanaka* [2002], *Oglesby et al.* [2004], *Ozacar et al.*, [2003], *Tsuboi et al.* [2003], and *Wright et al.* [2004]). All models identify at least two main subevents, an initial thrust event on the Susitna Glacier fault, and a larger strike-slip event on the Denali fault about 40 km west of the Denali-Totschunda fault junction, with slip at or exceeding 9 m in all models. This subevent corresponds to where the largest surface offset of 8.8 m was measured [*Haessler et al.*, 2004]. Models which are estimated using regional geodetic and/or seismic data find an additional strike-slip subevent along the

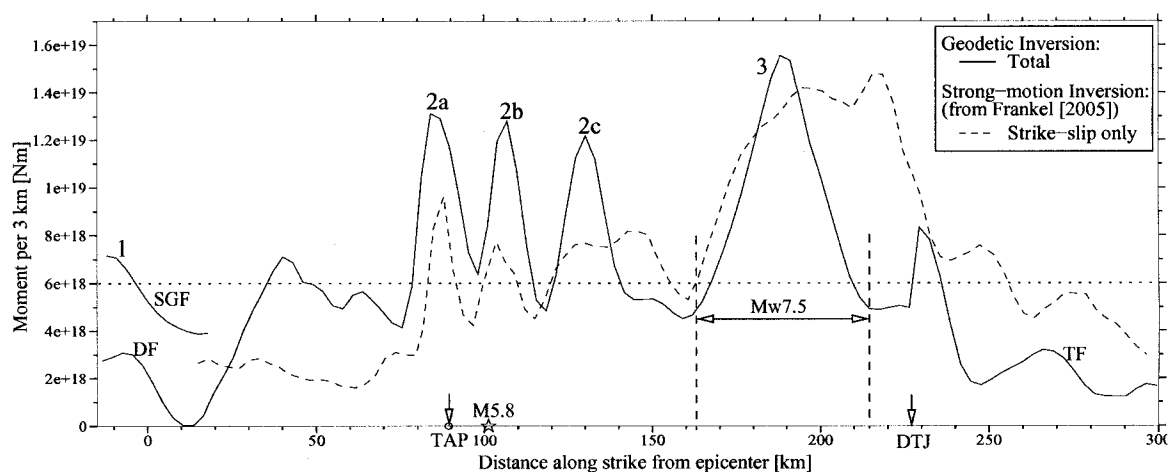


Figure 4.21. Moment release per 3 km section along the earthquake rupture. The solid black line shows the total moment release per 3 km along the earthquake rupture, estimated from inversion of GPS and surface offset data (assuming rigidity of 30 GPa). The dotted line shows the average moment release along the fault ( $6.0 \times 10^{18}$  Nm per 3 km). We identify 4 major pulses of moment release along the Denali fault. We resolve three pulses (2a, 2b, 2c) in the region previously identified as subevent 2 by others (e.g. *Eberhart-Phillips et al.* [2003]). The fourth and the largest subevent (3) equals an event with moment magnitude of  $M_W$  7.5. For reference we show with dashed line the moment release per 3 km estimated from strong-motion inversion [*Frankel, 2004*] showing the same general pattern of moment release but varying in magnitude.



Denali fault near the Trans-Alaska pipeline crossing [Eberhart-Phillips *et al.*, 2003; Frankel, 2004; Hreinsdóttir *et al.*, 2003; Wright *et al.*, 2004; Dreger *et al.*, 2004; Oglesby *et al.*, 2004]. The two subevents on the Denali fault have been identified as subevents 2 (TAP crossing) and 3 (40 km west of the Denali-Totschunda fault junction) respectively, following the initial thrust event (subevent 1) on the Susitna Glacier fault [Eberhart-Phillips *et al.*, 2003]. Studies by Wright *et al.* [2004], Dreger *et al.* [2004], and Oglesby *et al.* [2004] all rely on the smaller set of GPS data from Hreinsdóttir *et al.* [2003] to estimate slip in their model but the strong motion inversion of Frankel [2004] is independent of other data sets.

The GPS data presented here have exceptional data coverage where regional models have identified subevent 2 (near the TAP crossing). We estimate highly variable slip in that region (DF4 and DF5, Figure 4.13) and can identify 3 major pulses of moment release 80 to 140 km from the epicenter, all exceeding  $1.0 \times 10^{19}$  Nm per 3 km (2a, 2b, 2c, Figure 4.21). This is a geometrically complex region of the fault with two prominent bends in the observed surface rupture at about 80 (right or releasing bend) and 100 km (left or restraining bend). In addition, two major faults branch off the Denali fault towards the SW and NW between the two bends. The aftershock distribution is also highly variable, with a pocket of activity occurring between 60 and 80 km (DF3), little or no aftershock activity occurring between the two bends from 80 to 100 km (DF4) where we observe the first moment pulse, but highly energetic aftershock activity occurring east of 100 km, where the largest aftershock from the Denali Fault earthquake occurred ( $M5.8$ ). The pre-earthquake stress field reveals a significant change from NW-SE compression in the epicentral region to N-S compression just west of this region, with compressive stress being almost normal to the fault in sections DF4, DF5 and DF6 [Ratchkovski *et al.*, 2004]. The moment pulse 2a occurs east of the first prominent releasing bend in the fault (80 km) where the fault strike is more favorable for shear rupture relative to the regional stress field (at a shallower angle to the maximum compressive stress). We estimate a jump in slip at depth from 0 to 10 m across the bend over only 15 km along-strike of the fault. Ellsworth *et al.* [2004] showed that super-shear rupture velocity probably occurred on this section of the fault. Tests with synthetic data suggest that model resolution in this region is good. We suggest that this jump in slip is real and results from the releasing bend and its corresponding decrease in normal stress and/or increase in shear stress. It is also possible that this large slip pulse might be connected with

the transition to super-shear rupture. We see a similar jump in slip where the rupture steps from the Denali to the Totschunda fault, with a high deep slip patch following a “releasing” bend of the fault rupture. These two releasing bends feature the only two patches of large deep slip where there is not a corresponding shallow slip patch.

The moment pulses 2b and 2c occur east of the left or restraining bend and coincide with a zone of highly energetic aftershock activity that extends over a wide region both north and south of the fault. The moment pulse 2b is located just east of where the largest aftershock ( $M_{5.8}$ ) occurred on the fault. Moment tensor solutions for aftershocks in the area show predominantly thrust events [Ratchkovski *et al.* 2004], which suggests triggering on neighboring thrust faults in this region. In 1996 an  $M_W$  5.8 earthquake occurred in this region, a few km north of the fault, with focal mechanism and aftershocks indicative of a compressional regime in the area [Ratchkovski and Hansen, 2002].

We compare our results to that of strong motion inversion from Frankel [2004], which provides estimates totally independent of any geodetic data. Frankel [2004] inverted data from 11 strong-motion instruments, one of which is located just 3 km north of the Trans-Alaska pipeline crossing. His inversion reveals a similar pattern of moment release along the fault (Figure 4.21, dashed line); high moment release (exceeding  $1.4 \times 10^{19}$  Nm per 3 km) just west of the Denali-Totschunda fault junction (subevent 3), highly variable moment release, with 3 main pulses about 80-140 km east of the epicenter (2a, 2b, and 2c), and relatively low moment release along the Denali fault in the epicentral region and along the Totschunda fault. The pattern of moment release for the two data inversions is in best agreement where both have the best resolution, near the Trans-Alaska pipeline crossing. Strong motion inversion not including the site closest to the fault results in much broader moment release pattern with lower peak moment release [Frankel, 2004].

The majority of the estimated moment release occurs at 0-9 km depth, which agrees with the estimated depth range for the majority of aftershocks [Ratchkovski *et al.*, 2004]. Previous studies of several strong earthquakes ( $M$  6.0-6.9) e.g. on the San Andreas fault system and in the South Iceland seismic zone have shown correlation between areas of high slip and areas of low aftershock activity, and clusters of aftershocks around the edges of the high slip patches (e.g. for the 1984 Morgan Hill earthquake [Bakun *et al.*, 1986], the 1989 Loma Prieta earthquake [Beroza, 1991], and the two  $M_W$  6.5 June 2000 South Iceland

earthquakes [Pedersen *et al.*, 2003]). This has been explained e.g. in terms of local increase in shear stress in low slip regions surrounding regions with large slip and high stress drop [Bouchon, 1997]. We do not see clear relationship between slip and aftershocks for the Denali Fault earthquake though there seems to be a general concentration of aftershocks in sections DF5-DF7 where we have the lowest slip and fewer aftershocks where we have big slip patches. However both subevents 2a and 3 have significant slip to depths of 15-18 km where aftershocks are almost entirely absent and we see no clear clustering of aftershocks near the edges of the main slip patches. In contrast to what has been observed for several other large earthquakes [Rolandone *et al.*, 2004], there are very few deep aftershocks and our model finds several areas where there was significant slip much deeper than the aftershocks. The reason for the lack of deep aftershocks is not clear.

The Denali Fault earthquake has at least an order of magnitude larger rupture length than the earthquakes in above examples. Both the fault strike and the pre-earthquake stress field varies along strike and we expect other properties such as friction and pore pressure to be variable from one section of the fault to another. Thus we should not necessarily expect the number of aftershocks versus slip on one part of the fault to be the same as on another. We cannot rule out that within each section of the fault, where fault properties such as friction and pre-earthquake stress field are fairly homogenous, such a relationship exists on a finer scale. Our estimated slip distribution might be too rough and the quality of aftershock location not good enough to identify anticorrelation between the two. On the other hand we would expect slip on one segment of the fault to influence stress on other parts of the fault so such local increase in shear stress in low slip regions adjacent to high slip patches might be overprinted by the (long wavelength) total stress change on the fault.

Aftershock activity following the Denali Fault earthquake does not clearly align with the fault. The seismicity within the most active aftershock sources, within the epicentral region and along the central part of the rupture, seem to be concentrated within hanging walls of thrust structures dipping towards the main fault trace and are often several km from the Denali fault [Ratchkovski *et al.*, 2004]. This suggests stress triggering on adjacent faults rather than aftershocks on and immediately surrounding the fault plane. The same characteristics is apparent for the 1999  $M_W$  7.5 Izmit earthquake (figure 5 in Çakir *et al.* [2003]) where aftershock activity and slip distribution does not seem to be correlated and

the most active aftershock regions are offset from the main fault rupture.

The slip model presented here shows significant slip along the fault about 20-60 km from the epicenter. This region has previously been suggested as a region of low moment release by *Eberhart-Phillips et al.* [2003], *Ozacar and Beck* [2004], and *Oglesby et al.* [2004]. The lack of aftershocks in the region led *Ratchkovski et al.* [2003] to suggest that this is a creeping section of the fault. Geodetic data from the Black Rapids Glacier region (44-54 km east of the epicenter) suggest  $\sim 4$  m of slip in the region, despite the lack of aftershocks, and our preferred coseismic slip model shows 2-4 m of slip from about 30-60 km east of the epicenter, smoothly varying along strike and with depth. This suggests a significant moment release ( $\geq 1.5 \times 10^{18}$  Nm per km of fault length) from at least 30 km east of the epicenter to the Denali-Totschunda fault junction (Figure 4.21), and makes it clear that this section of the fault slipped during the earthquake.

The coseismic slip distribution shows both variation in rupture width along the fault and variation in slip with depth. The largest slip patch along the fault, subevent 3, shows high slip down to 18 km depth with the maximum slip occurring at 3-12 km depth. In contrast, sub events 2b and 2c are shallow, with the maximum slip occurring close to the surface. Sub event 2a is also deep, with significantly lower slip at the surface than at depth. In order to accurately estimate moment release we need information on both the rupture width and average slip with depth. Our results indicate that although surface offset data can give an indication of the along-strike slip distribution it alone cannot be used to accurately estimate the moment release for a complex rupture earthquake like the Denali Fault earthquake.

#### 4.7 Conclusions

We have estimated coseismic displacement for the 2002 Denali Fault earthquake at 232 GPS sites in Alaska and Canada, and use these data to study the geometry and slip distribution of the earthquake.

A dense profile of GPS data along the Richardson Hwy suggest that the Denali fault is near vertical in the region. The near fault GPS data along the highway agree with the largest observed surface offset measured in that region, but show a broad deforming zone around the fault.

We inverted the GPS data for a coseismic slip model along the Susitna Glacier, Denali,

and Totschunda faults. The large amount of data result in greatly improved model resolution along the faults. The estimated total moment release in the Denali Fault earthquake is  $6.81 \times 10^{20}$  Nm ( $M_W$  7.89) assuming rigidity of 30 GPa. The earthquake initiated with a  $M_W$  7.2 thrust sub-event on the Susitna Glacier fault but continued with highly variable, predominantly strike-slip along the Denali fault and then the Totschunda fault. We estimate a moment release of about  $5 \times 10^{18}$  Nm per 3 km from about 30 km east of the epicenter to the Denali-Totschunda fault junction. We see four larger pulses of moment release along the fault, with moment exceeding  $1 \times 10^{19}$  Nm per 3 km. The first three, subevents 2a, b, and c, are fairly narrow pulses of almost pure strike-slip motion, occurring 80-140 km east of the epicenter, but the fourth and the largest has slightly oblique slip with total moment corresponding to a  $M_W$  7.5 event. A fairly low moment release at shallow depth is estimated along the Totschunda fault. The estimated slip distribution along the surface is in very good agreement with geological surface offset measurements not measured on glaciers, but we find that surface offsets measured on glaciers are biased to lower values. The slip distribution does not show any clear correlation with aftershock activity. We see significant slip to depths of 18 km whereas the majority of aftershocks has been located in the upper 11 km of the crust. In two regions we see patches of large deep slip with no corresponding shallow slip patches, both patches follow a releasing stress bend of the fault rupture.

The GPS data presented in this paper and surface offset data along the fault rupture [Haeussler *et al.*, 2004] provide important constraints on the slip distribution along the Denali and Totschunda faults and along with available InSAR data from the epicentral region [Wright *et al.*, 2004] should play a prominent part in the understanding of the rupture processes for the geometrically complex Denali Fault earthquake.

#### 4.8 Acknowledgments

We are grateful to all data providers, from which this work truly benefits, in particular R. Scott Sexton, Alaska Department of Transportation, Fairbanks; Michael Schoder, Alaska Department of Transportation, Anchorage; Douglas A. Graether, OceanTech, Anchorage; Aeromap; Paul Flück and Michael Schmidt, Geological Survey of Canada; Martin Truffer and Sandra Zirnheld, UAF glaciology. We thank UNAVCO and Central Washington University for loaning us equipment, Purdue University and University of California Berkeley for

loaning us equipment and providing field assistance with data collection. We thank everyone who participated in various GPS campaigns following the Denali Fault earthquake, students and staff from UAF, Purdue, and UCB. In particular we would like to thank Christopher F. Larsen, A. Max Kaufman, Hilary J. Fletcher, Melany Zimmerman, Ingrid Johanson, and Arjun Aryal. We thank the Alyeska Pipeline Service Company for access to land, and privately collected survey data. Peter Haeussler, Natalia Ratchkovski, Patricia A. Craw, Arthur Frankel, Tim J. Wright for helpful discussions and providing data in advance of publication. Christopher F. Larsen, Ken Hudnut, Doug Christensen, and Steve McNutt provided comments and suggestions. This work was supported by NSF EAR-0310410, NSF EAR-0323156, and NSF EAR-0328043.

## References

- Bakun, W. H., G. C. P. King, and R. S. Cockerham (1986), Seismic slip, aseismic slip, and the mechanics of repeating earthquakes on the Calveras fault, California, In *Earthquake Source Mechanics*, AGU Geophys. Mono. 37, eds. S. Das, C. Scholz, and J Boatwright, Washington, DC, American Geophysical Union, 195-207.
- Beroza, G. C. (1991), Near-source modeling of the Loma Prieta earthquake: Evidence for heterogeneous slip and implications for earthquake hazard, *Bull. Seis. Soc. Amer.*, 81(5), 1603-1621.
- Boucher, C., Z. Altamimi, and P. Sillard (1999), The 1997 International Terrestrial Reference Frame (ITRF97), *IERS Tech. Note 27*, Int. Earth Rotation Serv., Paris.
- Boucher, M. (1997), The state of stress on some faults of the San Andreas system as inferred from near-field strong motion data, *J. Geophys. Res.*, 102(B6), 11731-11744.
- Carver, G., G. Plafker, M. Metz, L. Cluff, B. Slemmons, E. Johnson, J. Roddick, and S. Sorensen (2004), Surface Rupture on the Denali fault interpreted from tree damage during the 1912 Delta River  $M_W$  7.2-7.4 earthquake: Implications for the 2002 Denali Fault earthquake slip distribution, *Bull. Seis. Soc. Amer.*, 94(6B), S58-S71.
- Chinnery, M. A. (1965), The vertical displacements associated with transcurrent faulting, *J. Geophys. Res.*, 70(18), 4627-4632.
- Crone, A. J., S. F. Personius, P. A. Craw, P. J. Haeussler, and L. A. Staff (2004), The Susitna Glacier Thrust Fault-Characteristics of surface ruptures on the fault that initiated

- the 2002 Denali Fault earthquake, *Bull. Seis. Soc. Amer.*, *94*(6B), S5-S22.
- Çakir, Z., J. de Chabaliér, R. Armijo, B. Meyer, A. Barka, and G. Peltzer (2003), Coseismic and early post-seismic slip associated with the 1999 Izmit earthquake (Turkey), from SAR interferometry and tectonic field observations, *Geophys. J. Int.*, *155* 93-110.
- Doser, D. I. (2004), Seismicity of the Denali fault zone (1912-1988), *Bull. Seis. Soc. Amer.*, *94*(6B), S132-S144.
- Dreger, S. D., D. D. Oglesby, R. Harris, N. Ratchkovski, and R. Hansen (2004), Kinematic and dynamic rupture models of the November 3, 2002  $M_W$  7.9 Denali, Alaska, earthquake, *Gephys. Res. Lett.*, *31*(4), doi:10.1029/2003GL018333.
- Eberhart-Phillips, D., P. J. Haeussler, J. T. Freymueller, A. D. Frankel, C. M. Rubin, P. Craw, N. A. Ratchkovski, G. Anderson, A. J. Crone, T. E. Dawson, H. Fletcher, R. Hansen, E. L. Harp, R. A. Harris, D. P. Hill, S. Hreinsdóttir, R. W. Jibson, L. M. Jones, D. K. Keefer, C. F. Larsen, S. C. Moran, S. F. Personius, G. Plafker, B. Sherrod, K. Sieh, and W. K. Wallace (2003), The 2002 Denali fault earthquake, Alaska: A large magnitude, slip-partitioned event, *Science*, 1113-1118.
- Ellsworth, W. L., M. Celebi, J. R. Evans, E. G. Jensen, R. Kayen, M. C. Metz, D. J. Nyman, J. W. Roddick, P. Spudich, and C. D. Stephens (2004), Near-field ground motion of the 2002 Denali Fault, Alaska, earthquake recorded at Pump station 10, *Earthquake Spectra*, *20*(3), 597-615.
- Fletcher, H. J. (2002), Tectonics of interior Alaska from GPS measurements, Ph.D. thesis, 257 pp., Univ. Alaska Fairbanks, Fairbanks, Alaska.
- Fletcher, H. J., and J. T. Freymueller (2003), New constraints on the motion of the Fair-weather fault, Alaska, from GPS observations, *Gephys. Res. Lett.*, *30*(3), doi:10.1029/2002GL016476.
- Frankel, A. (2004), Rupture process of the M7.9 Denali Fault, Alaska, earthquake: Sub-events, directivity, and scaling of high-frequency ground motions, *Bull. Seis. Soc. Amer.*, *94*(6B), S234-S255.
- Freymueller, J. T, S. C. Cohen, and H. J. Fletcher (2000), Spatial variations in present-day deformation, Kenai Peninsula, Alaska, and their implications, *J. Geophys. Res.*, *105*(B4), 8079-8102.
- Haeussler, P. J., D. P. Schwartz, T. E. Dawson, H. D. Stenner, J. J. Lienkaemper, B. Sher-

- rod, F. R. Cinti, P. Montone, P. Craw, A. J. Crone, and S. Personius (2004), Surface rupture and slip distribution of the Denali and Totschunda faults in the November 3, 2002 M7.9 earthquake, Alaska, *Bull. Seis. Soc. Amer.*, *94*(6B), S23-S52.
- Hearn, E. H., and R. Bürgmann (submitted 2004), The effect of elastic layering on inversions of GPS data for earthquake slip and resulting stress changes, submitted to *Bull. Seis. Soc. Amer.*,
- Heinrichs, T. A., L. R. Mayo, D. C. Trabant, and R. S. March (1995), Observations of the surge-type Black Rapids glacier, Alaska, during a quiescent period, 1970-92, U. S. Geological Survey, Open-File Report 94-512, Fairbanks, Alaska.
- Heinrichs, T. A. (1994), Quiescent phase evolution of a surge-type glacier: Black Rapids Glacier, Alaska, USA, M.S. thesis, University of Alaska Fairbanks.
- Hreinsdóttir, S., J. T. Freymueller, H. J. Fletcher, C. F. Larsen, and R. Bürgmann (2003), Coseismic slip distribution of the 2002  $M_W$  7.9 Denali fault earthquake, Alaska, determined from GPS measurements, *Gephys. Res. Lett.*, *30*(13), doi:10.1029/2003GL017447.
- Ji, C., D. V. Helmberger, and D. J. Wald (2004), A teleseismic study of the 2002 Denali fault, Alaska, earthquake and implications of rapid strong-motion estimation, *Earthquake Spectra*, *20*(3), 617-637.
- Kikuchi, M., and Y. Yamanaka (2002), Source rupture processes of the central Alaska earthquake of Nov. 3, 2002, inferred from teleseismic body waves (+ the 10/23 M6.7 event), EIC seismological note - No. 129, Earthquake Research Institute (ERI), Univ. Tokyo, Tokyo.
- Lahr, J. C., and G. Plafker (1980), Holocene Pacific-North American plate interaction in southern Alaska: Implications for the Yakataga seismic gap, *Geology*, *8*, 483-486.
- Matthews, M., and P. Segall (1993), Statistical inversion of crustal deformation data and estimation of the depth distribution of slip in the 1906 earthquake, *J. Geophys. Res.*, *98*(B7), 12153-12163.
- Oglesby, D. D., D. S. Dreger, R. A. Harris, N. Ratchkovski, and Roger Hansen (2004), Inverse kinematic and forward dynamic models of the 2002 Denali, Alaska earthquake, *Bull. Seis. Soc. Amer.*, *94*(6B), S214-S233.
- Okada, Y. (1985), Surface deformation due to shear and tensile faults in a halfspace, *Bull. Seis. Soc. Amer.*, *75*(4), 1135-1154.



- Ozacar, A. A., and S. L. Beck (2004), The 2002 Denali Fault and 2001 Kunlun Fault earthquakes: complex rupture processes of two large strike-slip events, *Bull. Seis. Soc. Amer.*, *94*(6B), S278-S292.
- Ozacar, A. A., S. L. Beck, D. H. Christensen (2003), Source process of the 3 November 2002 Denali fault earthquake (central Alaska) from teleseismic observations, *Gephys. Res. Lett.*, *30*(12), doi:10.1029/2003GL017272.
- Page, R., and J. Lahr (1971), Measurements for fault slip on the Denali, Fairweather, and Castle mountain faults, Alaska, *J. Geophys. Res.*, *76*(35).
- Page, R. A. (1972), Crustal deformation on the Denali fault, Alaska, 1942-1970, *J. Geophys. Res.*, *77*(8).
- Page, R. A., N. N. Biswas, J. C. Lahr, and H. Pulpan (1991), Seismicity of continental Alaska, in *Neotectonics of North America*, edited by D. B. Slemmons, E. R. Engdahl, M. D. Zoback, D. D. Blackwell, The Geological Society of America, Inc.
- Pedersen, R., S. Jónsson, T. Árnadóttir, F. Sigmundsson, and K. L. Feigl (2003), Fault slip distribution of two June 2000  $M_W$  6.5 earthquakes in South Iceland estimated from joint inversion of InSAR and GPS measurements, *Earth Planet. Sci. Lett.*, *213*, 487-502.
- Plafker, G., and H. C. Berg (1994), Overview of the geology and tectonic evolution of Alaska, in *The Geology of North America, Decade of North American Geology*, vol. G-1, edited by G. Plafker and H. C. Berg, Geol. Soc. Amer., Boulder, Colorado.
- Plafker, G., L. Gilpin, and J. Lahr (1994), Neotectonic map of Alaska, Map in *The Geology of North America, Decade of North American Geology*, vol. G-1, edited by G. Plafker and H. C. Berg, Geol. Soc. Amer., Boulder, Colorado.
- Plafker, G., G. Carver, M. Metz, and L. Cluff (2004), Repeated historic surface ruptures of the Denali fault at Delta river, Alaska during large earthquakes in 1912 and 2002, *Eos Trans. AGU*, *85*(47), Fall Meet. Suppl., Abstract G11A-0780.
- Price, E. J., and R. Bürgmann, Interactions between the Landers and Hector Mine, California, earthquakes from space geodesy, boundary element modeling and time-dependent friction, *Bull. Seis. Soc. Amer.*, *92*(4), 1450-1469.
- Ratchkovski, N. A., and R. A. Hansen (2002), New constraints on tectonics of interior Alaska: Earthquake locations, source mechanisms, and stress regime, *Bull. Seis. Soc. Amer.*, *92*(3), 998-1014.

- Ratchkovski, N. A., R. A. Hansen, J. C. Stachnik, T. Cox, O. Fox, L. Rao, E. Clark, M. Lafevers, S. Estes, J. B. MacCormack, and T. Williams (2003), Aftershock sequence of the  $M_W$  7.9 Denali fault, Alaska, earthquake of 3 November, 2002 from the regional seismic network data, *Seis. Res. Lett.*, *74*(6), 743-752.
- Ratchkovski, N. A., S. Wiemer, and R. A. Hansen (2004), Seismotectonics of the central Denali fault, Alaska and the 2002 Denali fault earthquake sequence, *Bull. Seis. Soc. Amer.*, *94*(6B), S156-S174.
- Rolandone, F., R. Bürgmann, and R. M. Nadeau (2004), The evolution of the seismic-aseismic transition during the earthquake cycle: Constraints from the time-dependent depth distribution of aftershocks, *Gephys. Res. Lett.*, *31*, L23610, doi:10.1029/2004-GL021379.
- Savage, J. C. and M. Lisowski (1991), Strain accumulation along the Denali fault at the Nenana river and Delta river crossing, Alaska, *J. Geophys. Res.*, *96*(B9).
- Stark, P. B., and R. L. Parker (1995), Bounded-variable least-squares: An algorithm and application, *Comput. Stat.*, *10*(2), 129-141.
- Tsuboi, S., D. Komatitsch, C. Ji, and J. Tromp (2003), Broadband modeling of the 2002 Denali fault earthquake on the Earth Simulator, *Phys. Earth Planet. Inter.*, *139*(3-4), 305-313.
- Wessel, P., and W. H. F. Smith (1998), New improved version of the Generic Mapping Tools released, *Eos Trans. AGU*, *79*(47), 574.
- Wright, T. J., Z. Lu, and C. Wicks (2003), Source model for the  $M_W$  6.7, 23 October 2002, Nenana Mountain Earthquake (Alaska) from InSAR, *Gephys. Res. Lett.*, *30*(18), 1974, doi:10.1029/2003GL018014.
- Wright, T. J., Z. Lu, and C. Wicks (2004), Constraining the slip distribution and fault geometry of the  $M_W$  7.9, 3 November 2002, Denali fault earthquake with InSAR and GPS, *Bull. Seis. Soc. Amer.*, *94*(6B), S175-S189.

## Chapter 5

### Conclusions

#### 5.1 General

In this thesis I have presented coseismic GPS data from two major earthquakes. The earthquakes are quite different. The January  $M_W$  7.7 earthquake, off the coast of El Salvador, occurred in the subducting Cocos plate with a normal faulting mechanism. The  $M_W$  7.9 Denali Fault earthquake, in the interior of Alaska, ruptured the surface along a major continental strike-slip fault. The number of GPS sites with discernible coseismic signal is drastically different, which means that different questions can be addressed in the two cases. There are only a handful of continuous GPS stations in Central America, all with less than 20 mm coseismic displacement. In Alaska we have a large number of GPS sites with coseismic displacements from a few mm to over 3 m. As a result the emphasis of the papers is quite different. In El Salvador, where we have no fault rupture at the surface, we have used the GPS data to estimate both slip on and location of a fixed fault plane using a forward modeling scheme. In Alaska, where we know the location of the fault at the surface, we have estimated the detailed slip distribution by inverting the GPS data. In both cases our results compare well with the location and dynamic modeling from seismic data. The results and conclusions of each study have been presented in detail within each chapter. Here we summarize the main findings.

#### 5.2 The 2001 El Salvador Earthquakes

Coseismic displacements of up to 15 mm were observed from the January 13  $M_W$  7.7 El Salvador earthquake at continuous GPS stations in Central America. The measured displacements allow us to estimate both the earthquake location and moment, using information from seismology to constrain the fault's dimensions. Coulomb stress changes estimated from the coseismic model suggest that the  $M_W$  6.6 El Salvador earthquake (occurring one month later) was triggered by the  $M_W$  7.7 earthquake. The February 13  $M_W$  6.6 earthquake was a strike-slip event occurring in the overriding Caribbean plate, within a tectonic depression along the volcanic arc. Coseismic displacement of  $\sim 40$  mm at a GPS station in San Salvador suggests that the earthquake triggered additional slip on a fault close to the GPS station. The  $M_W$  6.6 earthquake further changed the static stress in the upper crust,

triggering slip on multiple parallel faults west and possibly east of the epicenter in the days to months following the earthquake. We suggest from the distribution of triggered events and aftershock locations that bookshelf style deformation at least partly accommodates deformation along the tectonic depression.

### 5.3 The 2002 Denali Fault Earthquake

The Denali Fault earthquake ruptured the surface along three faults in Alaska, the Susitna Glacier, Denali, and Totschunda faults. In the two weeks following the earthquake 28 campaign GPS sites were measured around the fault in addition to 12 continuously operating GPS stations in Alaska. The GPS data suggested a complex coseismic rupture along the faults. The site distribution was less than ideal and we had limited resolution on large sections of the faults. However inversion of the data identified two main regions of moment release along the Denali fault and suggested that slip on the Totschunda fault was only shallow. These results have been supported by the analysis of seismic data.

In the year following the earthquake a large number of additional sites was measured around the fault, including sites previously measured only by land surveyors. Coseismic displacements have been estimated for the earthquake at over 200 GPS sites in Alaska and Canada. The additional data have drastically improved resolution on the faults and have given important insights to the fault rupture. We estimate a total moment release of  $6.81 \times 10^{20}$  Nm ( $M_W$  7.89) in the earthquake which compares well with seismic studies.

The GPS data reveal a complex slip pattern along the earthquake rupture. In the epicentral region, predominantly thrust motion is estimated along the Susitna Glacier fault, with total moment equivalent to a  $M_W$  7.2 subevent. The earthquake then ruptured the Denali and Totschunda faults unilaterally from west to east with predominantly right-lateral strike-slip motion. We estimate at least  $2 \times 10^{18}$  Nm/km moment release from about 30 km east of the epicenter to the Denali-Totschunda fault junction but relatively low and shallow slip is estimated along the Totschunda fault. Slip along the Denali fault is highly variable, with four main pulses of moment release. The largest moment pulse, a slip patch corresponding to a  $M_W$  7.5 subevent, occurred about 40 km west of the Denali-Totschunda fault junction with slip of  $\sim 9$  m. The GPS data suggest two patches of deep slip, both coinciding with complex fault geometry and following a right bend in the

earthquake rupture. This could be a result of the fault strike becoming more favorable for shear rupture relative to the regional stress field. The slip distribution does not suggest a clear anticorrelation with aftershock activity. We estimate significant slip down to 18 km depth but the majority of aftershocks have been located in the upper 11 km of the crust. Our results compare well with results from strong motion inversions, giving similar patterns of moment release though the details differ.

The study from the Denali Fault earthquake shows the power of GPS when the site distribution and density is good. We ran resolution tests for the slip model which suggests that along the Denali and Totschunda faults we can resolve slip along the entire fault rupture. The resolution is best where the data density is the greatest. The lack of sites near and north of the Susitna Glacier fault does not allow us to estimate a detailed slip distribution and we need to rely on both geological and seismic data for the fault geometry with depth. However our estimate of moment release on the thrust fault compares well with other studies. Around the Trans-Alaska pipeline crossing, where the site density is the greatest, we have good resolution along the fault. The data suggest a near vertical fault rupture with predominantly right-lateral strike-slip motion but a significant component of reverse faulting, north-side up.

The GPS data from the Denali Fault earthquake support findings from other studies, from geological surface offsets, InSAR, teleseismic, and strong motion data, but reveal more details of the slip-distribution than other datasets alone. The GPS data can further compliment other datasets in future studies to estimate more detailed kinematic and dynamic slip models for the earthquake.

#### **5.4 Future of Earthquake Research with GPS**

Geodetic studies of coseismic deformation rely on data that exist prior to the earthquake. We cannot yet predict when and where a large earthquake is going to occur. Each year new continuous GPS sites are installed around the world and new or improved geodetic networks are measured. In addition GPS is becoming more and more popular for surveying. The study presented in this thesis has benefited from these efforts. Without the continuous GPS stations in Central America we would not have been able to estimate the coseismic displacements. Following the Denali Fault earthquake the large number of sites surveyed

prior to the earthquake resulted in one of the most detailed study of coseismic slip pattern with geodetic data to date. With projects such as the Plate Boundary Observatory (PBO) in the United States our chances of measuring deformation from the next large earthquake is increased. A major goal of the PBO project is to install and operate continuous GPS stations in and around the plate boundary zone between the Pacific and North American plates to study active deformation. The example from the Denali Fault earthquake has shown what GPS is capable of when the number and site density is good or optimal. With PBO the site density and data quality will exceed what we currently have available and we should expect to see more detailed slip models of future earthquakes than anything prior to now. With more data and improved slip models we will hopefully further enhance our understanding of earthquakes.

## Appendix A

### Table with Chapter 3

This appendix contains coseismic displacements estimated for the Denali Fault earthquake in Chapter 3. The table is an online supplement to the paper which has been published in *Geophysical Research Letters*.

Table A.1: Coseismic GPS data for the Denali Fault earthquake.

SITE	Location		Displacement			Uncertainty		
	Lat. [°]	Lon. [°]	N [m]	E [m]	V [m]	$\sigma_N$ [m]	$\sigma_E$ [m]	$\sigma_V$ [m]
SELD	59.4457	-151.7067	-0.0019	-0.0013	0.0054	0.0065	0.0054	0.0093
UAMF	60.0985	-149.4424	-0.0097	-0.0091	-0.0125	0.0091	0.0041	0.0062
CHI4	60.2377	-146.6465	0.0121	-0.0012	0.0053	0.0085	0.0045	0.0172
TRLK	60.5015	-149.4203	-0.0064	-0.0077	0.0170	0.0032	0.0056	0.0217
NIK2	60.6853	-151.3915	-0.0048	-0.0068	-0.0052	0.0018	0.0220	0.0579
MPEN	60.7352	-150.4827	-0.0137	-0.0135	-0.0068	0.0116	0.0057	0.0072
TURN	60.9305	-149.5433	-0.0106	-0.0107	-0.0220	0.0044	0.0027	0.0206
NSLM	60.9927	-138.4965	0.0062	-0.0041	0.0314	0.0042	0.0046	0.0052
POT3	61.0563	-146.6968	0.0146	-0.0134	0.0279	0.0064	0.0056	0.0098
ANC1	61.1824	-149.9968	-0.0052	-0.0140	0.0022	0.0064	0.0054	0.0095
TSEA	61.1873	-149.8950	-0.0049	-0.0167	0.0025	0.0064	0.0054	0.0095
DEST	61.2169	-138.7219	0.0063	-0.0034	0.0088	0.0032	0.0041	0.0131
ATW2	61.5977	-149.1322	-0.0074	-0.0256	-0.0002	0.0064	0.0055	0.0096
TAZL	62.0799	-145.4339	0.1008	-0.0582	0.0538	0.0029	0.0097	0.0062
GNAA	62.1124	-145.9702	0.0496	-0.0527	0.0208	0.0085	0.0097	0.0158
TLKA	62.3077	-150.4203	-0.0134	-0.0250	-0.0372	0.0085	0.0098	0.0159
7297	62.6880	-145.4261	0.1642	-0.2682	-0.0123	0.0029	0.0064	0.0125
MEN	62.9095	-143.7953	2.1467	-2.2479	-0.2459	0.0043	0.0046	0.0070
PAXS	62.9673	-145.4517	0.2720	-0.6130	-0.0615	0.0057	0.0050	0.0071
LOG	63.0226	-143.3454	-0.0786	1.1241	0.0815	0.0065	0.0158	0.0404
FCRK	63.0907	-145.4753	0.3866	-0.9192	-0.0729	0.0041	0.0074	0.0070
DH97	63.2651	-147.8551	0.0073	-0.1947	-0.0519	0.0063	0.0055	0.0098
M110	63.3055	-148.1870	-0.0669	-0.1617	-0.0316	0.0063	0.0055	0.0098
STRI	63.3334	-142.9531	0.0138	0.2972	-0.0294	0.0051	0.0108	0.0056
SSWB	63.3413	-149.0902	-0.0228	-0.0609	0.0090	0.0068	0.0063	0.0110
L2C6	63.3828	-148.8662	-0.0269	-0.0601	-0.0109	0.0063	0.0055	0.0097
CGLO	63.3883	-148.9496	-0.0170	-0.0655	-0.0110	0.0066	0.0059	0.0111
R109	63.3953	-148.6468	-0.0339	-0.0788	-0.0120	0.0067	0.0059	0.0104
HIW4	63.4643	-148.8073	-0.0323	-0.0431	-0.0159	0.0063	0.0056	0.0098
PANA	63.4838	-148.8204	-0.0308	-0.0454	-0.0169	0.0068	0.0061	0.0109
ATT	63.5025	-145.8472	-0.7493	1.3025	-0.0032	0.0085	0.0135	0.0156
0999	63.6650	-142.2748	0.0071	0.1307	-0.0463	0.0045	0.0061	0.0068
DNLY	63.6951	-145.8876	-0.3945	0.4763	0.0187	0.0077	0.0184	0.0060
GRNR	63.8358	-148.9783	-0.0467	0.0334	0.0188	0.0063	0.0056	0.0098

Table A.1: Coseismic GPS data for the Denali Fault earthquake.

SITE	Location		Displacement			Uncertainty		
	Lat. [°]	Lon. [°]	N [m]	E [m]	V [m]	$\sigma_N$ [m]	$\sigma_E$ [m]	$\sigma_V$ [m]
BSB4	63.9065	-145.7891	-0.2280	0.1855	0.0247	0.0130	0.0212	0.0418
2999	64.0287	-142.0761	0.0418	0.1143	0.0385	0.0029	0.0037	0.0076
NENA	64.5794	-149.0798	-0.0248	0.0382	0.0443	0.0082	0.0131	0.0117
CLGO	64.8738	-147.8605	-0.0514	0.0244	0.0188	0.0062	0.0056	0.0100
FAIR	64.9780	-147.4992	-0.0516	0.0248	0.0233	0.0063	0.0057	0.0101
CENA	65.4982	-144.6776	-0.0378	0.0183	0.0257	0.0088	0.0102	0.0159



## **Appendix B**

### **Tables With Chapter 4**

This appendix contains all Tables referred to in Chapter 4 but which due to length were submitted as online supplement with the paper. The first table, Table B.1, contains information on GPS stations used in the study and surveys. It has been slightly modified to fit the UAF thesis format. Table B.2 contains the coseismic displacements estimated for the Nenana Mt. earthquake. Table B.3 contains interseismic, postseismic, and Nenana Mt. earthquake corrections applied to the data. Table B.4 contains the coseismic displacements estimated for the Denali Fault earthquake.

Table B.1: GPS stations and surveys

SITE	Survey Marker Inscription (Name)	Pre-Earthquake Data		Post Earthquake Data		
		First/Last	Institute(s)	Nenana	Denali	Institute(s)
0999	0999	1999/2000	UAF		07NOV02	UAF
126G	(126)	1994	ADOT		18JUN03	UAF/UCB/PU
2201	60655 1983	1998/2002	CMJV/UAF		30AUG03	UAF
2999	2999	1999/2000	UAF		07NOV02	UAF
7297	7297 AUG 91	1993/2000	NASA/UAF		07NOV02	UAF
8130	848130	2000/2002	GSC/PGC		18NOV02	GSC/PGC
AL23	A 123 1965	2002	CMJV		13JUN03	UAF/UCB/PU
ALAS	ALASKA 2 1964	1997/2002	UAF		02JUL03	UAF
ANC1	(ANCHORAGE INT AIRPORT)	Permanent 2001	ADOT		03NOV02	ADOT
ATT	ATT 1999	1999/2002	UAF		04NOV02	UAF
ATW2	(ATWC PALMER)	Permanent 2000	UAF		03NOV02	UAF
B122	B 122 1965	2002	CMJV		16JUN03	UAF/UCB/PU
B123	B 123 1965	2002	CMJV		13JUN03	UAF/UCB/PU
B124	B 124 1965	2002	UAF	28OCT02	13MAY03	UAF/UCB/PU
BEAR	BEAR MT 1997	1997/2002	UAF		30JUN03	UAF
BRAD	BRAD 1998	1998/2002	UAF		29AUG03	UAF
BRBA	(WILLS EAR LOWER)	2002	UAF		03MAY03	UAF
BREM	(BREMNER SEISMIC)	2000/2002	UAF		09JUL03	UAF
BRLA	(LAKE)	(1973)/1993	(USGS)/UAF		03MAY03	UAF
BROZ	(OZONE)	(1973)	(USGS)		04MAY03	UAF
BRPO	(POTHOLES)	(1973)	(USGS)		04MAY03	UAF
BRSR	(SHUDDER)	(1973)	(USGS)		08MAY03	UAF
BRWE	(WILLS EAR)	(1973)/1993	(USGS)/UAF		04MAY03	UAF
BRWN	(BROWNE)	1998/2002	UAF		10NOV02	UCB
BSB4	BEALES S. BASE NO 4 1942	1997/2002	UAF		04NOV02	UAF
BUMP	GPS NO BUMP 1990	1994	CMJV		14JUN03	UAF/UCB/PU
C122	C 122 1965	2002	CMJV		29MAY03	UAF/UCB/PU
C123	C 123 1965	1994/2002	ADOT/CMJV		13JUN03	UAF/UCB/PU
C96	C 96 1964	2002	ADOT		16JUN03	UAF/UCB/PU

Table B.1: GPS stations and surveys

SITE	Survey Marker Inscription (Name)	Pre-Earthquake Data		Post Earthquake Data		
		First/Last	Institute(s)	Nenana	Denali	Institute(s)
CARL	CARL 1997	1997/2000	UAF		04JUN03	UAF/UCB/PU
CC	5151A 2000	2000/2002	LCMF/UAF		16SEP03	UAF
CENA	(CENTRAL NOAA FSL)	Permanent 1997	NOAA		03NOV02	NOAA
CGLO	T17S R7W 1986 1993	1994/2000	ADOT/CMJV/UAF	24OCT02	04NOV02	UAF
CHI4	(CAPE HINCHINBROOK 4)	Permanent 1999	USCG		05NOV02	USCG
CKLN	(CHICKALOON)	2000/2002	UAF		05JUL03	UAF
CLGO	(COLLEGE OBSERV)	Permanent 1996	UAF		03NOV02	UAF
CMJV	(CRAZY MTS JOINT VENTURE)	Permanent 1998	CMJV		03NOV02	CMJV
COGH	COGHILL 1947	1992/2002	NOAA/UAF		13JUL03	UAF
COMB	COMB 1983	1992/1999	NOAA/UAF		01AUG03	UAF
CPLK	(COOPER LAKE)	1999/2002	UAF		30JUN03	UAF
CPR	CPR 95	1995/2002	UAF		13NOV02	UCB
CRK1	GPS CREEK 1 2003*	2002	ADOT		07NOV03	UAF
CRK2	GPS CREEK 2 2003*	2002	ADOT		07NOV03	UAF
D122	D 122 1965	2002	CMJV		30MAY03	UAF/UCB/PU
DAHL	DAHL 1964	1996/2002	UAF		30JUN03	UAF
DEST	DESTRUCTION 1943	1999/2002	UAF/GSC/PGC		13NOV02	GSC/PGC
DFLY	DFLY 1997	1997/2002	UAF	28OCT03	12NOV02	UAF
DH97	DH97 1997	1997/2000	UAF	24OCT02	03NOV02	UAF
DIAN	DIANA 1991	1997/2002	UAF		25AUG03	UAF
DIXI	DIXIE 1949	1992/2002	NOAA/UAF		13JUL03	UAF
DNLY	DNLY 1997	1997/2002	UAF		04NOV02	UAF
E113	E 113 1965	2002	CMJV		29MAY03	UAF/UCB/PU
E175	E 175 WASH DC	2002	ADOT		25MAY03	UAF/UCB/PU
EFRK	(EAST FORK TOKLAT)	2002	UAF		28JUL03	UAF
EAGL	EAGLE GPS	1993/2002	USGS/UAF		23SEP03	USGS
EGG	EGG 1912	1992/2002	NOAA/UAF		13JUL03	UAF
EGL2	EAGLE 1997	1997/2000	UAF		03JUN03	UAF/UCB/PU
EKG3	EAST KALGIN 3 1976	1999/2002	UAF		25JUN03	UAF

Table B.1: GPS stations and surveys

SITE	Survey Marker Inscription (Name)	Pre-Earthquake Data		Post Earthquake Data		
		First/Last	Institute(s)	Nenana	Denali	Institute(s)
ELD	ELD 1997			(31OCT02)	04NOV02	AERO
ENDI	ENDING 1964	1997/2001	UAF		14JUL03	UAF
F101	F 101 1964	2002	ADOT		17OCT03	UAF/UCB/PU
F113	F 113 1965	2002	CMJV		30MAY03	UAF/UCB/PU
F122	F 122 1965	2002	CMJV		15JUN03	UAF/UCB/PU
FAIR	(GILMORE CREEK)	Permanent 1991	JPL		03NOV02	JPL
FAIT	(FAITH 1952)	1997/2000	UAF		03JUN03	UAF/UCB/PU
FCRK	SOURDOUGH FISH CREEK AUG 91	1993/2000	NASA/UAF		07NOV02	UAF
FLY	GPS NO FLYN 1990	1994	CMJV		28MAY03	UAF/UCB/PU
FM01	(FM 83.1)	1994	PIPE		17OCT03	UAF/UCB/PU
FM02	(FM 83.2)	1994	PIPE		18OCT03	UAF/UCB/PU
FM03	(FM 83.3)	1994	PIPE		18OCT03	UAF/UCB/PU
FM04	(FM 83.4)	1994	PIPE		18OCT03	UAF/UCB/PU
FM05	(FM 83.5)	1994	PIPE		17OCT03	UAF/UCB/PU
FM06	(FM 83.6)	1994	PIPE		17OCT03	UAF/UCB/PU
FM07	(FM 83.7)	1994	PIPE		17OCT03	UAF/UCB/PU
FM08	(FM 83.8)	1994	PIPE		17OCT03	UAF/UCB/PU
FM09	(FM 83.9)	1994	PIPE		17OCT03	UAF/UCB/PU
FM10	(FM 83.10)	1994	PIPE		17OCT03	UAF/UCB/PU
FM11	(FM 83.11)	1994	PIPE		17OCT03	UAF/UCB/PU
FM12	(FM 83.12)	1994	PIPE		17OCT03	UAF/UCB/PU
FS32	32 8904-S 1998			(01NOV02)	04NOV02	AERO
FSHL	FISHLAKE 1922 1961	1995/2002	USGS/UAF		27NOV02	USGS
G63	G 63 1952	2002	CMJV		29MAY03	UAF/UCB/PU
GL22	G 122 1965	2002	CMJV		15JUN03	UAF/UCB/PU
GNAA	(GLENNALLEN FSL)	Permanent 1997	NOAA		03NOV02	NOAA
GRAV	GRAVY 1964	1995/2002	UAF		30JUN03	UAF
GRIZ	S5566 L1 C3 C5 L3 1969	1997/2000	UAF	23OCT02	10NOV02	UAF
GRNR	(GARNER)	Permanent 1997	UAF	23OCT02	03NOV02	UAF

Table B.1: GPS stations and surveys

SITE	Survey Marker Inscription (Name)	Pre-Earthquake Data		Post Earthquake Data		
		First/Last	Institute(s)	Nenana	Denali	Institute(s)
GUS1	(GUSTAVUS 1)	Permanent 1996	USCG		03NOV02	USCG
GUY	GUY 2001	2001/2002	UAF		12JUL03	UAF
H101	H 101 1964	2002	ADOT		17OCT03	UAF/UCB/PU
H34	H 34 1944	1999	ADOT		13OCT03	UAF/UCB/PU
H7	H 7 1928	2002	ADOT		12OCT03	UAF/UCB/PU
HAM	HAM 1947	1992/2002	NOAA/UAF		13JUL03	UAF
HAR3	HARRIET NO 3 1908 1944	1999/2002	UAF		25JUN03	UAF
HIDD	HIDDEN 1983	1992/1999	NOAA/UAF		31JUL03	UAF
HIWA	HIWAY 1970	1997/2002	UAF	24OCT02		UAF
HIW4	(HIWAY 4)			28OCT02	04NOV02	UAF
HNSC	S3151 C3 TRI 1952	1993	NOAA	(01NOV02)	05NOV02	AERO
HNSD	HNSD 1999	2002	UAF	(01NOV02)	05NOV02	AERO
HOMA	HOMAIR 1964	1995/2002	NOAA/UAF		27JUN03	UAF
HOME	HOME 1941	2002	ADOT		15OCT03	UAF/UCB/PU
HURR	HURR 1997	1997/2002	UAF		12NOV02	UCB
ILIA	E. BASE 1946	1999/2001	UAF		05AUG03	UAF
INVK	INUVIK	Permanent 2000	NRCan/GSD		03NOV02	NRCan/GSD
ISLZ	ISLE 1964 (AZ)	1995/2002	USGS/UAF		03JUL03	UAF
JANE	JANE 1998	1998/2002	UAF		18SEP03	UAF
JOIN	GPS NO JOIN 1990	1990	CMJV		29MAY03	UAF/UCB/PU
K112	K 112 1965	1994	ADOT		13JUN03	UAF/UCB/PU
K113	K 113 1965	2002	CMJV		29MAY03	UAF/UCB/PU
K76	K 76 1964	1996/2002	LCMF/UAF		18SEP03	UAF
KDK1	(KODIAK IS 1)	Permanent 1996	USCG		03NOV02	USCG
KEN1	(NIKISKI 1)	Permanent 1996	USCG		26NOV02	USCG
KENN	KENNY 1941	1994	ADOT/CMJV		16JUN03	UAF/UCB/PU
KODK	KODIAK IGS)	Permanent 2000	NASA		03NOV02	NASA
KSTN	KUSTATAN 1909 1953	1999/2002	UAF		25JUN03	UAF
L101	L 101 1964	2002	ADOT		17OCT03	UAF/UCB/PU

Table B.1: GPS stations and surveys

SITE	Survey Marker Inscription (Name)	Pre-Earthquake Data		Post Earthquake Data		
		First/Last	Institute(s)	Nenana	Denali	Institute(s)
L113	L 113 1965	2002	CMJV		30MAY03	UAF/UCB/PU
L122	L 122 1965	2002	CMJV		15JUN03	UAF/UCB/PU
L2C6	S11154 L2 C6 1993	1997/2000	UAF	24OCT02	03NOV02	UAF
LADU	GPS NO LADUE 1990	1994/2002	CMJV/ADOT		25MAY03	UAF/UCB/PU
LIBF	CS 307A	1993/1997	NASA		13JUN03	UAF/UCB/PU
LOG	LOG 1999	1999/2000	UAF		06NOV02	UAF
LSG1	LSG1 2001	2001	UAF		16JUL03	UAF
M110	M110 1965	1994/2000	ADOT/UAF	24OCT02	03NOV02	UAF
M113	M 113 1965	2002	CMJV		29MAY03	UAF/UCB/PU
M120	M 120 1965	1994	CMJV		11JUN03	UAF/UCB/PU
M126	M 126 1965	2002	UAF		29JUL03	UAF
MACL	GPS NO MACLEAN 1990	1990/1991	CMJV		25MAY03	UAF/UCB/PU
MAT	MAT	1994	CMJV		25MAY04	UAF/UCB/PU
MCAR	ELEV. 1414 K 1908	1993/1995	NASA		26JUL03	UAF
MEN	MEN 1947	1999/2000	UAF		06NOV02	UAF
MIDD	MIDDLETON 1933	1993/2000	USGS/UAF		23SEP03	USGS
MILC	GPS NO MILLER 1990	2002	ADOT		16JUN03	UAF/UCB/PU
MOS2	MOOSE NO 2 1944	1995/2002	UAF		05JUL03	UAF
MOTD	MOTD 2002	2002	UAF		13NOV02	GSC/PGC
MOTG	MONTAGUE	1993/1997	USGS		08JUL03	UAF
MPEN	MOOSE PEN 98	1998/2002	UAF		14NOV02	UCB
N101	N 101 1964	2002	ADOT		18JUN03	UAF/UCB/PU
N111	N 111 1965	1994	ADOT		12JUN03	UAF/UCB/PU
NENA	(NENANA)	1998/2001	UAF		10NOV02	UCB
NIK2	NIKISKI 2	1995/2002	UAF		15NOV02	UCB
NINI	NINILCHIK NO 3 1908	1998/2002	UAF		27JUN03	UAF
NJNC	GPS NO JUNCTION 1990	1994	CMJV		12JUN03	UAF/UCB/PU
NSLM	SLIMS R. 2000	2000	UAF/GSC/PGC		13NOV02	GSC/PGC
NWOD	EWP STA 3045+85 1989	1995/2001	USGS/UAF		25NOV02	USGS

Table B.1: GPS stations and surveys

SITE	Survey Marker Inscription (Name)	Pre-Earthquake Data		Post Earthquake Data		
		First/Last	Institute(s)	Nenana	Denali	Institute(s)
O8	O8 1923	2002	ADOT		29MAY03	UAF/UCB/PU
ORTT	GPS NO THOMAS 1990	1994/2000	CMJV/NOAA/UAF		04NOV02	UAF
P100	P 100 1964	2002	ADOT		18JUN03	UAF/UCB/PU
P586	(PBM 586.909)	1994	PIPE		17OCT03	UAF/UCB/PU
P592	(PBM 592.002)	1994	PIPE		07NOV03	UAF
PANA	PANA 1997	1997/2002	UAF	24OCT02	03NOV02	UAF
PAXS	PAXSON HILL AUG 91	1993/2000	NASA/UAF		07NOV02	UAF
PISA	PISA 1942	1997/2002	UAF	24OCT02	11NOV02	UAF
POPL	POPLAR 1964	1999/2002	UAF		29JUN03	UAF
POPZ	POPLAR 1964 (AZK)	1996/2002	UAF		29JUN03	UAF
POT3	(POTATO POINT 3)	Permanent 1996	USCG		03NOV02	USCG
POWE	POWER 1941	1992/2002	NOAA/UAF		10JUL03	UAF
PPLN	(PIPELINE BRIDGE)	1997/2000	UAF		02OCT03	UAF
PRTG	PORTAGE	1993/2002	USGS/UAF		15JUL03	UAF
PTVL	(PETERSVILLE)	2001/2002	UAF		28JUL03	UAF
PURI	PURIN 1944	1994/2001	NOAA/ADOT/UAF		12OCT03	UAF
Q122	Q 122 1965	2002	CMJV		15JUN03	UAF/UCB/PU
QRRY	QUARRY	1999/2002	UAF		25JUN03	UAF
R109	R 109 1965	1997/2000	UAF	25OCT02	05NOV02	UAF
R110	R 110 1965	1994	ADOT		10JUN03	UAF/UCB/PU
R122	R 122 1965	1994/2002	ADOT/CMJV		15JUN03	UAF/UCB/PU
RAND	RANDY 1973	1994	CMJV		04JUN03	UAF/UCB/PU
RD44	RED 1944	2000	ADOT		07JUL03	UAF
REED	REEDY 1964	1995/2002	USGS/UAF		26NOV02	USGS
RGGI	RUGGED ISLAND (AZ)	1999/2002	UAF		17SEP03	UAF
RIDG	GPS NO RIDGE	1994	CMJV		13JUN03	UAF/UCB/PU
ROC	ROCK 1912	1992/2002	NOAA/UAF		14JUL03	UAF
S1	S1 1922	1995/2002	USGS/UAF		12NOV02	ADOT
S113	S 113 1965	2002	CMJV		30MAY03	UAF/UCB/PU

Table B.1: GPS stations and surveys

SITE	Survey Marker Inscription (Name)	Pre-Earthquake Data		Post Earthquake Data		
		First/Last	Institute(s)	Nenana	Denali	Institute(s)
S119	S 119 1965	1994	CMJV		12JUN03	UAF/UCB/PU
S122	S 122 1965	2002	CMJV		15JUN03	UAF/UCB/PU
S174	S 174 WASH DC	1994	CMJV		11JUN03	UAF/UCB/PU
S72	S 72 1964	1997/2001	UAF		15JUL03	UAF
SELD	(SELDOVIA AIRPORT)	Permanent 2000	UAF		03NOV02	UAF
SG27	BARROW SUOMINET)	Permanent 2002	UAF		03NOV02	UAF
SHPA	SHEEP ASTRO 1943	2000	ADOT		06JUL03	UAF
SICH	GPS NO SICHUK 1990	1990/1991	CMJV		27MAY03	UAF/UCB/PU
SLBR	GPS NO SLBR 1990	1994	CMJV		28MAY03	UAF/UCB/PU
SLCH	SALCHA 1995	1995/2002	UAF		19MAY03	UAF/UCB/PU
SLIM	SLIME 1997	1997/2000	UAF	24OCT02	11NOV02	UAF
SOUR	(SOURDOUGH)	1993/2002	NASA/NOAA/ADOT		29MAY03	UAF/UCB/PU
SPIL	SPILLWAY 1952	1997/2000	UAF		05JUN03	UAF/UCB/PU
SSWB	SUMMIT SOUTH WEST BASE 1942	1997/2002	UAF	24OCT02	04NOV02	UAF
STEP	STEP 1913 1947	1993/2000	AVO/CVO		31AUG03	UAF
STRI	STRIP GPS 1988	1994/2002	CMJV/NOAA/ADOT/UAF		06NOV02	UAF
SXQD	SXQ D 1995	1995/2001	UAF		16NOV02	UCB
T122	T 122 1965	2002	CMJV		14JUN03	UAF/UCB/PU
T19	NO 19 1966	1993/2001	NASA/UAF		17SEP03	UAF
TAZL	TAZLINA 1941	1993/2001	NASA/UAF		08NOV02	UAF
TEM1	(TEM1)			(31OCT02)	04NOV02	AERO
THMP	THOMPSON PASS 1941	1993/2002	NASA/UAF		08JUL03	UAF
TLKA	(TALKEETNA FSL)	Permanent 1997	NOAA		03NOV02	NOAA
TNK1	TANK 1			(02NOV02)	05NOV02	AERO
TP26	(GPS 4 TP 26)	1999	ADOT		14OCT03	UAF/UCB/PU
TRAI	GPS NO TRAIL 1990	1999	ADOT		27MAY03	UAF/UCB/PU
TRLK	TRAIL LAKES 1995	1995/2002	UAF		30JUN03	UAF
TSEA	(TSEA)	Permanent 1999	TSE		03NOV02	TSE
TSIN	TSINA EAST BASE 1941	1995/2002	NASA/UAF		13JUN03	UAF/UCB/PU



Table B.1: GPS stations and surveys

SITE	Survey Marker Inscription (Name)	Pre-Earthquake Data		Post Earthquake Data		
		First/Last	Institute(s)	Nenana	Denali	Institute(s)
TURN	TURN 1996	1997/2002	UAF		01JUL03	UAF
TWB1	TANA WEST BASE NO 1 1943	1999	ADOT		27MAY03	UAF/UCB/PU
U113	U 113 1965	2002	CMJV		29MAY03	UAF/UCB/PU
U122	U 122 1965	2002	CMJV		14JUN03	UAF/UCB/PU
UAMF	(UAMF 95)	1995/2002	UAF		13NOV02	UAF
V113	V 113 1965	2002	CMJV		16JUN03	UAF/UCB/PU
V122	V 122 1965	2002	CMJV		14JUN03	UAF/UCB/PU
V61	V 61 1952	2002	ADOT		15OCT03	UAF/UCB/PU
W109	W 109 1965	1994	ADOT/CMJV		11JUN03	UAF/UCB/PU
W112	W 112 1965	1994	ADOT		12JUN03	UAF/UCB/PU
W176	W 176	1994	ADOT		26MAY03	UAF/UCB/PU
WHIT	(WHITEHORSE)	Permanent 1993	NRCan/GSD		03NOV02	NRCan/GSD
WICK	WICK 1997	1997/2000	UAF		04JUN03	UAF/UCB/PU
WILL	WILLOW CREEK NORTH BASE 1941	1994/1997	CMJV/NASA		16JUN03	UAF/UCB/PU
WOND	WONDER 1950	1998/2002	UAF		29JUL03	UAF/UCB/PU
X113	X 113 1965	2002	CMJV		30MAY03	UAF/UCB/PU
X122	X 122 1965	1994/2002	ADOT/CMJV		14JUN03	UAF/UCB/PU
X61	X 61 1952	2002	ADOT		14OCT03	UAF/UCB/PU
X7	X7 1943	1992/2002	GSC/PGC/UAF		12NOV02	GSC/PGC
Y111	Y 111 1965	1994	ADOT		13JUN03	UAF/UCB/PU
Y113	Y 113 1965	2002	CMJV		29MAY03	UAF/UCB/PU
Y122	Y 122 1965	2002	CMJV		13JUN03	UAF/UCB/PU
Y565	78Y.565	1992/2002	GSC/PGC/UAF		13NOV02	GSC/PCG
Y61	Y 61 1952	2002	ADOT		15OCT03	UAF/UCB/PU
YKTT	10143 1974	1992/2002	NOAA/UAF		01AUG03	UAF
YUKO	YUK	1999/2000	UAF		07JUN03	UAF/UCB/PU
Z113	Z 113 1965	2002	CMJV		30MAY03	UAF/UCB/PU
Z117	Z 117 1965	1994	CMJV		07JUN03	UAF/UCB/PU
Z122	Z 122 1965	2002	CMJV		13JUN03	UAF/UCB/PU

Table B.1: GPS stations and surveys

SITE	Survey Marker Inscription (Name)	Pre-Earthquake Data		Post Earthquake Data		
		First/Last	Institute(s)	Nenana	Denali	Institute(s)
Z22A	Z22 A 1994	1994/2002	NOAA/USGS/UAF		17AUG03	UAF

ADOT - Alaska Department of Transportation

AERO - AEROMAP

AVO - Alaska Volcano Observatory

CMJV - Crazy Mountains Joint Venture

CVO - USGS Cascades Volcano Observatory

NRCan/GSD - Geodetic Survey Division, Natural Resources Canada

GSC/PGC - Geological Survey Canada - Pacific Geoscience Center

LCMF - LCMF Inc. Alaska

NASA - National Aeronautics and Space Administration - Goddard Space Flight Center

PIPE - OceanTech Inc., for Alyeska

PU - Purdue University

UAF - University of Alaska Fairbanks

UCB - University of California Berkeley

USGS - U. S. Geological Survey

TSE - The Surveyer Exchange

\* - CRK1 and CRK2 installed in 2002 but stamped in 2003

Table B.2: Nenana Mt. earthquake displacements

SITE	Location			Displacement			Uncertainty		
	Lat. [°]	Lon. [°]	H [m]	N [m]	E [m]	V [m]	$\sigma_N$ [m]	$\sigma_E$ [m]	$\sigma_V$ [m]
B124	63.73494	-149.30884	859	0.006	0.020	0.007	0.004	0.004	0.007
CGLO	63.38826	-148.94963	718	-0.017	-0.010	-0.05	0.013	0.011	0.02
DFLY	63.79363	-148.91981	509	0.003	0.019	0.015	0.005	0.005	0.009
DH97	63.26515	-147.85505	944	0.024	0.004	-0.003	0.011	0.009	0.015
GRIZ	63.65239	-148.83297	619	-0.012	0.041	0.00	0.012	0.009	0.02
GRNR	63.83576	-148.97834	596	-0.018	0.009	0.008	0.004	0.004	0.007
HIWA	63.45883	-148.77867	947	-0.012	0.020	0.002	0.004	0.004	0.007
L2C6	63.38283	-148.86622	715	0.000	-0.006	-0.033	0.010	0.008	0.015
M110	63.30548	-148.18698	803	-0.026	-0.015	0.01	0.012	0.010	0.02
PANA	63.48375	-148.82038	670	-0.004	0.022	0.015	0.004	0.004	0.008
PISA	63.28465	-149.21055	731	-0.008	0.007	0.002	0.004	0.004	0.007
R109	63.39527	-148.64680	765	-0.009	-0.001	-0.001	0.010	0.008	0.015
SLIM	63.51200	-148.80409	650	0.003	0.033	0.008	0.012	0.009	0.02
SSWB	63.34131	-149.09023	733	-0.008	0.001	-0.010	0.005	0.005	0.009

Table B.3: Corrections

SITE	Interseismic						Postseismic				Nenana Mt. Eq.	
	N [m]	E [m]	U [m]	$\delta N$ [m]	$\delta E$ [m]	$\delta U$ [m]	N [m]	E [m]	$\delta N$ [m]	$\delta E$ [m]	N [m]	E [m]
0999	-0.0025	-0.0018	0.0100	0.0020	0.0029	0.0065	0	0	0	0	0	0
126G	-0.0122	-0.0035	0.0384	0.0145	0.0217	0.0493	-0.0074	0.0271	0.0110	0.0100	0	0
2201	0	0	0	0	0	0	-0.0018	-0.0024	0.0002	0.0002	0	0
2999	-0.0027	-0.0016	0.0100	0.0020	0.0029	0.0065	0	0	0	0	0	0
AL23	0.0017	-0.0062	0.0018	0.0004	0.0005	0.0011	0.0216	-0.0465	0.0130	0.0110	0.0048	-0.0071
ALAS	0	0	0	0	0	0	-0.0019	-0.0045	0.0005	0.0005	0	0
B122	0.0016	-0.0061	0.0018	0.0004	0.0005	0.0011	0.0276	-0.0546	0.0130	0.0110	0	0
B123	0.0017	-0.0062	0.0018	0.0004	0.0005	0.0011	0.0213	-0.0465	0.0130	0.0110	0.0049	-0.0073
B124	0.0004	-0.0015	0.0004	0.0003	0.0004	0.0010	-0.0050	-0.0067	0.0008	0.0008	0	0
BEAR	0	0	0	0	0	0	-0.0019	-0.0033	0.0004	0.0004	0	0
BRAD	0	0	0	0	0	0	-0.0022	-0.0028	0.0002	0.0002	0	0
BRBA	0.0021	-0.0025	-0.0029	0.0006	0.0009	0.0020	-0.0044	-0.0233	0.0024	0.0024	0	0
BREM	0	0	0	0	0	0	0.0129	-0.0036	0.0013	0.0013	0	0
BRLA	0.0205	-0.0242	-0.0289	0.0062	0.0086	0.0200	-0.0008	-0.0177	0.0018	0.0018	0	0
BROZ	0.071	-0.117	0	0.018	0.030	0	0.054	-0.035	0	0	0	0
BRPO	0.066	-0.092	0	0.018	0.028	0	0.005	-0.025	0	0	0	0
BRSR	0.065	-0.087	0	0.018	0.027	0	0.001	-0.027	0	0	0	0
BRWE	0.0209	-0.0249	-0.0289	0.0062	0.0086	0.0200	-0.0041	-0.0237	0.0024	0.0024	0	0
BRWN	0	0	0	0	0	0	0	0	0	0	-0.0041	0.0044
BUMP	0.0986	-0.0574	0.1040	0.0078	0.0111	0.0264	0.0225	-0.0084	0.0024	0.0024	0	0
C122	0.0023	-0.0049	0.0043	0.0003	0.0005	0.0010	0.0273	-0.0539	0.0130	0.0110	0	0
C123	0.0013	-0.0068	0.0004	0.0004	0.0005	0.0011	0.0210	-0.0464	0.0130	0.0110	0.0051	-0.0076
C96	0.0020	-0.0041	0.0038	0.0003	0.0004	0.0009	0.0358	-0.0830	0.0060	0.0060	0	0
CARL	0	0	0	0	0	0	-0.0049	-0.0086	0.0010	0.0010	-0.0163	0.0314
CC	0	0	0	0	0	0	-0.0014	-0.0024	0.0002	0.0002	0	0
CKLN	0	0	0	0	0	0	-0.0047	-0.0104	0.0011	0.0011	0	0
COGH	0	0	0	0	0	0	-0.0002	-0.0049	0.0005	0.0005	0	0
COMB	0	0	0	0	0	0	0.0013	-0.0005	0.0001	0.0001	0	0
CPLK	0	0	0	0	0	0	-0.0015	-0.0031	0.0003	0.0003	0	0

Table B.3: Corrections

SITE	Interseismic						Postseismic				Nenana Mt. Eq.	
	N [m]	E [m]	U [m]	$\delta N$ [m]	$\delta E$ [m]	$\delta U$ [m]	N [m]	E [m]	$\delta N$ [m]	$\delta E$ [m]	N [m]	E [m]
CRK1	0.0046	-0.0021	0.0021	0.0009	0.0013	0.0031	-0.0399	0.0665	0.0064	0.0064	0	0
CRK2	0.0048	-0.0022	0.0022	0.0010	0.0013	0.0032	-0.0406	0.0666	0.0064	0.0064	0	0
D122	0.0023	-0.0049	0.0043	0.0003	0.0005	0.0010	0.0271	-0.0535	0.0130	0.0110	0	0
DAHL	0	0	0	0	0	0	-0.0018	-0.0038	0.0004	0.0004	0	0
DIAN	0	0	0	0	0	0	-0.0037	-0.0049	0.0004	0.0004	0	0
DIXI	0	0	0	0	0	0	0.0018	-0.0031	0.0004	0.0004	0	0
E113	0.0022	-0.0047	0.0043	0.0003	0.0005	0.0010	0.0336	-0.0672	0.0130	0.0110	0	0
E175	-0.0010	-0.0009	0.0042	0.0016	0.0024	0.0054	-0.0087	0.0336	0.0035	0.0035	0	0
EAGL	0	0	0	0	0	0	-0.0056	-0.0086	0.0007	0.0007	0	0
EFRK	-0.0019	-0.0023	-0.0032	0.0009	0.0010	0.0035	-0.0037	-0.0088	0.0010	0.0010	-0.0029	0.0047
EGG	0	0	0	0	0	0	0.0004	-0.0035	0.0004	0.0004	0	0
EGL2	0	0	0	0	0	0	-0.0104	0.0037	0.0011	0.0011	0	0
EKG3	0	0	0	0	0	0	-0.0022	-0.0033	0.0004	0.0004	0	0
ENDI	0	0	0	0	0	0	-0.0016	-0.0042	0.0004	0.0004	0	0
F101	0.0024	-0.0028	-0.0035	0.0007	0.0010	0.0024	-0.0517	0.0595	0.0064	0.0064	0	0
F113	0.0022	-0.0047	0.0043	0.0003	0.0005	0.0010	0.0334	-0.0668	0.0130	0.0110	0	0
F122	0.0016	-0.0061	0.0018	0.0004	0.0005	0.0011	0.0266	-0.0525	0.0130	0.0110	0	0
FAIT	0	0	0	0	0	0	-0.0118	0.0042	0.0013	0.0013	0	0
FLY	0.0178	-0.0294	0.0143	0.0089	0.0089	0.0178	0.0963	-0.0314	0.0101	0.0101	0	0
FM01	0.0315	-0.0148	0.0148	0.0131	0.0172	0.0403	-0.0169	-0.0036	0.0014	0.0014	0	0
FM02	0.0315	-0.0148	0.0148	0.0131	0.0172	0.0403	-0.0167	-0.0034	0.0014	0.0014	0	0
FM03	0.0315	-0.0148	0.0148	0.0131	0.0172	0.0403	-0.0085	-0.0086	0.0017	0.0017	0	0
FM04	0.0315	-0.0148	0.0148	0.0131	0.0172	0.0403	-0.0088	-0.0085	0.0017	0.0017	0	0
FM05	0.0315	-0.0148	0.0148	0.0131	0.0172	0.0403	-0.0084	-0.0088	0.0017	0.0017	0	0
FM06	0.0315	-0.0148	0.0148	0.0131	0.0172	0.0403	-0.0079	-0.0091	0.0017	0.0017	0	0
FM07	0.0315	-0.0148	0.0148	0.0131	0.0172	0.0403	-0.0069	-0.0100	0.0018	0.0018	0	0
FM08	0.0315	-0.0148	0.0148	0.0131	0.0172	0.0403	-0.0069	-0.0101	0.0018	0.0018	0	0
FM09	0.0315	-0.0148	0.0148	0.0131	0.0172	0.0403	-0.0066	-0.0104	0.0018	0.0018	0	0
FM10	0.0315	-0.0148	0.0148	0.0131	0.0172	0.0403	-0.0067	-0.0103	0.0018	0.0018	0	0

Table B.3: Corrections

SITE	Interseismic						Postseismic				Nenana Mt. Eq.	
	N [m]	E [m]	U [m]	$\delta N$ [m]	$\delta E$ [m]	$\delta U$ [m]	N [m]	E [m]	$\delta N$ [m]	$\delta E$ [m]	N [m]	E [m]
FM11	0.0315	-0.0148	0.0148	0.0131	0.0172	0.0403	0.0119	-0.0427	0.0021	0.0021	0	0
FM12	0.0315	-0.0148	0.0148	0.0131	0.0172	0.0403	0.0119	-0.0425	0.0020	0.0020	0	0
G63	0.0022	-0.0047	0.0043	0.0003	0.0005	0.0010	0.0347	-0.0695	0.0130	0.0110	0	0
GL22	0.0016	-0.0061	0.0018	0.0004	0.0005	0.0011	0.0263	-0.0518	0.0130	0.0110	0	0
GRAV	0	0	0	0	0	0	-0.0017	-0.0035	0.0004	0.0004	0	0
GUY	0	0	0	0	0	0	0.0028	-0.0034	0.0004	0.0004	0	0
H101	0.0024	-0.0028	-0.0035	0.0007	0.0010	0.0024	-0.0494	0.0617	0.0064	0.0064	0	0
H34	-0.0042	-0.0047	0.0187	0.0070	0.0106	0.0240	-0.0080	0.0749	0.0057	0.0057	0	0
H7	0.0016	0.0002	0.0024	0.0008	0.0011	0.0027	-0.0523	0.0537	0.0060	0.0060	0	0
HAM	0	0	0	0	0	0	-0.0005	-0.0046	0.0005	0.0005	0	0
HAR3	0	0	0	0	0	0	-0.0021	-0.0030	0.0004	0.0004	0	0
HIDD	0	0	0	0	0	0	0.0015	-0.0006	0.0002	0.0002	0	0
HOME	0.0044	-0.0065	0.0049	0.0006	0.0009	0.0018	0.0404	-0.0768	0.0064	0.0064	0	0
HURR	0	0	0	0	0	0	0	0	0	0	-0.0043	-0.0040
ILIA	0	0	0	0	0	0	-0.0016	-0.0019	0.0002	0.0002	0	0
ISLZ	0	0	0	0	0	0	-0.0028	-0.0052	0.0006	0.0006	0	0
JANE	0	0	0	0	0	0	-0.0011	-0.0026	0.0003	0.0003	0	0
JOIN	0.0444	-0.0648	0.0492	0.0058	0.0090	0.0176	0.032	-0.069	0.00760	0.0076	0	0
K112	0.0081	-0.0689	-0.0089	0.0032	0.0044	0.0097	0.0152	-0.0453	0.0130	0.0110	0.0095	-0.0107
K113	0.0022	-0.0048	0.0043	0.0003	0.0005	0.0010	0.0326	-0.0650	0.0130	0.0110	0	0
K76	0	0	0	0	0	0	-0.0019	-0.0037	0.0003	0.0003	0	0
KENN	0.0924	-0.0538	0.0825	0.0090	0.0135	0.0036	0.0210	-0.0100	0.0023	0.0023	0	0
KSTN	0	0	0	0	0	0	-0.0024	-0.0038	0.0004	0.0004	0	0
L101	0.0018	-0.0021	-0.0026	0.0006	0.0008	0.0018	-0.0489	0.0635	0.0066	0.0066	0	0
L113	0.0022	-0.0048	0.0043	0.0003	0.0005	0.0010	0.0322	-0.0643	0.0130	0.0110	0	0
L122	0.0017	-0.0061	0.0018	0.0004	0.0005	0.0011	0.0250	-0.0491	0.0130	0.0110	0	0
LADU	-0.0010	-0.0009	0.0042	0.0016	0.0024	0.0054	-0.0097	0.0342	0.0036	0.0036	0	0
LIBF	0	0	0	0	0	0	0.0231	-0.0079	0.0024	0.0024	0	0
LOG	-0.0021	-0.0027	0.0093	0.0020	0.0029	0.0065	0	0	0	0	0	0

Table B.3: Corrections

SITE	Interseismic						Postseismic				Nenana Mt. Eq.	
	N [m]	E [m]	U [m]	$\delta N$ [m]	$\delta E$ [m]	$\delta U$ [m]	N [m]	E [m]	$\delta N$ [m]	$\delta E$ [m]	N [m]	E [m]
LSG1	0.0210	-0.0090	0.0173	0.0036	0.0047	0.0112	-0.0038	-0.0147	0.0015	0.0015	0	0
M113	0.0022	-0.0048	0.0043	0.0003	0.0005	0.0010	0.0320	-0.0639	0.0130	0.0110	0	0
M120	-0.0143	-0.0081	-0.0403	0.0072	0.0089	0.0228	-0.0118	0.0035	0.0012	0.0012	0	0
M126	-0.0046	-0.0006	-0.0022	0.0006	0.0009	0.0023	-0.0031	-0.0094	0.0010	0.0010	-0.0016	0.0015
MACL	-0.0108	-0.0156	0.0528	0.0199	0.0299	0.0678	0	0	0	0	0	0
MAT	0.0159	-0.0387	0.0159	0.0099	0.0099	0.0198	0.1727	-0.1017	0.0110	0.0100	0	0
MCAR	0	0	0	0	0	0	0.0165	-0.0065	0.0018	0.0018	0	0
MIDD	0	0	0	0	0	0	0.0031	-0.0009	0.0003	0.0003	0	0
MILC	0.0025	-0.0023	0.0021	0.0005	0.0006	0.0013	0.0119	-0.0425	0.0020	0.0020	0	0
MOS2	0	0	0	0	0	0	-0.0048	-0.0093	0.0010	0.0010	0	0
MOTD	0.0029	-0.0002	0.0005	0.0005	0.0006	0.0016	0	0	0	0	0	0
MOTG	0	0	0	0	0	0	0.0012	-0.0014	0.0002	0.0002	0	0
N101	0.0032	-0.0014	0.0014	0.0006	0.0009	0.0021	-0.0398	0.0517	0.0065	0.0065	0	0
N111	0.0009	-0.0805	-0.0331	0.0087	0.0108	0.0268	0.0098	-0.0443	0.0130	0.0110	0.0273	-0.0271
NINI	0	0	0	0	0	0	-0.0018	-0.0025	0.0003	0.0003	0	0
NJNC	-0.0107	-0.0063	0.0394	0.0149	0.0223	0.0506	-0.0023	0.0303	0.0030	0.0030	0	0
O8	0.0046	-0.0067	0.0051	0.0006	0.0009	0.0018	0.0239	-0.0421	0.0048	0.0048	0	0
P100	0.0016	0.0002	0.0023	0.0008	0.0010	0.0026	-0.0519	0.0542	0.0060	0.0060	0	0
P586	0.0315	-0.0148	0.0148	0.0131	0.0172	0.0403	-0.0209	-0.0009	0.0016	0.0016	0	0
P592	0.0269	-0.0306	0.0287	0.0131	0.0172	0.0403	0.0065	-0.0596	0.0037	0.0037	0	0
POPL	0	0	0	0	0	0	-0.0019	-0.0034	0.0004	0.0004	0	0
POPZ	0	0	0	0	0	0	-0.0019	-0.0034	0.0004	0.0004	0	0
POWE	0	0	0	0	0	0	0.0064	-0.0039	0.0007	0.0007	0	0
PPLN	0	0	0	0	0	0	-0.0339	0.0303	0.0034	0.0034	0	0
PRTG	0	0	0	0	0	0	-0.0013	-0.0040	0.0004	0.0004	0	0
PTVL	0	0	0	0	0	0	-0.0047	-0.0111	0.0012	0.0012	0	0
PURI	0	0	0	0	0	0	-0.0063	-0.0148	0.0012	0.0012	0	0
Q122	0.0017	-0.0062	0.0018	0.0004	0.0005	0.0011	0.0236	-0.0469	0.0130	0.0110	0	0
QRRY	0	0	0	0	0	0	-0.0023	-0.0035	0.0004	0.0004	0	0

Table B.3: Corrections

SITE	Interseismic						Postseismic				Nenana Mt. Eq.	
	N [m]	E [m]	U [m]	$\delta N$ [m]	$\delta E$ [m]	$\delta U$ [m]	N [m]	E [m]	$\delta N$ [m]	$\delta E$ [m]	N [m]	E [m]
R110	-0.0072	-0.0743	-0.0591	0.0117	0.0183	0.0382	-0.0074	-0.0332	0.0130	0.0110	0.0016	-0.0275
R122	0.0017	-0.0062	0.0018	0.0004	0.0005	0.0011	0.0234	-0.0469	0.0130	0.0110	0	0
RAND	-0.0036	-0.0394	-0.0054	0.0179	0.0179	0.0358	-0.0046	-0.0171	0.0018	0.0018	-0.0061	-0.0048
RD44	0.0336	-0.0102	0.0319	0.0036	0.0046	0.0111	-0.0031	-0.0110	0.0011	0.0011	0	0
RGGI	0	0	0	0	0	0	-0.0013	-0.0027	0.0002	0.0002	0	0
RIDG	-0.0072	-0.0018	-0.0296	0.0008	0.0008	0.0015	-0.0124	0.0041	0.0013	0.0013	0	0
ROC	0	0	0	0	0	0	0.0006	-0.0031	0.0003	0.0003	0	0
S113	0.0023	-0.0048	0.0043	0.0003	0.0005	0.0010	0.0305	-0.0606	0.0130	0.0110	0	0
S119	-0.0215	-0.0143	-0.0519	0.0072	0.0089	0.0228	-0.0109	0.0027	0.0011	0.0011	0	0
S122	0.0017	-0.0062	0.0018	0.0004	0.0005	0.0011	0.0233	-0.0468	0.0130	0.0110	0	0
S174	-0.0107	-0.0072	0.0394	0.0149	0.0223	0.0506	-0.0054	0.0300	0.0030	0.0030	0	0
S72	0	0	0	0	0	0	-0.0022	-0.0048	0.0005	0.0005	0	0
SHPA	0.0313	-0.0134	0.0257	0.0054	0.0070	0.0166	-0.0017	-0.0110	0.0011	0.0011	0	0
SICH	-0.0120	-0.0144	0.0528	0.0199	0.0299	0.0678	0	0	0	0	0	0
SLBR	0.0107	-0.0455	0.0143	0.0089	0.0089	0.0178	0.0828	-0.0637	0.0104	0.0104	0	0
SLCH	0	0	0	0	0	0	-0.0171	0.0075	0.0019	0.0019	0	0
SOUR	0	0	0	0	0	0	0.0273	-0.0531	0.0060	0.0060	0	0
SPIL	0	0	0	0	0	0	-0.0119	0.0043	0.0013	0.0013	0	0
STEP	0	0	0	0	0	0	-0.0024	-0.0024	0.0002	0.0002	0	0
T122	0.0017	-0.0062	0.0018	0.0004	0.0005	0.0011	0.0232	-0.0468	0.0130	0.0110	0	0
T19	0	0	0	0	0	0	-0.0017	-0.0032	0.0003	0.0003	0	0
THMP	0	0	0	0	0	0	0.0096	-0.0040	0.0010	0.0010	0	0
TP26	-0.0042	-0.0047	0.0187	0.0070	0.0106	0.0240	-0.0075	0.0732	0.0056	0.0056	0	0
TRAI	-0.0039	-0.0043	0.0170	0.0064	0.0096	0.0218	-0.0087	0.0862	0.0065	0.0065	0	0
TRLK	0	0	0	0	0	0	-0.0014	-0.0033	0.0004	0.0004	0	0
TSIN	0	0	0	0	0	0	0.0112	-0.0044	0.0012	0.0012	0	0
TWB1	-0.0039	-0.0043	0.0170	0.0064	0.0096	0.0218	-0.0008	0.0789	0.0060	0.0060	0	0
U113	0.0023	-0.0048	0.0043	0.0003	0.0005	0.0010	0.0299	-0.0594	0.0130	0.0110	0	0
U122	0.0017	-0.0062	0.0018	0.0004	0.0005	0.0011	0.0231	-0.0468	0.0130	0.0110	0	0



Table B.3: Corrections

SITE	Interseismic						Postseismic				Nenana Mt. Eq.	
	N [m]	E [m]	U [m]	$\delta N$ [m]	$\delta E$ [m]	$\delta U$ [m]	N [m]	E [m]	$\delta N$ [m]	$\delta E$ [m]	N [m]	E [m]
V113	0.0016	-0.0060	0.0018	0.0004	0.0005	0.0011	0.0296	-0.0587	0.0130	0.0110	0	0
V122	0.0017	-0.0062	0.0018	0.0004	0.0005	0.0011	0.0230	-0.0468	0.0130	0.0110	0	0
V61	0.0044	-0.0065	0.0049	0.0006	0.0009	0.0018	0.0378	-0.0693	0.0059	0.0059	0	0
W109	-0.0170	-0.0510	-0.0224	0.0095	0.0119	0.0299	-0.0169	-0.0328	0.0037	0.0037	-0.0247	-0.0195
W112	0.0116	-0.0635	0.0036	0.0032	0.0044	0.0097	0.0182	-0.0459	0.0130	0.0110	0.0071	-0.0090
W176	-0.0113	-0.0052	0.0381	0.0144	0.0216	0.0489	-0.0074	0.0288	0.0110	0.0100	0	0
WICK	0	0	0	0	0	0	-0.0104	0.0036	0.0011	0.0011	0	0
WILL	0.0861	-0.0565	0.0610	0.0090	0.0135	0.0036	0.0196	-0.0127	0.0023	0.0023	0	0
WOND	0	0	0	0	0	0	-0.0027	-0.0073	0.0008	0.0008	-0.0011	0.0012
X113	0.0023	-0.0049	0.0043	0.0003	0.0005	0.0010	0.0289	-0.0572	0.0130	0.0110	0	0
X122	0.0017	-0.0062	0.0018	0.0004	0.0005	0.0011	0.0225	-0.0467	0.0130	0.0110	0.0042	-0.0065
X61	0.0044	-0.0065	0.0049	0.0006	0.0009	0.0018	0.0371	-0.0632	0.0055	0.0055	0	0
Y111	0.0089	-0.0698	-0.0089	0.0032	0.0044	0.0097	0.0124	-0.0448	0.0130	0.0110	0.0140	-0.0143
Y113	0.0023	-0.0049	0.0043	0.0003	0.0005	0.0010	0.0286	-0.0566	0.0130	0.0110	0	0
Y122	0.0017	-0.0062	0.0018	0.0004	0.0005	0.0011	0.0222	-0.0466	0.0130	0.0110	0.0044	-0.0067
Y61	0.0044	-0.0065	0.0049	0.0006	0.0009	0.0018	0.0362	-0.0616	0.0053	0.0053	0	0
YKTT	0	0	0	0	0	0	0.0019	-0.0009	0.0002	0.0002	0	0
YUKO	0	0	0	0	0	0	-0.0071	0.0024	0.0007	0.0007	0	0
Z113	0.0023	-0.0049	0.0043	0.0003	0.0005	0.0010	0.0283	-0.0559	0.0130	0.0110	0	0
Z117	-0.0260	-0.0251	-0.0914	0.0072	0.0089	0.0228	-0.0108	0.0009	0.0011	0.0011	0	0
Z122	0.0017	-0.0062	0.0018	0.0004	0.0005	0.0011	0.0219	-0.0466	0.0130	0.0110	0.0046	-0.0070
Z22A	0	0	0	0	0	0	-0.0080	-0.0125	0.0010	0.0010	0	0

Table B.4: Denali Fault earthquake displacements

SITE	Location			Displacement			Uncertainty		
	Lat. [°]	Lon. [°]	H [m]	N [m]	E [m]	V [m]	$\sigma_N$ [m]	$\sigma_E$ [m]	$\sigma_V$ [m]
0999	63.66500	-142.27477	1068	0.0059	0.1093	-0.0402	0.0066	0.0075	0.0157
126G	64.08648	-141.00134	1304	0.0225	0.0541	-0.0070	0.0184	0.0284	0.0539
2201	59.52490	-150.55139	363	0.0018	-0.0077	0.1202	0.0107	0.0090	0.0140
2999	64.02873	-142.07611	749	0.0029	0.0684	-0.0292	0.0066	0.0075	0.0157
7297	62.68804	-145.42612	746	0.1635	-0.2878	-0.0203	0.0066	0.0055	0.0104
8130	63.95850	-138.69444	455	0.0044	0.0296	0.0290	0.0072	0.0059	0.0116
AL23	63.10546	-146.59623	963	0.0510	-0.4788	-0.1221	0.0160	0.0218	0.0277
ALAS	60.89307	-149.06387	27	0.0040	-0.0228	-0.0071	0.0075	0.0062	0.0112
ANC1	61.18238	-149.99677	47	-0.0047	-0.0154	-0.0000	0.0058	0.0049	0.0088
ATT	63.50253	-145.84719	813	-0.7554	1.3035	-0.0249	0.0073	0.0063	0.0109
ATW2	61.59775	-149.13229	97	-0.0072	-0.0270	-0.0022	0.0058	0.0049	0.0089
B122	63.05862	-146.07427	932	0.1470	-0.5535	-0.0383	0.0164	0.0210	0.0275
B123	63.10188	-146.62083	1016	0.0434	-0.4691	0.0114	0.0184	0.0387	0.0514
B124	63.73494	-149.30884	859	-0.0470	0.0095	0.0498	0.0045	0.0040	0.0074
BEAR	60.45542	-150.24777	312	0.0012	-0.0020	-0.0029	0.0084	0.0068	0.0125
BRAD	59.75513	-150.85189	378	-0.0093	-0.0120	-0.0133	0.0049	0.0037	0.0071
BRBA	63.49299	-146.48975	1753	-0.3336	1.7143	0.2141	0.0250	0.0255	0.0291
BREM	60.96817	-144.60559	843	0.0674	-0.0057	-0.0061	0.0085	0.0069	0.0124
BRLA	63.49445	-146.38880	1623	-0.2163	1.6149	-0.1446	0.0327	0.0563	0.0607
BROZ	63.42836	-146.46578	2067	0.29	-1.57	-	0.2*	0.2*	-
BRPO	63.47859	-146.58183	1942	0.54	-2.27	-	0.2*	0.2*	-
BRSR	63.47299	-146.43412	1708	0.53	-1.88	-	0.2*	0.2*	-
BRWE	63.49433	-146.50803	1851	-0.4178	1.5315	0.1964	0.0525	0.0854	0.1639
BRWN	64.17069	-149.29505	278	-0.0259	0.0366	0.0390	0.0086	0.0079	0.0143
BSB4	63.90650	-145.78909	548	-0.2374	0.1910	0.0039	0.0078	0.0067	0.0117
BUMP	61.67528	-144.73695	373	0.1513	-0.0311	0.0886	0.0159	0.0166	0.0337
C122	63.06720	-146.10080	968	0.1193	-0.5676	-0.0222	0.0197	0.0269	0.0363
C123	63.10444	-146.65347	990	0.0330	-0.4568	-0.0240	0.0208	0.0421	0.0619
C96	63.21148	-145.63893	931	0.4623	-1.2258	-0.0736	0.0120	0.0191	0.0269
CARL	63.55149	-148.80893	677	-0.0319	-0.0031	-0.1268	0.0158	0.0127	0.0216
CC	59.69421	-149.74790	16	0.0038	-0.0014	0.0948	0.0084	0.0066	0.0128
CENA	65.49816	-144.67763	282	-0.0373	0.0185	0.0257	0.0084	0.0099	0.0155
CGLO	63.38826	-148.94963	718	-0.0261	-0.0585	-0.0163	0.0050	0.0044	0.0081
CHI4	60.23774	-146.64652	91	0.0150	0.0009	0.0034	0.0052	0.0049	0.0084
CKLN	61.76466	-148.53678	248	-0.0005	-0.0276	-0.0247	0.0085	0.0072	0.0126
CLGO	64.87378	-147.86049	196	-0.0514	0.0233	0.0175	0.0057	0.0051	0.0093
CMJV	61.16583	-149.84492	58	-0.0043	-0.0198	0.0062	0.0058	0.0049	0.0088
COGH	61.07038	-147.94713	57	0.0136	-0.0131	0.0132	0.0068	0.0056	0.0103
COMB	59.66985	-138.63932	1286	0.0153	-0.0019	-0.0578	0.0093	0.0077	0.0130
CPLK	60.38298	-149.72094	378	-0.0055	0.0036	0.0229	0.0092	0.0073	0.0129

Table B.4: Denali Fault earthquake displacements

SITE	Location			Displacement			Uncertainty		
	Lat. [°]	Lon. [°]	H [m]	N [m]	E [m]	V [m]	$\sigma_N$ [m]	$\sigma_E$ [m]	$\sigma_V$ [m]
CPR	60.48944	-149.74545	181	0.0006	-0.0049	-0.0352	0.0120	0.0097	0.0169
CRK1	63.54432	-145.86464	653	-0.6490	0.9508	-0.0284	0.0160	0.0282	0.0319
CRK2	63.55228	-145.86724	642	-0.6630	0.9264	-0.0518	0.0127	0.0198	0.0315
D122	63.07928	-146.11524	984	0.1362	-0.5849	-0.0364	0.0147	0.0134	0.0160
DAHL	60.65402	-149.48788	393	0.0109	-0.0062	0.0108	0.0068	0.0055	0.0108
DEST	61.21692	-138.72188	858	0.0073	0.0004	-0.0156	0.0074	0.0060	0.0108
DFLY	63.79363	-148.91981	509	-0.0702	0.0339	0.0178	0.0049	0.0044	0.0086
DH97	63.26515	-147.85505	943	0.0078	-0.1957	-0.0530	0.0057	0.0050	0.0091
DIAN	60.58787	-151.22793	37	0.0027	-0.0078	-0.0149	0.0075	0.0060	0.0112
DIXI	60.73148	-147.44640	17	0.0181	-0.0164	0.0349	0.0093	0.0076	0.0143
DNLY	63.69506	-145.88763	557	-0.4040	0.4719	-0.0038	0.0075	0.0065	0.0112
E113	63.07030	-145.59093	1051	0.3032	-0.7990	-0.0456	0.0159	0.0234	0.0279
E175	63.38678	-142.52980	631	0.0304	0.2215	-0.1640	0.0102	0.0178	0.0233
EAGL	61.25748	-149.52869	1205	0.0084	-0.0249	-0.0188	0.0080	0.0064	0.0121
EFRK	63.55921	-149.79401	946	-0.0170	-0.0186	0.0015	0.0050	0.0045	0.0095
EGG	60.77404	-147.96265	17	0.0134	-0.0062	0.0076	0.0080	0.0067	0.0114
EGL2	65.49089	-145.38755	1171	-0.0358	0.0317	0.0105	0.0103	0.0087	0.0163
EKG3	60.48463	-151.83819	68	0.0003	0.0023	-0.0253	0.0063	0.0050	0.0092
ELD	58.97197	-135.22232	10	0.0046	-0.0021	0.0086	0.0056	0.0047	0.0088
ENDI	60.81847	-148.97571	19	0.0195	-0.0330	-0.0044	0.0146	0.0125	0.0219
F101	63.67035	-145.88548	556	-0.4304	0.5409	-0.0167	0.0108	0.0157	0.0230
F113	63.08347	-145.60711	1029	0.2985	-0.8077	-0.0474	0.0152	0.0153	0.0186
F122	63.07437	-146.15303	1084	0.1045	-0.5364	-0.0548	0.0174	0.0255	0.0314
FAIR	64.97800	-147.49924	319	-0.0513	0.0237	0.0226	0.0057	0.0051	0.0095
FAIT	65.34713	-146.26100	798	-0.0488	0.0318	0.0056	0.0101	0.0085	0.0155
FCRK	63.09070	-145.47530	1047	0.3872	-0.9272	-0.0784	0.0064	0.0053	0.0098
FLY	62.52840	-143.24828	968	0.7270	-0.3969	0.1402	0.0190	0.0186	0.0295
FM01	63.40584	-145.74117	768	-1.2127	2.4065	0.2191	0.0262	0.0361	0.0498
FM02	63.40596	-145.74387	765	-1.2135	2.4535	0.1744	0.0234	0.0319	0.0430
FM03	63.39306	-145.74242	816	-1.2802	2.4300	0.4641	0.0316	0.0350	0.0526
FM04	63.39333	-145.73945	816	-1.2618	2.4877	0.2452	0.0262	0.0338	0.0457
FM05	63.39252	-145.73890	819	-1.3506	2.6448	0.3313	0.0267	0.0351	0.0458
FM06	63.39183	-145.74159	825	-1.2703	2.4659	0.2555	0.0286	0.0341	0.0483
FM07	63.38869	-145.73574	808	-1.2849	2.5361	0.2944	0.0250	0.0351	0.0474
FM08	63.38827	-145.73317	802	-1.3077	2.4891	0.2982	0.0268	0.0364	0.0493
FM09	63.38746	-145.73299	799	-1.3106	2.4963	0.2651	0.0244	0.0335	0.0441
FM10	63.38792	-145.73499	806	-1.3027	2.4737	0.2715	0.0275	0.0338	0.0468
FM11	63.38197	-145.73304	776	1.4514	-1.8908	-1.2403	0.0288	0.0361	0.0501
FM12	63.38185	-145.73044	779	-1.2961	1.5763	-0.0476	0.0289	0.0408	0.0550
FS32	59.14868	-135.34696	9	0.0022	-0.0009	0.0249	0.0065	0.0065	0.0125

Table B.4: Denali Fault earthquake displacements

SITE	Location			Displacement			Uncertainty		
	Lat. [°]	Lon. [°]	H [m]	N [m]	E [m]	V [m]	$\sigma_N$ [m]	$\sigma_E$ [m]	$\sigma_V$ [m]
FSHL	61.52473	-149.88242	135	-0.0066	-0.0238	-0.0300	0.0077	0.0062	0.0115
G63	63.03141	-145.50124	834	0.3091	-0.7497	-0.0408	0.0149	0.0169	0.0194
GL22	63.07345	-146.18095	1117	0.0945	-0.5079	-0.0736	0.0156	0.0213	0.0286
GNAA	62.11238	-145.97022	601	0.0472	-0.0521	0.0215	0.0081	0.0095	0.0153
GRAV	60.56437	-149.58153	324	0.0062	-0.0157	-0.0019	0.0079	0.0065	0.0122
GRIZ	63.65239	-148.83297	619	-0.0442	-0.0004	0.0067	0.0050	0.0044	0.0085
GRNR	63.83576	-148.97834	596	-0.0464	0.0322	0.0175	0.0057	0.0050	0.0092
GUS1	58.41749	-135.69734	20	0.0230	0.0115	0.0072	0.0082	0.0164	0.0211
GUY	60.87929	-147.09595	440	-0.0034	-0.0106	0.0140	0.0080	0.0064	0.0118
H101	63.64132	-145.89129	578	-0.4757	0.6051	0.0248	0.0095	0.0110	0.0183
H34	63.23398	-143.05170	550	0.0353	0.4019	-0.0943	0.0120	0.0177	0.0327
H7	63.76014	-145.85535	871	-0.2901	0.4145	-0.2219	0.0207	0.0320	0.0567
HAM	61.00556	-148.09136	16	0.0074	-0.0181	0.0390	0.0069	0.0056	0.0103
HAR3	60.39035	-152.27123	96	0.0066	-0.0120	-0.0010	0.0082	0.0067	0.0125
HIDD	59.70548	-138.94547	1077	0.0205	0.0107	-0.0171	0.0090	0.0077	0.0125
HIW4	63.46434	-148.80727	667	-0.0324	-0.0427	-0.0177	0.0057	0.0050	0.0091
HNSC	59.24230	-135.51780	13	-0.0036	0.0029	0.0304	0.0073	0.0086	0.0151
HNSD	59.24810	-135.53420	17	0.0060	0.0073	0.0475	0.0080	0.0098	0.0163
HOMA	59.63899	-151.49155	31	-0.0066	-0.0011	-0.0072	0.0070	0.0057	0.0108
HOME	62.71327	-145.43127	835	0.1632	-0.3125	0.0158	0.0095	0.0118	0.0188
HURR	62.99930	-149.60892	606	-0.0150	-0.0489	-0.0339	0.0075	0.0062	0.0111
ILIA	59.76328	-154.82072	51	-0.0040	-0.0091	0.0412	0.0100	0.0076	0.0139
INVK	68.30619	-133.52696	46	-0.0033	0.0024	0.0081	0.0057	0.0057	0.0105
ISLZ	61.02066	-149.74561	17	0.0153	-0.0074	-0.0160	0.0072	0.0059	0.0110
JANE	60.18298	-149.64356	198	0.0021	0.0049	0.0269	0.0082	0.0067	0.0130
JOIN	62.87112	-145.47724	912	0.1900	-0.4400	0.0700	0.0400	0.0400	0.2000
K112	63.03706	-147.21284	929	0.0875	-0.2593	-0.0438	0.0153	0.0133	0.0154
K113	63.07838	-145.67535	1067	0.2883	-0.7835	-0.0893	0.0158	0.0236	0.0274
K76	60.28597	-149.34288	163	0.0058	-0.0022	0.0379	0.0102	0.0082	0.0143
KDK1	57.61769	-152.19343	27	0.0034	-0.0043	-0.0017	0.0073	0.0081	0.0124
KEN1	60.67508	-151.35018	56	-0.0050	-0.0124	-0.0205	0.0084	0.0077	0.0123
KENN	61.77558	-145.03691	456	0.1288	-0.0188	0.1066	0.0155	0.0198	0.0228
KODK	57.73511	-152.50138	38	-0.0005	-0.0009	0.0142	0.0060	0.0049	0.0086
KSTN	60.72011	-151.75440	88	-0.0004	-0.0025	0.0170	0.0064	0.0051	0.0095
L101	63.61317	-145.86433	650	-0.5062	0.6726	-0.0031	0.0183	0.0343	0.0476
L113	63.07766	-145.70218	1019	0.2643	-0.7668	-0.0524	0.0149	0.0152	0.0180
L122	63.09116	-146.28391	1178	0.0925	-0.4389	-0.1838	0.0233	0.0338	0.0496
L2C6	63.38283	-148.86622	715	-0.0265	-0.0612	-0.0122	0.0057	0.0050	0.0091
LADU	63.25431	-142.45289	565	0.0300	0.2223	-0.0819	0.0131	0.0299	0.0494
LIBF	61.62019	-144.53594	393	0.1296	-0.0050	-0.0341	0.0152	0.0124	0.0205

Table B.4: Denali Fault earthquake displacements

SITE	Location			Displacement			Uncertainty		
	Lat. [°]	Lon. [°]	H [m]	N [m]	E [m]	V [m]	$\sigma_N$ [m]	$\sigma_E$ [m]	$\sigma_V$ [m]
LOG	63.02263	-143.34543	665	-0.0721	1.1183	0.0600	0.0068	0.0082	0.0169
LSG1	62.05331	-147.66577	1519	-0.0017	-0.0436	-0.0110	0.0054	0.0059	0.0129
M110	63.30548	-148.18699	803	-0.0668	-0.1626	-0.0326	0.0057	0.0050	0.0091
M113	63.06575	-145.71702	1009	0.2475	-0.7364	-0.0544	0.0162	0.0243	0.0286
M120	64.79142	-148.20011	470	-0.0247	0.0259	0.1441	0.0146	0.0174	0.0342
M126	63.43299	-150.29701	1180	-0.0078	-0.0242	0.0304	0.0050	0.0046	0.0092
MACL	62.88815	-143.68000	693	2.0400	-2.5300	-0.2000	0.1000*	0.1000*	0.2000*
MAT	62.60543	-143.64182	821	0.8849	-0.3400	0.2150	0.0181	0.0181	0.0267
MCAR	61.43200	-142.92044	447	0.1151	-0.0200	-0.0563	0.0254	0.0202	0.0351
MEN	62.90947	-143.79535	705	2.1387	-2.2849	-0.2544	0.0253	0.0207	0.0349
MIDD	59.43459	-146.33457	55	0.0201	0.0027	-0.0147	0.0080	0.0063	0.0117
MILC	63.37374	-145.73184	781	1.4523	-2.3935	-0.70911	0.0147	0.0303	0.0431
MOS2	61.67558	-149.05605	219	0.0016	-0.0383	-0.0390	0.0064	0.0053	0.0096
MOTD	60.95774	-138.04046	952	0.0023	0.0038	0.0021	0.0060	0.0049	0.0097
MOTG	59.82485	-147.90778	20	0.0099	0.0111	-0.0187	0.0124	0.0095	0.0164
MPEN	60.73517	-150.48269	109	-0.0100	-0.0115	-0.0279	0.0080	0.0064	0.0117
N101	63.58135	-145.86647	661	-0.5890	0.8098	-0.0514	0.0118	0.0199	0.0240
N111	63.22630	-147.72636	942	0.0911	-0.1482	-0.0572	0.0175	0.0191	0.0316
NENA	64.57942	-149.07981	378	-0.0350	0.0345	0.0199	0.0077	0.0065	0.0118
NIK2	60.68530	-151.39150	19	-0.0120	-0.0157	-0.0097	0.0073	0.0058	0.0107
NINI	60.00854	-151.71576	98	0.0010	-0.0013	0.0020	0.0078	0.0065	0.0120
NJNC	63.00991	-141.79999	562	0.0188	0.0960	-0.0247	0.0176	0.0217	0.0366
NSLM	60.99267	-138.49645	806	0.0039	0.0055	0.0026	0.0073	0.0059	0.0107
NWOD	61.42085	-149.45104	113	0.0010	-0.0169	-0.0290	0.0137	0.0104	0.0194
O8	62.52287	-145.51557	610	0.1298	-0.1663	0.0255	0.0081	0.0120	0.0192
ORTT	62.96095	-141.93643	534	0.1848	0.1833	-0.0616	0.0103	0.0085	0.0149
P100	63.76802	-145.76973	691	-0.3318	0.2978	0.0374	0.0110	0.0166	0.0265
P586	63.41123	-145.74622	761	-1.1618	2.3436	0.2795	0.0283	0.0390	0.0497
P592	63.33972	-145.73538	781	1.2246	-1.9317	-0.4339	0.0262	0.0246	0.0479
PANA	63.48375	-148.82038	670	-0.0312	-0.0453	-0.0270	0.0051	0.0047	0.0089
PAXS	62.96727	-145.45172	1136	0.2717	-0.6192	-0.0607	0.0072	0.0062	0.0115
PISA	63.28465	-149.21055	731	-0.0325	-0.0658	0.0088	0.0048	0.0042	0.0078
POPL	60.48696	-150.06405	200	0.0004	0.0019	0.0214	0.0081	0.0066	0.0119
POPZ	60.48499	-150.05583	110	0.0063	0.0022	-0.0143	0.0093	0.0071	0.0138
POT3	61.05626	-146.69683	36	0.0148	-0.0146	0.0264	0.0058	0.0050	0.0092
POWE	61.08368	-146.30535	19	0.0242	0.0047	0.0412	0.0121	0.0101	0.0192
PPLN	64.15494	-145.84607	318	-0.1313	0.0903	0.0502	0.0068	0.0059	0.0093
PRTG	60.77121	-148.82959	50	0.0151	-0.0078	0.0060	0.0082	0.0067	0.0131
PTVL	62.53174	-150.81672	563	-0.0160	-0.0356	0.0631	0.0086	0.0067	0.0132
PURI	61.80459	-148.08936	717	0.0164	-0.0412	0.0010	0.0106	0.0084	0.0171

Table B.4: Denali Fault earthquake displacements

SITE	Location			Displacement			Uncertainty		
	Lat. [°]	Lon. [°]	H [m]	N [m]	E [m]	V [m]	$\sigma$ N [m]	$\sigma$ E [m]	$\sigma$ V [m]
Q122	63.08846	-146.39999	1254	0.0775	-0.5295	0.0240	0.0168	0.0200	0.0276
QRRY	60.62987	-152.30374	56	-0.0029	0.0108	0.0006	0.0062	0.0049	0.0093
R109	63.39527	-148.64680	765	-0.0346	-0.0794	-0.0198	0.0050	0.0045	0.0082
R110	63.29223	-148.07507	791	-0.0173	-0.1796	-0.0251	0.0214	0.0251	0.0424
R122	63.08787	-146.42408	1236	0.0721	-0.5014	-0.1087	0.0155	0.0168	0.0233
RAND	63.25066	-149.25499	683	-0.0105	-0.0737	0.1234	0.0235	0.0268	0.0542
RD44	61.80260	-147.86643	560	-0.0176	-0.0368	-0.0395	0.0111	0.0152	0.0308
REED	61.54243	-149.39592	35	0.0020	-0.0240	-0.0190	0.0073	0.0060	0.0108
RGGI	59.86519	-149.40719	28	0.0011	0.0036	0.0466	0.0070	0.0056	0.0109
RIDG	64.84958	-147.86464	150	-0.0454	0.0237	0.1165	0.0151	0.0161	0.0217
ROC	60.65374	-147.93290	19	0.0099	-0.0022	0.0038	0.0084	0.0068	0.0121
S1	61.58049	-149.44176	112	0.0029	-0.0293	0.0160	0.0112	0.0110	0.0199
S113	63.04475	-145.84431	1012	0.1885	-0.5883	0.0251	0.0267	0.0348	0.0481
S119	64.71051	-148.62493	425	-0.0075	0.0207	0.0567	0.0180	0.0180	0.0345
S122	63.09298	-146.43685	1163	0.0693	-0.5144	-0.0765	0.0152	0.0170	0.0229
S174	63.15043	-142.08123	586	0.0542	0.1730	-0.0415	0.0159	0.0182	0.0338
S72	60.94569	-149.19536	18	0.0288	-0.0130	-0.0017	0.0149	0.0131	0.0215
SELD	59.44571	-151.70667	20	-0.0017	-0.0031	0.0038	0.0059	0.0049	0.0087
SG27	71.32290	-156.61033	9	0.0027	0.0013	-0.0030	0.0057	0.0057	0.0105
SHPA	61.79976	-147.57556	802	0.0157	-0.0465	-0.0855	0.0085	0.0103	0.0221
SICH	62.98763	-143.35446	658	-0.0600	1.3700	0.0400	0.1000*	0.1000*	0.2000*
SLBR	62.70486	-143.94742	672	0.9291	-0.4817	0.1292	0.0180	0.0173	0.0254
SLCH	64.47674	-146.97640	274	-0.0965	0.0582	0.0235	0.0066	0.0057	0.0102
SLIM	63.51200	-148.80409	650	-0.0489	-0.0409	-0.0192	0.0049	0.0043	0.0082
SOUR	62.66391	-145.48372	748	0.1430	-0.2537	0.0069	0.0138	0.0120	0.0181
SPIL	65.22682	-147.08437	420	-0.0460	0.0228	-0.0946	0.0102	0.0086	0.0154
SSWB	63.34131	-149.09023	733	-0.0245	-0.0605	-0.0023	0.0052	0.0049	0.0090
STEP	59.43431	-153.76484	434	-0.0042	-0.0181	0.0008	0.0099	0.0085	0.0128
STRI	63.33337	-142.95313	512	0.0205	0.2902	-0.0444	0.0100	0.0083	0.0146
SXQD	60.47594	-151.04173	36	-0.0072	-0.0077	-0.0326	0.0094	0.0074	0.0130
T122	63.10017	-146.44333	1107	0.0677	-0.4940	-0.0117	0.0144	0.0171	0.0218
T19	60.11921	-149.42861	20	-0.0000	-0.0049	0.0279	0.0086	0.0069	0.0132
TAZL	62.07986	-145.43290	449	0.0928	-0.0630	0.0299	0.0067	0.0055	0.0098
TEM1	59.45023	-135.33020	13	0.0062	-0.0030	0.0164	0.0055	0.0047	0.0087
THMP	61.12800	-145.73227	863	0.0470	-0.0031	0.0488	0.0101	0.0083	0.0141
TLKA	62.30765	-150.42030	164	-0.0120	-0.0262	-0.0376	0.0081	0.0095	0.0155
TNK1	59.27222	-135.44049	13	0.0096	-0.0087	0.0089	0.0066	0.0063	0.0125
TP26	63.25465	-143.03903	541	0.0483	0.3946	-0.0875	0.0113	0.0142	0.0284
TRAI	63.16107	-143.19991	610	0.0408	0.6085	-0.1088	0.0113	0.0137	0.0266
TRLK	60.50151	-149.42026	173	0.0027	-0.0053	0.0167	0.0067	0.0055	0.0103

Table B.4: Denali Fault earthquake displacements

SITE	Location			Displacement			Uncertainty		
	Lat. [°]	Lon. [°]	H [m]	N [m]	E [m]	V [m]	$\sigma_N$ [m]	$\sigma_E$ [m]	$\sigma_V$ [m]
TSEA	61.18733	-149.89497	43	-0.0043	-0.0183	0.0006	0.0058	0.0049	0.0088
TSIN	61.20357	-145.52823	512	0.0499	-0.0019	-0.0149	0.0074	0.0061	0.0108
TURN	60.93053	-149.54331	25	0.0037	-0.0152	-0.0421	0.0081	0.0065	0.0121
TWB1	63.35931	-143.31607	489	-0.0225	0.3328	-0.1333	0.0121	0.0177	0.0354
U113	63.04204	-145.88800	932	0.1513	-0.5580	-0.0314	0.0276	0.0386	0.0550
U122	63.10938	-146.45342	1039	0.0414	-0.4815	0.0088	0.0228	0.0371	0.0684
UAMF	60.09850	-149.44240	18	-0.0078	-0.0123	-0.0414	0.0089	0.0073	0.0131
V113	63.04739	-145.91613	914	0.1743	-0.5828	-0.0616	0.0163	0.0188	0.0256
V122	63.12012	-146.46137	989	0.0806	-0.5582	-0.0743	0.0146	0.0186	0.0223
V61	62.65230	-145.48471	762	0.1583	-0.2821	0.0715	0.0112	0.0171	0.0271
W109	63.38983	-148.50673	674	-0.0201	-0.0761	0.0258	0.0133	0.0149	0.0335
W112	63.04355	-146.92271	914	0.0770	-0.3227	-0.0721	0.0165	0.0158	0.0230
W176	64.07565	-141.63261	548	0.0302	0.0799	-0.0166	0.0180	0.0296	0.0555
WHIT	60.75051	-135.22211	1427	0.0014	0.0040	0.0053	0.0057	0.0050	0.0090
WICK	65.18270	-148.06620	756	-0.0372	0.0100	0.0148	0.0111	0.0089	0.0167
WILL	61.89514	-145.27141	437	0.0876	-0.0320	0.0246	0.0127	0.0155	0.0123
WOND	63.49123	-150.87367	661	-0.0068	-0.0188	-0.0205	0.0070	0.0058	0.0110
X113	63.05131	-145.97481	886	0.1617	-0.5715	-0.0237	0.0153	0.0146	0.0210
X122	63.12367	-146.51160	925	0.0643	-0.5129	-0.0749	0.0154	0.0158	0.0215
X61	62.59682	-145.45993	695	0.1239	-0.2024	0.0257	0.0088	0.0095	0.0161
X7	60.85918	-137.06285	659	-0.0021	0.0011	-0.0058	0.0081	0.0067	0.0116
Y111	63.09679	-147.48462	813	0.1060	-0.1893	-0.0562	0.0161	0.0141	0.0171
Y113	63.04734	-145.99660	875	0.1333	-0.5698	-0.0326	0.0177	0.0230	0.0301
Y122	63.11855	-146.54273	907	0.0678	-0.5230	-0.0791	0.0185	0.0281	0.0402
Y565	61.59267	-139.44490	757	0.0120	0.0037	-0.0196	0.0078	0.0064	0.0116
Y61	62.58230	-145.48096	681	0.1279	-0.1930	-0.0155	0.0112	0.0135	0.0219
YKTT	59.51074	-139.64880	18	0.0182	-0.0058	-0.0002	0.0061	0.0049	0.0097
YUKO	65.67618	-149.09299	194	-0.0228	0.0167	-0.0436	0.0180	0.0146	0.0278
Z113	63.04543	-146.02274	886	0.1430	-0.5342	-0.0230	0.0158	0.0172	0.0263
Z117	64.38854	-149.01388	152	-0.0553	0.0481	0.1478	0.0141	0.0165	0.0324
Z122	63.11651	-146.57171	973	0.0783	-0.4268	-0.1674	0.0159	0.0245	0.0320
Z22A	61.75422	-150.05237	73	0.0150	-0.0397	-0.0422	0.0119	0.0131	0.0202

\* Uncertainty not known.